LOW DIMENSIONAL SEMICONDUCTING NANOSTRUCTURES:

STABILITY, TRENDS AND PROMISES

by

PRABATH WANAGURU

DISSERTATION

Submitted in partial fulfillment of the requirements
for the degree of Doctor of Philosophy at
The University of Texas at Arlington
May, 2016

Arlington, Texas

Supervising Committee:

Qiming Zhang, Supervising Professor
Muhammad N. Huda
Seong J. Koh
Joseph H. Ngai
Alexander H. Weiss

ABSTRACT

LOW DIMENSIONAL SEMICONDUCTING NANOSTRUCTURES:

STABILITY, TRENDS AND PROMISES

Prabath Wanaguru, Ph.D.

The University of Texas at Arlington, 2016

Supervising Professor: Qiming Zhang

Systematic studies of low dimensional semiconducting nanostructures have been performed. In particular, silicon-germanium (SiGe) armchair type nanotubes, and both zigzag and armchair type nanoribbons were used to represent the bottom-up approach while hematite nanoribbons were used to represent the top down approach. Four high symmetric nanostructure atomic arrangements were identified. All the SiGe nanotubes and SiGe nanoribbons show definite semiconducting character and the band gaps span over large range. Zigzag SiGe nanoribbons show direct band gap nature indicating potential applications in opto-electronic devices. Standalone SiGe nanoribbons may roll into nanotubes depending on the atomic arrangement. Li adsorption on SiGe nanotubes indicated

that SiGe nanotubes have potential as anode material in Li-ion battery technology when the nanotube length is over 20 Å. Most stable site for Li adsorption is Si Top site and most preferred site is Ge Top. Intrinsic puckered surface nature screen the adsorbed Li from each other and hence, increase the charge density. Hydrogen atomic adsorption increases the band gap while oxygen breaks the nanotube-wall bonds and incorporates into nanotube lattice structure.

Hematite nanoribbons based on two surfaces, (110) and (104) were studied. For each surface, depending on the termination direction, it can be identified two types. Both types based on (110) surface show definite semiconducting character. One type of (104) surface based nanoribbons show surface modification while the other type obtained built-in oxygen vacancy which acquired the spin dependent transport properties and hence, possible applications in spintronics area.

ACKNOWLEDGEMENTS

I would like to remember and thank Dr. Asok K. Ray, who provided valuable guidance in carrying out this dissertation work. He was a great mentor and a very talented motivator. My heartfelt gratitude goes to my advisor Dr. Qiming Zhang, who graciously provided his invaluable guidance, advice, and support in completing this dissertation. He allowed me to grow and helped in every possible manner. To him I am highly indebted. My sincere gratitude goes to my committee members, Drs. M. Huda, S. Koh, J. Ngai, and A. Weiss, for taking their valuable time to participate in my dissertation work. I would like to thank Dr. Raymond Atta-Fynn for being a great friend and mentor. It is indeed a great pleasure to know him. I also like to express my gratitude to the Physics Department for supporting my time here at UTA. I would like to acknowledge my fellow group members Jiao An and Yuting Peng for their support.

Finally, I would like to recognize my wife Oshani, and my daughter Odara for their unwavered support throughout this journey.

April 15, 2016

TABLE OF CONTENTS

LIST OF FIGURES

LIST OF TABLES

Chapter 1

Introduction

1.1 Overview of Current One-Dimensional Nanomaterials and Some of Their Applications

Discovery of carbon nanotubes by S. Iijima [1], in 1991 has triggered many interesting research on one-dimensional (1D) nanostructures, such as nanotubes (NT), nanoribbons (NR), and nanowires (NW). Among those 1D nanostructures, carbon based nanostructures exhibit excellent electrical, thermal and mechanical properties, with applications spanning on vast area [2-11]. In fact, carbon nanotubes (CNTs) have been proposed as the emerging materials to provide solutions to the complications arising when decreasing the sizes of technology nodes in complementary metal-oxide-semiconductor (CMOS) technology [12,13].

On the other hand, the transformation from macro scale to nano scale has introduced novel physical phenomena such as quantum size effects [14,15] and edge effects [16]. Furthermore, the size minimization has increased the surface to volume ratio [17] which increases the reactivity of these 1D nanostructure materials immensely [18-20]. Additionally, at nanometer scale, these 1D nanostructures known to modify their respective bulk electronic structure

properties such as band nature (i.e. flat or curve), band gap and the direct/indirect nature [20] drastically. Furthermore, these nanostructures provide a quasi-1D path for carriers which increase the mobility exponentially [18]. For example it is known that these carbon nanostructures, particularly the CNTs have very high carrier mobilities than the commercial grade silicon materials carrier mobility [21,22].

Despite having all those excellent properties, integration of carbon nanostructures into current, existing silicon microelectronic technology is a challenge. First, nanostructures are based on a different element compared to silicon microelectronic technology and second, the most popular 1D carbon nanostructure, the carbon nanotubes, exhibit either metallic or semiconductor behavior depending on the chirality and diameter [23]. Hence, in a given sample of CNTs, it may contain both metallic and semiconducting nanotubes. This limits the usage of CNTs in silicon microelectronic technology and creates an additional step, where it is necessary to separate these nanotubes into semiconducting and metallic categories before they could be used in their respective applications [24-26]. Therefore, it is natural to look for nanostructures based on other elements which could exhibit characteristics similar to carbon-based nanostructures and integrate easily with the existing silicon microelectronic technology.

The obvious choice would be silicon-based nanostructures since the CMOS technology is driven by Silicon. Silicon has been the workhorse of the CMOS industry and widely considered as the most important element in the 20th century. However, silicon also has some drawbacks. It has an indirect band gap which makes it difficult to create efficient optoelectronic devices. Additionally, the carrier mobility is not that excellent, which limit the applications in high-speed devices. Despite those drawbacks, silicon still thrived in CMOS technology due to many other reasons. It is abundant and can be purified to have very low background impurity concentration. Silicon has a high yielding percentage and excellent thermal properties [27,28] which help immensely in getting a defect free material and dissipating the generated heat from transistors, respectively. Its "diamond" crystallization is extremely stable, and the excellent mechanical properties are very helpful in the fabrication process [27,28]. The most important feature is its ability to grow high-quality dielectric medium, SiO_2, trivially [28].

However, recent development of the CMOS technology which is decrease of node size creates issues in usage of silicon. For example as the technology node size decreases (moving onto nanometer scale) the physical thickness of different layers of CMOS are reduced [29]. Particularly the gate oxide (SiO_2) has become thinner than the limit of electronic tunneling distance [29]. Hence, the gate leakage current becomes unavoidably high where it is necessary that the silicon's most important advantage (trivial generation of SiO_2) must be replaced

[29] with a high dielectric constant (k) material such that the gate leakage current is reduced. Therefore, it is clear that Si alone cannot progress towards the new CMOS technology. We need a material that is semiconducting, capable of creating nanostructures and high-k oxides. Such a material will be able to integrate into existing silicon microelectronic technology quite effectively and efficiently.

On a different aspect, the CNTs have studied extensively as potential anode materials for Li-ion battery (LIB) technology [30-32]. CNTs exhibit better output than the current commercialize anode material graphite due to their high electronic conductivity and high thermal and mechanical stability [33]. Predicted theoretical maximum capacity and stoichiometry of CNTs are 1116 $mAhg^{-1}$ and LiC_2 and they are very high compared to 372 $mAhg^{-1}$ and LiC_6 values of graphite [33]. Carbon nanotube value of the theoretical maximum capacity is the highest capacity reported among the carbon-based materials. In determining such a high value, the intrinsic porosity and the quasi-1D nature associated with the CNT play higher role.

There are two main areas of research involved in LIB anode material technology. One area of research is focused on enhancing the properties of carbon-based anode materials and the other area of research focused on finding an alternative material to carbon-based materials. It is highly important to study the

viability of other nanoscale materials than the carbon as anode materials since they may further enhance many properties of LIB. For example, LIB anode materials which increase specific capacities beyond the CNTs, and the materials with higher Li diffusion capabilities may lead the LIB technology applications beyond the portable devices [34].

When considering the alternative materials for carbon-based anode materials, silicon (Si) and germanium (Ge) are two of the most promising materials. Particularly, the Si materials have the highest recorded gravimetric (4200 mAh g^{-1} with $Li_{22}Si_5$ stoichiometry) and volumetric (9786 mAh cm^{-3}) densities among many LIB anode candidates [35-39]. On the other hand, Ge does not have Li adsorption densities as high as Si but still has higher Li adsorption density than CNT's Li adsorption density [40,41]. Furthermore, Ge has an excellent intrinsic electrical conductivity which is in the order of ~10^4 times that of Si [34]. Considering Si is the second most abounded element on earth, and along with its high adsorption densities, it is clear that, either Si or its heterostructure material in nanoscale regime could be the ideal candidate for an enhanced LIB anode material.

However, Si or Ge usage as LIB anode material is limited due to the huge volume changes (Si ~400% and Ge ~300%) which occur during the charging and discharging cycles [34]. This volume change leads the materials to their

breakdown point in terms of Li-ion reversibility. Hence, it is essential to use nanostructure forms of Si and Ge elements such that they may provide the necessary free volume to sustain the huge volume changes happening in charging and discharging cycles.

Another interesting research area which uses 1D nanostructure is in solar energy conversions [42-45]. The integration of nanostructures into solar energy conversion is mainly driven by the excellent outcomes that the nanostructures have been shown in other research areas. Inherent properties of 1D nanostructures such as high surface to volume ratio could result in high light absorption, reduced charge recombination, improved carrier mobility, increased reaction rate *etc*. However, when it comes to photo-voltaic cell technology, the typical 1D nanostructure like CNTs display less success (~3% efficiency) than crystalline Si (~25% efficiency) [46]. Again, the reason for CNTs inefficiency is due to the fact that the given sample of CNTs having a mixture of different chirality nanotubes, where particular chirality absorb light only on a particular wavelength [47]. Quite interestingly, even though crystalline Si show high efficiency, when Si moves towards the thin film structures or reduced dimensionality, the photo-voltaic cell efficiency suffers and record a value of ~10.5% [46]. On the other hand, heteronuclear structure thin films, for example GaAs thin films thrived and recorded an efficiency of ~28% while multi-junction photo-voltaic cells of GaInP/GaAs and GaInAsP/GaInAs recorded an efficiency of ~46% [46]. In terms

of the other solar energy conversion materials, another potential material is hematite (α-Fe_2O_3). Hematite has a highly favorable light absorption band gap of ~2.0 eV, and it is earth abundant, non-toxic and cost effective. However, due to spatially localized Fe 3d orbitals, hematite demonstrates very poor carrier mobility and hinders its usage as a potential solar energy conversion material. However, with the inherent properties of 1D nanostructures and the general positive properties of hematite can be consider as potential solar energy conversions material.

1.2 Nanostructure Generation: Bottom-Up versus Top-Down Approaches

Designing and synthesizing of nanometer scale materials can be categorized into two different approaches: the bottom-up approach and the top-down approach. The bottom-up approach is employed when building a nanostructure from the scratch. The method, first start with a concentration of atoms, ions or molecules (building blocks) and then the growth of the nanostructure is proceed with continues supply of “building blocks” until the desired formation and size is realized. This is more suitable for the situations where the bulk structure of the desired material is not available or too expensive and/or in need of material with specific properties. On the other hand, the top-down approach is more suitable when the bulk material is available and/or less

expensive. The Method starts with a bulk structure and then removes materials until the desired nanostructure formation or the size are generated. For removing materials and molding the nanostructures, one has to employ dry/wet etching techniques and annealing techniques respectively. It is worth to mention that the material waste is high on this approach and for decades the method of top-down is used simply because of its capability of providing high quality structures and yield. However, the recent scale down of device sizes or the increase of device density is affected by this approach. For instance technology nodes have problems in achieving required resolutions below 100 nm.

1.3 Motivation

Considering the current standings of nanostructures and the future demands of different technologies, it is safe to assume that smart nanostructure materials are essential. The essence of nanostructures can be captured with the bottom-up approach and with that the freedom to generate tailored nanostructures with desired properties is much higher. In order to generate desired smart nanostructures, alloying of two different elements which complement and enhance each other's properties is a must. Considering this purpose, we have looked into SiGe nanostructure materials and specifically, the design of SiGe nanotubes and nanoribbons. In addition, we have studied the stability of SiGe

nanotubes by allowing the SiGe to interact with common atmospheric impurities such as hydrogen and oxygen. Furthermore, we studied the viability of SiGe nanotubes as LIB anode materials.

Considering the top-down approach in nanometer scale, it is necessary to identify a bulk material which has properties of earth-abundant, non-toxic, cost-effective and the like. In this regard, we studied the hematite nanoribbons, and in particular to identify and understand its possibilities in solar energy conversion technologies.

All our work has been performed using computational simulations employing the methods of density functional theory (DFT) and beyond DFT (discussed in Chapter 2). We identified the structure stabilities in terms of their binding energies, and their electronic nature in terms of highest occupied molecular orbital (HOMO)-lowest unoccupied molecular orbitals (LUMO) gap or band gap.

This work contains study of SiGe nanotubes with cluster approach in Chapter 3, their interaction with lithium in Chapter 4, and their interaction with atmospheric impurities in Chapter 5. Then the focus shift on to another form of SiGe nanostructure which is fully hydrogenated SiGe nanoribbons where it is studied the ability of SiGe nanoribbons to remain as standalone structure without any substrate (Chapter 6). Then we present the study of hematite nanoribbons on

chapter 7 and finally the conclusions of this work in Chapter 8. All the SiGe based studies were performed using the GAUSSIAN 03/09 [48] suite of programs and the hematite work was performed using the Vienna Ab initio simulation package (VASP) [49,50].

Chapter 2

Theory

2.1 Introduction

Understanding of laws governing the chemical and physical properties of matter has been the central issue of scientists for centuries. In early 20^{th} century, owing much to the analogy between gravitational interactions found in planetary systems and electrostatic interactions found in charge particle systems, the scientists came up with a model for atom. For example, if the atom consists with Z electrons with each have a charge of –e orbiting around the nucleus of charge Ze. However, according to the successful electromagnetic theory, the model of orbiting electrons around the nucleus would be fault due to orbiting charged particle should radiate energy and thus decelerating and eventually collapsing to nucleus. This reasoning contradicts very existence of the matter. Therefore, it is evident that there should be a different set of laws which governs the matter at atomic level, and hence the birth of Quantum Mechanics as known today.

In general matter can be identified as a collection of interacting atoms. The system may in a gas phase such as molecules, clusters or may in a condensed phase such as solids. Whatever the phase system is in, at the fundamental level, it is all about set of atomic nuclei and electrons that interacting with each other

through electrostatic and columbic forces. This requires the solution to the many-body Schrodinger or Dirac equation:

$$\hat{H}\Psi = E\Psi\,, \tag{2.1}$$

where $\Psi = \Psi(\vec{R}, \vec{x})$ is the many body wave function, which contains all the information about the system and depends on 3N electronic spatial variables, N electronic spin variables, and 3P nuclear spatial variables. In addition, $\vec{R} = \{\vec{R}_I ; I = 1, \ldots, P\}$ and $\vec{x} = \{\vec{x}_i ; i = 1, \ldots, N\}$. $\hat{H}$ is the Hamiltonian operator. The non-relativistic Hamiltonian is given by

$$\hat{H} = -\sum_{I=1}^{P} \frac{\hbar^2}{2M_I} \nabla_I{}^2 - \sum_{i=1}^{N} \frac{\hbar^2}{2m} \nabla_i{}^2 + \frac{1}{4\pi\varepsilon_0} \sum_{I=1}^{P} \sum_{J \neq I}^{P} \frac{e^2 Z_I Z_J}{2\left|\vec{R}_I - \vec{R}_J\right|} + \frac{1}{4\pi\varepsilon_0} \sum_{i=1}^{N} \sum_{j \neq i}^{N} \frac{e^2}{2\left|\vec{r}_i - \vec{r}_j\right|} - \frac{1}{4\pi\varepsilon_0} \sum_{I=1}^{P} \sum_{i=1}^{N} \frac{e^2 Z_I}{\left|\vec{R}_I - \vec{r}_i\right|}\,,$$

(2.2)

where the first term is the kinetic energy of the nuclei, the second term is the kinetic energy of the electrons, the third term is the nucleus-nucleus interaction, the fourth term is the electron-electron interaction, and the last term is the electron-nuclei interaction. In theory, all the properties of a system in question can be derived by solving equation 2.1 with the Hamiltonian in equation 2.2. In practical this can be achieved only for hydrogen atom or hydrogen atom like systems which contains only two particles.

In general, the term in equation 2.2 that becomes the most difficult/impossible to compute is the electron-electron interaction. It is due to the fact that the motion of individual electron cannot be found without simultaneously

considering all the other electrons in the system (correlation). Hence, in solving the equation 2.1, it is necessary to use controlled approximations. This leads to the 1st approximation, Born-Oppenheimer approximation [51] in solving equation 2.1 (*Time-Independent Schrödinger Equation-TISE*). It states that when considering the time scales associated with the motion of electrons and nuclei, electrons move much quicker where nuclei can be considered as stationary. By applying this approximation, system can be interpreted as electrons moving in a field of fixed nuclei and hence the Hamiltonian in equation will change as follows.

$$\hat{H} = -\sum_{i=1}^{N} \frac{\hbar^2}{2m} \nabla_i^{\,2} + \frac{1}{4\pi\varepsilon_0} \sum_{i=1}^{N} \sum_{j \neq i}^{N} \frac{e^2}{2\left|\vec{r}_i - \vec{r}_j\right|} - \frac{1}{4\pi\varepsilon_0} \sum_{I=1}^{P} \sum_{i=1}^{N} \frac{e^2 Z_I}{\left|\vec{R}_I - \vec{r}_i\right|}, \tag{2.3}$$

where the first term in equation 2.2 can be neglected since nuclei not moving. In addition, the third term becomes constant and can be taken out of the Hamiltonian operator 2.2 since an added constant to the operator only shift the eigenvalue and does not change the eigenfunctions of the operator. Furthermore the equation 2.3 shall be written in atomic units in following manner.

$$\hat{H} = -\frac{1}{2} \sum_{i=1}^{N} \nabla_i^{\,2} + \frac{1}{2} \sum_{i=1}^{N} \sum_{j \neq i}^{N} \frac{1}{\left|\vec{r}_i - \vec{r}_j\right|} - \sum_{I=1}^{P} \sum_{i=1}^{N} \frac{Z_I}{\left|\vec{R}_I - \vec{r}_i\right|}, \tag{2.4}$$

2.2 Hartree and Hartree-Fock approximations

It has been an important goal of physics to solve this many particle problem. In the Hartree approximation [52], the many-electron wave function is constructed from the product of single particle functions,

$$\Psi(\vec{x}_1,\vec{x}_2,...,\vec{x}_N) = \Psi_1(\vec{x}_1)\Psi_2(\vec{x}_2)...\Psi_N(\vec{x}_N), \tag{2.5}$$

where each of the functions $\Psi_i(\vec{x}_i)$ satisfies a one-electron Schrödinger equation, with an additional potential term, which arises from the average field of the other electrons. The Schrödinger equation for a single electron can be written as

$$\left[-\frac{1}{2}\nabla^2 + V(\vec{r}_i) + \varphi_i\right]\Psi_i(\vec{r}) = \varepsilon_i\Psi_i(\vec{r}), \tag{2.6}$$

where the Coulomb potential φ_i is given by Poisson's equation

$$\nabla^2\varphi_i = 4\pi \sum_{j=1,i\neq j}^{N}\left|\Psi_j\right|^2, \tag{2.7}$$

and $V(\vec{r}_i)$ is the potential due to the nuclei. In equation 2.6 the argument becomes $\vec{r}_i$ from $\vec{x}_i$ since in Hartree approximation, the spin is considered in ad hoc manner and only the coordinate of an electron is there. The foregoing ad hoc manner of spin treatment and the wave function not being anti-symmetric are the major problems with this approximation. However, the Hartree product wave function can be replaced by a single determinant function (Slater determinant), which leads to the Hartree-Fock approximation [52,53], may be simple solution to

the required anti-symmetry nature of the wave function. The inclusion of Fermi statistics, which introduces an additional, nonlocal exchange term in the Schrödinger equation, improves the total energy calculation, but the single particle picture, with the wave function described in terms of orbitals with particular spins and occupation numbers, is unchanged. It is noted that a single Slater determinant wave function lead to a poor energy since the lowest-lying configuration is generally only one of very many with comparable energies. It is further noted that a better approximation would result from taking a linear combination of Slater determinants [54]. This approach known as "configuration interaction" (CI) and it improves the correlation effects beyond Hartree-Fock approximation by including the many-particle wave functions. In principle, CI provides an exact solution of the many-electron problems. However, in practice the explosive increase in the number of configurations with increasing electron number limits its application to only small systems with relatively few electrons and the complexity of the resulting solutions implies that a simple interpretation of the results is often difficult.

2.3 Hohenberg-Kohn Theorems

The earliest form of DFT was based on the Thomas-Fermi model [55,56]. However, its applications were limited due to the inaccurate representation of the

kinetic energy functional and exchange energy, and the exclusion of the electron correlation effects. Kinetic energy is calculated by assuming that the motions of the electrons are uncorrelated and the Thomas-Fermi model does not require the anti-symmetrized wave function with respect to permutation of any pair of electrons. The formulation of DFT as an exact ground state theory of many-body systems truly began with the work by Hohenberg and Kohn in 1964 [57].

Hohenberg and Kohn built on the Thomas-Fermi model, using it in conjunction with their two theorems. The first Hohenberg-Kohn theorem uses the electron density $\rho(r)$ as the basic variable. It states that the external potential $v(r)$ is determined, within a trivial additive constant, by the electron density $\rho(r)$.

First consider the electron density $\rho(r)$ for the non-degenerate ground state of an N-electron system. Then the number of electrons is determined by the following equation:

$$\int \rho(r)dr = N \tag{2.8}$$

If $\rho(r)$ also determines $v(r)$, it follows that $\rho(r)$ determines the ground-state wave function Ψ and hence, all the other electronic properties of the system. Suppose that there are two different external potentials v and v' that give the same $\rho(r)$ for their ground state. Then there would be two Hamiltonians, H and H', whose ground-state densities were the same although the normalized wave functions Ψ and Ψ' would be different. Each of these Hamiltonians and its

corresponding wave function would satisfy time independent Schrodinger's equation:

$$H\Psi = E\Psi, \tag{2.9}$$

$$H'\Psi' = E'\Psi', \tag{2.10}$$

where E and E' are the ground-state energies for H and H' respectively. Therefore, the expectation value of H in Ψ' has to be greater than E because it would be in a higher state:

$$\begin{aligned} E < \langle \Psi' | H | \Psi' \rangle &= \langle \Psi' | H + H' - H' | \Psi' \rangle \\ &= \langle \Psi' | H' | \Psi' \rangle + \langle \Psi' | H - H' | \Psi' \rangle \\ &= E' + \int \rho(r)[v(r) - v'(r)]dr \end{aligned} \tag{2.11}$$

Similarly, the expectation value of H' in Ψ would be greater than E',

$$\begin{aligned} E' < \langle \Psi | H' | \Psi \rangle &= \langle \Psi | H' + H - H | \Psi \rangle \\ &= \langle \Psi | H | \Psi \rangle + \langle \Psi | H' - H | \Psi \rangle \\ &= E - \int \rho(r)[v'(r) - v(r)]dr \end{aligned} \tag{2.12}$$

Adding (2.11) and (2.12) leads to inequality 2.13:

$$E + E' < E' + E \tag{2.13}$$

This is a contradiction, so there cannot be two different external potentials that give the same ground-state densities.

Hence the $\rho(r)$ determines N, v, and all properties of the ground state. The total ground state energy can be written as a functional of the electron density:

$$E[\rho] = T[\rho] + V_{ne}[\rho] + V_{ee}[\rho], \tag{2.14}$$

where $T[\rho]$ is the kinetic energy, $V_{ne}[\rho]$is the nuclei-electron interaction energy and $V_{ee}[\rho]$ is the electron-electron Coulomb interaction energy. The nuclei-electron interaction is considered as an external potential, and the external potential $v(r)$ can be expressed as

$$V_{ne}[\rho] = \int \rho(r)v(r)dr\,, \tag{2.15}$$

Hohenberg and Kohn also grouped the other two energy terms into a single functional $F_{HK}[\rho]$. So the energy is written as

$$E[\rho] = \int \rho(r)v(r)dr + F_{HK}[\rho], \tag{2.16}$$

where

$$F_{HK}[\rho] = T[\rho] + V_{ee}[\rho], \tag{2.17}$$

The second Hohenberg-Kohn theorem states that for a trial density, $\rho'(r)$, such that $\rho'(r) \geq 0$ and $\int \rho'(r)dr = N$,

$$E_0 \leq E[\rho'], \tag{2.18}$$

where $E[\rho']$ is the energy functional from equation (2.14). This theorem gives the energy as an application of the variational principle, in which the ground-state electron density is considered to be the density that minimizes $E[\rho]$.

The proof of this second theorem begins by considering that there must be a ground state density function $\rho(r)$ with a corresponding external potential, v, Hamiltonian, H, and wave function, Ψ. This ground state density function is not known exactly, but a trial density function $\rho'(r)$ can be used as a starting point:

$$\langle \Psi' | H | \Psi' \rangle = \int \rho'(r) v(r) dr + F_{HK}[\rho'], \tag{2.19}$$

Furthermore, the energy associated with the trial function must be greater than the ground state energy:

$$E[\rho'] \geq E[\rho], \tag{2.20}$$

Assuming differentiability of $E[\rho]$, the variational principle requires that the ground-state density satisfies the stationary principle,

$$\delta\{E[\rho] - \mu(\int \rho(r) dr - N)\} = 0 \tag{2.21}$$

Using the constraint that

$$\int \rho(r) dr = N \tag{2.22}$$

and the Lagrange multiplier μ, gives the Euler-Lagrange equation

$$\mu = v(r) + \frac{\delta F_{HK}[\rho]}{\delta \rho(r)}, \tag{2.23}$$

This equation is the basis of density functional theory. Unfortunately, (2.23) cannot be solved exactly because $F_{HK}[\rho]$ is not explicitly known. To proceed, some satisfactory approximation for this term must be utilized.

2.4 Kohn-Sham Method

The form of DFT used in this work follows from the theories of Kohn and Sham [58]. First, they rearrange the unknown universal functional $F_{HK}[\rho]$. They assume that the kinetic energy term has a component that is independent of the electron-electron interaction $T_s[\rho]$ and that the electron-electron potential term has a component that is described as a classical Coulomb potential $J[\rho]$. Then, the unknown universal functional can be written as

$$F_{HK}[\rho] = T_s[\rho] + J[\rho] + E_{xc}[\rho], \tag{2.24}$$

where $T_s[\rho]$ is the kinetic energy term generated from non-interacting electrons, $J[\rho]$ is the classical Coulomb potential and the third term is unknown exchange-correlation energy term which may be define as follows.

$$E_{xc}[\rho] = T[\rho] - T_s[\rho] + V_{ee}[\rho] - J[\rho] \tag{2.25}$$

This exchange-correlation term includes all the terms that involve electron-electron interaction. Rather than working strictly in terms of density functionals, Kohn and Sham write the ground state wave function as a combination of N orbitals $\Psi_i(r,s)$ and the non-interacting many electron wave function as follows.

$$\Psi_s = \frac{1}{\sqrt{N!}} \det\left[\Psi_1 \Psi_2 ... \Psi_n\right], \tag{2.26}$$

This makes the Sham kinetic energy term

$$T_s[\rho] = \sum_{i=1}^{N} \left\langle \Psi_i \left| -\frac{1}{2}\nabla^2 \right| \Psi_i \right\rangle, \tag{2.27}$$

Kohn and Sham keep the Coulomb potential term as a functional of density, though

$$J[\rho] = \frac{1}{2}\int \frac{\rho(r)\rho(r')}{|r-r'|} dr dr' \ , \tag{2.28}$$

Also, the density can be redefined in terms of the orbitals:

$$\rho(r) = \sum_{i}^{N} \sum_{s} |\Psi_i(r,s)|^2 \ , \tag{2.29}$$

The variational principle involves minimizing the energy expression. This time it is minimized with the constraint that the orbitals are orthonormal

$$\int \Psi_i^* \Psi_j dx = \delta_{ij} \, , \tag{2.30}$$

and introducing ε_{ij} terms as the Lagrange multipliers. After applying the variational principle, Kohn and Sham found that for a single orbital

$$\left(-\frac{1}{2}\nabla^2 + v_{eff} \right) \Psi_i = \varepsilon_i \Psi_i \, , \tag{2.31}$$

where the background effective potential is

$$v_{eff} = v(r) + \int \frac{\rho(r')}{|r-r'|} dr' + v_{xc}(r) \tag{2.32}$$

and the exchange-correlation potential is

$$v_{xc}(r) = \frac{\delta E_{xc}[\rho]}{\delta \rho(r)} \tag{2.33}$$

These three equations (2.31 – 2.33) and the definition of the density in terms of orbitals (2.29) are the four essential Kohn-Sham equations.

Figure 2.1 illustrates the method in which the Kohn-Sham equations can be applied to find the energy of a system. The process begins with a trial density function, $\rho_{in}(r)$. This initial density is inserted into equations (2.32) and (2.33) to solve for v_{eff}. Then the effective potential is inserted into equations (2.29) and (2.31) to find a new density function, $\rho_{out}(r)$. The process is subject to a convergence requirement ε_r. If the difference between $\rho_{in}(r)$ and $\rho_{out}(r)$ is less than this requirement, the density is used in equation (2.16) to find the ground state energy. If the convergence criteria is not met, then $\rho_{out}(r)$ becomes a new trial density and the loop starts again until the convergence criteria is satisfied.

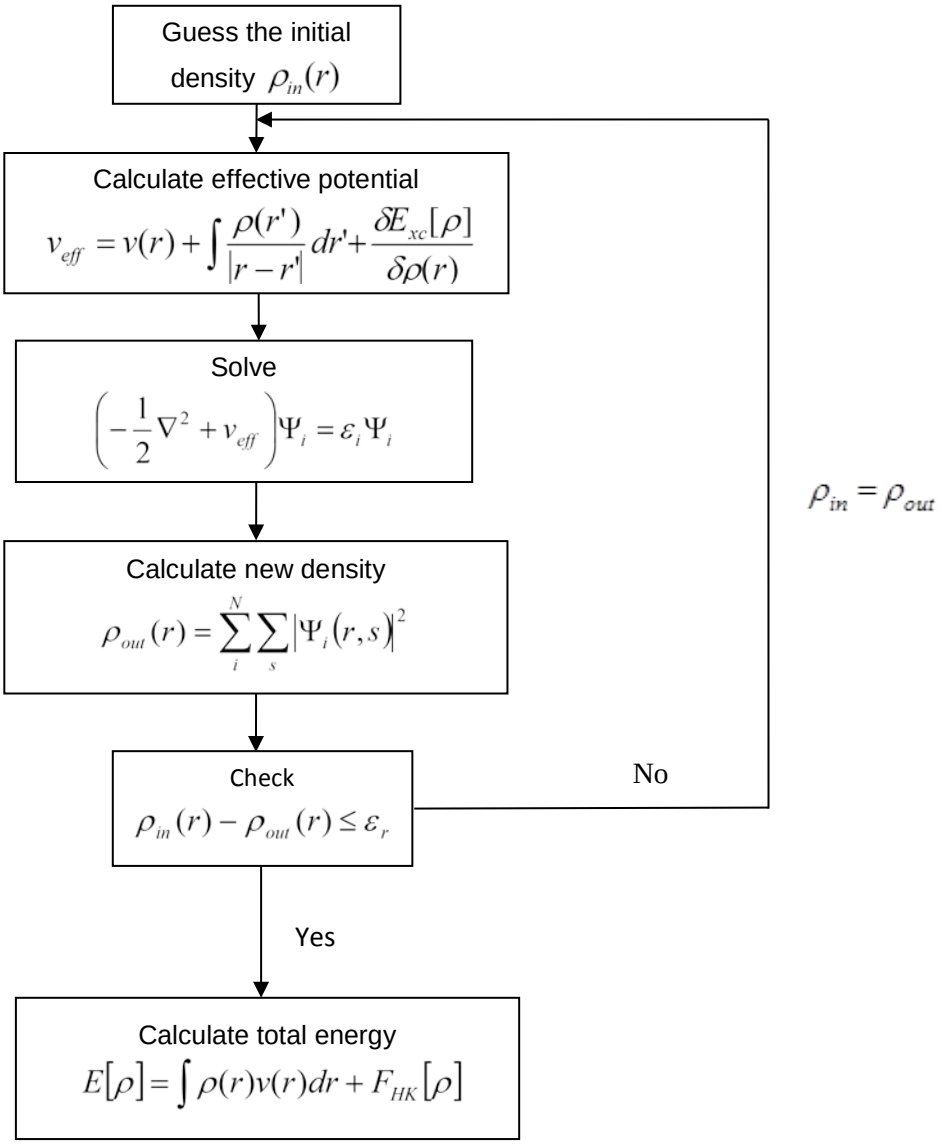

Figure 2.1: Flowchart for DFT self-consistency calculations

The Kohn-Sham scheme provides a simple but rigorous way to compute the electronic properties within density functional theory. In principle, the Kohn-Sham equations will yield exact ground state properties if an exact exchange correlation potential is given. However, the Kohn-Sham scheme does not provide methods to obtain the explicit exchange and correlation functionals and therefore, approximations have to be considered.

2.5 Local Density Approximation

This local density approximation was proposed by Kohn and Sham [58]. They showed that it could be applied to the limiting case of a slowly varying density.

$$E_{xc}^{LDA}[\rho] = \int \rho(r)\varepsilon_{xc}(\rho)dr\,, \tag{2.34}$$

where $\varepsilon_{xc}(\rho)$ is the exchange and correlation energy per particle of a uniform electron gas of density $\rho(r)$. The functional derivative of $E_{xc}^{LDA}[\rho]$ gives the local approximation to the Kohn-Sham exchange-correlation potential:

$$v_{xc}^{LDA}(r) = \frac{\delta E_{xc}^{LDA}}{\delta\rho(r)} = \varepsilon_{xc}(\rho(r)) = \rho(r)\frac{\delta\varepsilon_{xc}(\rho)}{\delta\rho} \tag{2.35}$$

Hence the Kohn-Sham equation becomes

$$\left[-\frac{1}{2}\nabla^2 + v(r) + \int \frac{\rho(r')}{|r-r'|}dr' + v_{xc}^{LDA}(r)\right]\Psi_i = \varepsilon_i \Psi_i \tag{2.36}$$

The local exchange-correlation energy is simply the summation of exchange effect and the correlation effect.

$$\varepsilon_{xc}(\rho) = \varepsilon_x(\rho) + \varepsilon_c(\rho), \tag{2.37}$$

where $\varepsilon_x(\rho)$ is the exchange energy per particle of a homogenous electron gas, and known exactly as follows

$$\varepsilon_x(\rho) = -\frac{3}{4}\left(\frac{3}{\pi}\right)^{1/3}\rho(r)^{1/3} = -\frac{0.4582}{r_s}, \tag{2.38}$$

where the r_s is the mean interelectronic distance expressed in atomic units. The $\varepsilon_c(\rho)$ is the correlation energy per particle of a homogenous electron gas and many approximations for correlation are also available [59-62],

$$\varepsilon_c = \begin{cases} A\ln r_s + B + C\ln r_s + Dr_s, & r_s \le 1 \\ \gamma/(1+\beta_1\sqrt{r_s} + \beta_2 r_s), & r_s > 1 \end{cases}, \tag{2.39}$$

where for very dense electronic systems, A=0.0311, B=-0.048, C=0.002 and D=-0.0116 for spin-unpolarized and A=0.01555, B=-0.0269, C=0.007 and D=-0.0048 for spin-polarized case. Furthermore for low densities, γ=-0.1423, $\beta_{1=}$1.0529 and β_2=0.3334 for spin-unpolarized and γ=-0.0843, $\beta_{1=}$1.3981 and β_2=0.2611 for spin-polarized cases.

Furthermore the mean interelectronic distance is as follows:

$$r_s = (\frac{3}{4\pi\rho})^{1/3} \tag{2.40}$$

The LDA functional is further extended to the spin dependent situations by replacing the scalar external potential $v(r)$ by a spin dependent potential $v_{\alpha\beta}(r)$ and replacing the density $\rho(r)$ by the density matrix $\rho_{\alpha\beta}(r)$ [63-65]. The electron densities with spin projection up $\rho_\alpha(r)$ and down $\rho_\beta(r)$ are treated separately. This so-called local spin density approximation (LSDA) improved LDA for atomic and molecular systems with unpaired spins.

LDA and its spin generalization LSDA allow one to use the knowledge of the uniform electron gas to predict properties of the in homogenous electron gases occurring in atoms, molecules and solids. LSDA usually has moderate accuracy for most systems of interest, making errors of order 5-10%. Its most remarkable feature is its reliability, making the same kinds of errors on every system it's applied to. The success of LDA and LSDA is due to the fact that the exchange-correlation hole $\rho_{xc}^{LDA}(r_1, r_2)$ is spherically symmetric and it obeys the sum rule [64,66-68]. In other words, if an electron has been found at r_1 there is one less electron left to find elsewhere

$$\int \rho_{xc}^{LDA}(r_1, r_2) dr_2 = -1, \tag{2.41}$$

where the exchange-correlation hole $\rho_{xc}^{LDA}(r_1, r_2)$ is defined by

$$V_{ee} = \iint \frac{1}{r_{12}} \rho_2(r_1, r_2) dr_1 dr_2 = J[\rho] + \frac{1}{2} \iint \frac{1}{r_{12}} \rho(r_1) \rho_{xc}^{LDA}(r_1, r_2) dr_1 dr_2 \quad (2.42)$$

with $J[\rho]$ being the classical Coulomb interaction. This is true because for every r_1, $\rho_{xc}^{LDA}(r_1, r_2)$ is the exact exchange-correlation hole of a homogenous electron gas with density $\rho(r_1)$. Hence, the LDA and LSD describe the total charge of $\rho_{xc}^{LDA}(r_1, r_2)$ correctly.

2.6 Generalized Gradient Approximation

The LDA formula for E_{xc} is for systems with slow varying densities, and likewise for system with in-homogeneities, it is better to carry out an expansion of the density in terms of the gradient and higher order derivatives. Following expands the exchange-correlation functional in a Taylor series in gradients of the density and called gradient expansion approximation (GEA),

$$E_{xc}^{GEA}[\rho] = \int \rho(r) \varepsilon_{xc}(\rho) dr + \int C_{xc}(\rho) \frac{\nabla \rho}{\rho^{2/3}} dr + ... \quad (2.43)$$

As seen on equation 2.43 the first term in the expansion is LDA. It is expected that this expansion to be give a better approximation for LDA and it did not provide better results over LDA. There are two reasons for this. First, the GEA exchange-correlation hole improves the LDA hole only at short separations, but is poorly damped and oscillatory at large separations, and secondly GEA violates

the sum rule of the exchange-correlation hole. Accordingly, Perdew and others introduced the so-called generalized gradient approximation (GGA) such that the exchange correlation energy can be written as a functional of both the density and its gradient:

$$E_{xc}^{GGA}[\rho] = \int d^3 r f(\rho(r)\nabla\rho(r)) \tag{2.44}$$

The first modern GGA was that of Langreth and Mehl, who proposed the idea of truncating the gradient expansion for the exchange-correlation hole. Considering the problems encountered by GGA, Perdew *et al*. [69,70] proposed several versions of GGA functional by introducing the real-space cutoff procedure on the hole, which restores the sum rule or the normalization and negativity conditions on the GGA hole and generates a short-ranged hole whose angular and system average was much closer to the true hole. The Perdew-Wang 1991 (PW91) GGA functional [71] incorporates no free parameters and is entirely determined from uniform electron gas properties and extract constraints. The Perdew-Burke-Ernzerhof functional [72] is a simplified and refined version of the PW91 functional. Becke derived an exchange functional known as B88 [73,74] incorporating the known behavior of the exchange hole at large distances outside a finite system. Lee, Yang and Parr obtained the correlation energy as an explicit functional of the density and it's gradient and Laplacian, now generally known as the "LYP" functional [75].

These GGA functionals systematically improve the LDA and, in some calculations, approach the accuracy of CI methods, at much less computational cost.

2.7 Hybrid Density Functional Method

Considering the local or semi local nature of LDA and GGA, Becke proposed the so-called Hybrid Density Functional method which incorporates the exact treatment of exchange by Hartree-Fock theory with DFT approximations for dynamical correlation. This idea was motivated by re-examination of the adiabatic connection,

$$H_\lambda = T + \lambda V_{ee} + \sum_i v_\lambda(r_i), \tag{2.45}$$

where λ is an inter-electronic coupling-strength parameter that "switches on" the $1/r_{12}$ Coulomb repulsion between electrons. $\lambda = 0$ corresponds to the non-interacting Kohn-Sham reference system, while $\lambda = 1$ corresponds to the fully interacting real system, with $\rho(r)$ being fixed as the exact ground state density of H_λ. The $E_{xc}[\rho]$ can be written as

$$E_{xc}[\rho] = \int_0^1 d\lambda U_{xc}^{\lambda}[\rho], \tag{2.46}$$

where

$$U_{xc}^{\lambda}[\rho] = \left\langle \Psi_n^{\lambda} \mid V_{ee} \mid \Psi_n^{\lambda} \right\rangle - J[\rho] \tag{2.47}$$

The obvious first approximation for the λ dependence of the integrated in equation (2.46) is a linear interpolation, resulting in the Becke's half-and-half functional:

$$E_{xc}^{h\&h}[\rho] = \frac{1}{2}\left(U_{xc}^{0} + U_{xc}^{1}\right), \tag{2.48}$$

where U_{xc}^{o} is the exact exchange energy of the KS determinant and U_{xc}^{1} is the potential energy contribution to the exchange-correlation energy of the fully interacting system. This half and half functional has the merit of having a finite slope as $\lambda \to 0$, and it becomes exact if $E_{xc,\lambda=1}^{DFT}$ is exact and the system has high density. However, it does not provide a good quality of the total energy and the uniform gas limit is not obtained. Due to this Becke proposed the semi-empirical generalization of 3-parameter hybrid exchange-correlation functional

$$E_{xc}^{B3} = E_{xc}^{LSDA} + a_o(E_x^{exact} - E_x^{LSDA}) + a_x \Delta E_x^{GGA} + a_c \Delta E_c^{GGA}, \tag{2.49}$$

where a_o, a_x and a_c are semiempirical coefficients to be determined by an appropriate fit to experimental data. E_x^{exact} is the exchange energy of the Slater determinant of the Kohn-Sham orbitals. ΔE_x^{GGA} is the gradient correction for the exchange, and ΔE_c^{GGA} is the gradient correction for the correlation. Equation

(2.49) describes the Becke, three-parameter, Lee-Yang-Parr (B3LYP) that we used in many of our SiGe calculations.

2.8 Strong correlations: LDA+U or GGA+U

Third row transition metal oxides are characterized specifically for their well-localized d orbitals. These well-localized d orbitals lead to strong on-site correlations. For example, when an electron is occupying a state localized in a particular site, placing another electron at the same site cost an additional energy of U. This was first traversed by Hubbard at the level of an empirical Hamiltonian and much attention has been granted ever since. The Hubbard approach has been combined with DFT calculations by supplementing the LDA or GGA with a Hubbard U parameter for LDA+U or GGA+U (on site repulsion term)[76].

$$E_{GGA+U} = E_{GGA} - \frac{1}{2}UN(N-1) + \frac{1}{2}U\sum_{i\neq j} f_i f_j \,, \tag{2.50}$$

where f_i are orbital occupancies and the model splits into two sub-bands. In addition the eigenvalues are given by

$$\varepsilon_i = \frac{\partial E_{GGA+U}}{\partial f_i} = \varepsilon_{GGA} + U(\frac{1}{2} - f_i)\,, \tag{2.51}$$

where the energy separation given by the Hubbard U parameter reproduces the behavior of Mott-Hubbard insulators and the strong correlation induces the band gap opening.

For the work done on SiGe nanostructures, as mentioned earlier, we have mainly used B3LYP hybrid functional as implemented in GAUSSIAN suite of programs for the clusters. It is well known that B3LYP functional is excellent in predicting semiconductor structures, specifically the band gaps. However, it is also known to deviate in extended systems. Hence when the periodic boundary conditions are applied for the structures, we have used HSE06 hybrid functional. Furthermore when we studied the hematite structures, which belong to transition metal oxide category, we have used the GGA+U approach implemented in VASP.

Chapter 3

Single Walled Armchair SiGe Nanotubes

3.1 Introduction

Both silicon and germanium reside in column IV of the periodic table and are isoelectronic to carbon. Hence, progressively increasing research is currently being pursued in the area of nanotubular forms of these elements [77-88]. We have found that Si nanotubes are stable and semiconducting in nature irrespective of chirality. In addition, Ge nanotubes of both armchair and zigzag configurations, are also semiconducting [83,84].

A more complicated atomic arrangement of Si and Ge in tubular forms; SiGe nanotubes (a hybrid structure) and one dimensional structure in the form of SiGe nanowires have also been the focus of scientific community very recently. Migas and Borisenko showed that SiGe and Si-Ge core-shell nanowires with the <001> orientation and a diameter of 1.5 nm display a competitive indirect-direct character of the gap [89]. To show the unique features of SiGe nanotubes, Schmidt and Eberl created these tubes using two different methods, called a ‘general’ and a ‘specialized’ method [90]. From the ‘general’ method they were able to prepare nanotubes, which yielded an aspect ratio of 60 and by involving the ‘specialized’ method, they were able to prepare nanotubes of length 20μm with a diameter of 530nm. Molecular dynamics simulations done by Zang *et al.*

[91] demonstrated that a free standing Si nanofilms may bend into a nanotube with Ge as inner layer, opposite to the normal bending configuration defined by misfit strain. They also observed that such rolled-up nanotubes can accommodate a high level of strain, even beyond the magnitude of lattice mismatch. Recently, graphene-like structure from Si (silicene sheet) grown on top of closed packed silver surface Ag (111) has been discovered [92]. They claimed the synthesized silicene is highly ordered Si honey-comb structure with possible sp^2-sp^3 bonding. Following the same path, it should be possible to make Ge, SiGe honey-comb structures. Hence the rolling-up Si, Ge or SiGe honey-comb structures to build NTs should be possible experimentally.

3.2 Computational method and construction of SiGe nanotubes

Hybrid density functional theory incorporating Hartree-Fock (HF) exchange [52,53] with density functional theory (DFT) exchange-correlation has proved to be an efficient method for many systems. It has been reported that hybrid functionals can reproduce the band gaps of semiconductors and insulators quite well [93,94]. In this current work we have used hybrid density functional theory to study the electronic and geometric structure properties of SiGe nanotubes, represented by finite clusters with dangling bonds saturated by hydrogen atoms. Furthermore we have used the hybrid functional B3LYP [73,75],

and all electron 6-31G**//3-21G* [95] basis set as implemented in the GAUSSIAN 09 suite of software [48]. Because of severe demands on computational resources in an all-electron calculations for a large cluster, the geometries were first optimized with the 3-21G* basis set and then single-point energy runs have been performed with the 6-31G** set. We note here that, as is known, geometrical parameters are not highly sensitive to the choice of the basis set. The SiGe nanotubes have been represented by finite clusters with dangling bonds terminated by hydrogen atoms. All structures reported here are *geometry as well as spin optimized* with the density convergence criterion set at 10^{-6} a.u.

The starting geometries of these tubular structures have been obtained by simply rolling graphene like sheets of Si and Ge atoms placed at different nodes of the *honeycomb* lattice to form a tube. Among the vast family of nanotubes the two most simple and highly studied cases are armchair and zigzag; both are achiral nanotubular forms. In the (*n*,*n*) armchair tubes the two sides of each hexagons are perpendicular to the tubular axis, whereas in *(n*,0) zigzag, the two sides of each hexagons are parallel to the tube axis [2].

With distinct atomic arrangements, these nanotubular morphologies can be categorized in four “types”, namely types I, II, III and IV (refer Figure 3.1). In type I, alternating Si and Ge atoms have only Ge or Si atoms as nearest neighbors. In types II and III, the nearest neighbors surrounding each Si atom consists of two Ge atoms and another Si atom and vice-versa. The difference between type II and

type III SiGe nanotubes lies in the fact that in type II nanotubes, any layer (ring of atoms) perpendicular to the nanotube axis contains only one kind of atoms, either Si or Ge. But in type III, the same kind of layer will contain alternating Si and Ge atoms. First three types (I-III) of SiGe armchair NTs have been previously studied by Somil and Ray [96] using the same hybrid functional, B3LYP but with the Los Alamos pseduopotential basis set LANL2DZ. In this work, a *new type* IV SiGe NT is proposed to have the nearest neighbor surroundings exactly opposite to those of types II and III, namely that the nearest neighbors surrounding each Si atom consists of two Si atoms and one Ge atom and *vice versa*. In particular, this atomic arrangement in type IV tubes makes Si and Ge layers parallel to the tube axis (refer Figure 3.1).

Finally, from the perspective of atomic bond types, type I has one kind of bonds present throughout the nanotube, namely Si-Ge bond, whereas types II, III and IV have, in addition, Ge-Ge, and Si-Si bonds. However, for a given size, type IV has the highest number of homo-nuclear bonds. This type IV configuration is only possible due to close range bond distances of Si-Si, Ge-Ge and Si-Ge which is about 2.30-2.40Å. For example type IV is not possible with SiC nanotubes, since strong C-C bond distance is around 1.34Å and Si-C around 1.84Å and Si-Si around 2.30Å. The large variation in bond distances can cause deformations and absence of tubular shapes.

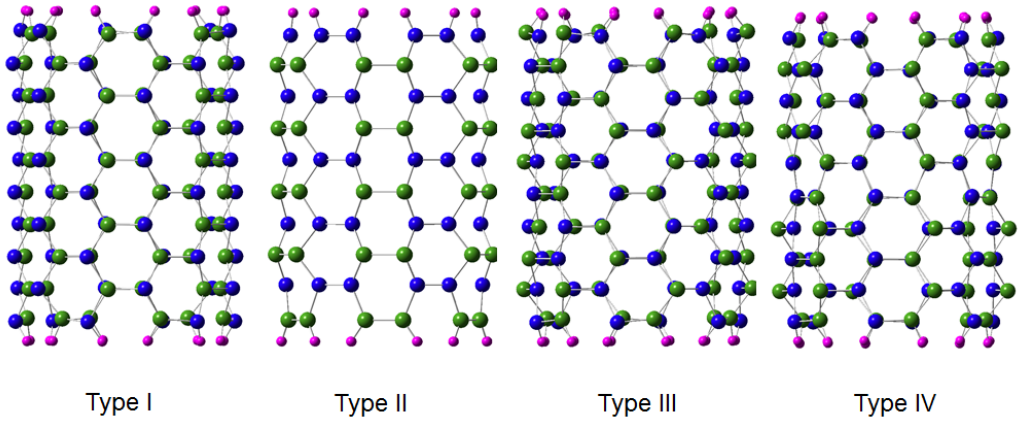

Figure 3.1: Side views of SiGe(6,6) four types of nanotubes. H atoms in pink, Si atoms in blue and Ge atoms in green color.

The smallest SiGe conformation studied here is an armchair (3,3) tube, represented by a cluster $Si_{30}Ge_{30}H_{12}$, and the largest is a (11,11) tube represented by the cluster $Si_{110}Ge_{110}H_{44}$. We first calculated the binding energy per atom in the separated atom limit by using equation 3.1.

$$E_b = [n (E_{si} + E_{Ge}) + m (E_H) – E_T]/ (2n + m), \quad (3.1)$$

where E_{Si} is the ground state energy of the Si atom, E_{Ge}, E_H, and E_T are the corresponding total energies of the Ge atom, H atom, and of the nanotube, n is the number of Si (Ge) atoms and m is the number of H atoms in the tube.

3.3 Results and discussion

The binding energies calculated using equation 3.1 is shown in Table 3.1. In addition Figure 3.2 shows the plotted binding energies obtained for all four types of nanotubes. Comparing SiGe (3,3) through SiGe (11,11) of types I-IV nanotubes it is evident that the trend indicates saturation in the binding energy with an increase in tube diameter and this is the same trend reported by Somil and Ray [96]. However, in the present data, the tubes of all four types with lowest diameters show the highest binding energy. For example, the binding energy per atom of a (3,3) type I tube is 3.508 eV and 3.389 eV for a (11,11) tube. For the newly proposed type IV tube, the binding energy per atom for (3,3) and (11,11) are 3.495 eV and 3.411 eV, respectively. In the present calculations, SiGe (3,3)

tubes were found to have higher average bond energy compared to other tubes leading, in general, to higher binding energies.

By arranging the atoms in a honey-comb structure, we imposed sp^2 hybridization on Si and Ge atoms. In order to find the hybridization of Si and Ge atoms after optimization, we performed a NBO (natural bond orbital) analysis [97] and bond angle analysis on these nanotube structures. In Table 3.2 and Table 3.3 we report the angle-based hybridization analysis results of Si and Ge atoms on these nanotubes, respectively. Typical sp^3, sp^2 and p bond angles are ~109.5, 120 and 90 degrees. However, when determining the angles of these bonds, we considered a range instead of one value to determine the hybridization. Therefore, angles within 99.75-114.75 degrees considered as sp^3 hybridized and any angle below 99.75 degrees considered as p hybridized and any angle above 114.75 degrees considered as sp^2 hybridized atom. Si atoms in all types have gained the sp^3 hybridization except type II (10,10) and (11,11) tubes.

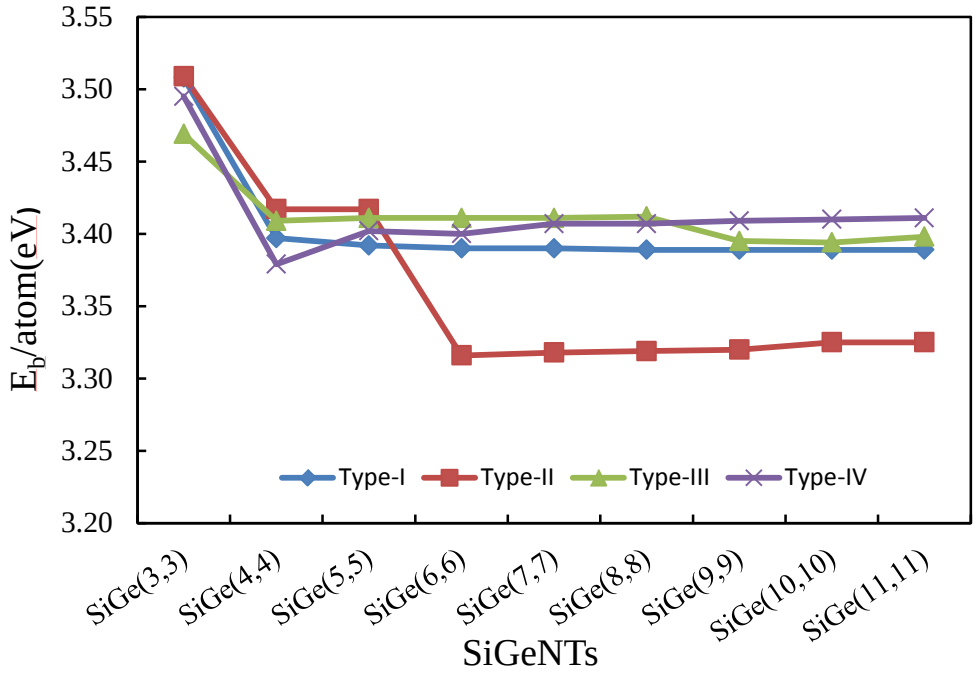

Figure 3.2: Binding energy per atom with respect to number of atoms in the tube.

Table 3.1: Binding energies per atom in eV of type I-IV for SiGe nanotubes

System	Stoichiometry	Binding energies per atom (eV)			
		Type-I	Type-II	Type-III	Type-IV
SiGe(3,3)	Si_{30} $Ge_{30}H_{12}$	3.508	3.509	3.469	3.495
SiGe(4,4)	Si_{40} $Ge_{40}H_{16}$	3.397	3.417	3.409	3.379
SiGe(5,5)	Si_{50} $Ge_{50}H_{20}$	3.392	3.417	3.411	3.402
SiGe(6,6)	Si_{60} $Ge_{60}H_{24}$	3.390	3.316	3.411	3.400
SiGe(7,7)	Si_{70} $Ge_{70}H_{28}$	3.390	3.318	3.411	3.407
SiGe(8,8)	Si_{80} $Ge_{80}H_{32}$	3.389	3.319	3.412	3.407
SiGe(9,9)	Si_{90} $Ge_{90}H_{36}$	3.389	3.320	3.395	3.409
SiGe(10,10)	Si_{100} $Ge_{100}H_{40}$	3.389	3.325	3.394	3.410
SiGe(11,11)	Si_{110} $Ge_{110}H_{44}$	3.389	3.325	3.398	3.411
Avg. binding energy/atom		3.404	3.363	3.412	3.413

In addition at high curvature nanotubes (SiGe (3,3), (4,4) and (5,5)) in all four types Si atoms makes p hybridizations. We also note that several Ge atoms in type IV tubes, higher diameter type III tubes, type II (3,3), and type III (3,3) tubes bond through p orbitals. In general, Ge atoms in all four types make sp^3 hybridized atoms and number of p orbital bonded Ge atoms is higher than the Si atoms. From the NBO orbital analysis it is realized that these orbitals have approximately 10% s character and 90% p character. Also they have lone pairs made of about 80% s character and 20% p character. This is a rather new observation in the area of nanotubes indicating that these Si and Ge atoms go through the dehybridization process, consistent with some previous observations for other systems [98,99] Probability in making sigma p orbital bonding is high in type IV tubes since number of Ge-Ge bonds are high compared to other types. Since type I only have Si-Ge bonds and probability for p orbital sigma bonds is very law at higher diameter nanotubes. Figure 3.3 shows the NBOView [100] plots generated from these tubes. 3D rendered contours clearly show that the 90% p orbitals make sigma bonds leading to higher bond strengths.

Table 3.2: Hybridization of Si atoms in all four types of SiGe nanotubes. Hybridization is presented as a percentage of total hybridization.

System – number of total Si atoms in the system	Type-I			Type-II			Type-III			Type-IV		
	sp^2	sp^3	p	sp^2	sp^3	p	sp^2	sp^3	p	sp^2	sp^3	p
SiGe (3,3) - 30	30	61	9	41	33	26	27	67	7	27	63	10
SiGe (4,4) - 40	5	60	35	28	50	22	30	48	22	55	28	17
SiGe (5,5) - 50	0	87	13	30	70	0	40	60	0	60	40	0
SiGe (6,6) - 60	0	100	0	67	33	0	44	56	0	60	40	0
SiGe (7,7) - 70	0	100	0	79	21	0	64	36	0	53	47	0
SiGe (8,8) - 80	0	100	0	73	27	0	47	53	0	60	40	0
SiGe (9,9) - 90	0	100	0	73	27	0	57	43	0	69	31	0
SiGe (10,10) - 100	0	100	0	100	0	0	63	37	0	59	41	0
SiGe (11,11) - 110	0	100	0	100	0	0	67	33	0	72	28	0

Table 3.3: Hybridization of Ge atoms in all four types of SiGe nanotubes. Hybridization is presented as a percentage of total hybridization.

System – number of total Ge atoms in the system	Type-I			Type-II			Type-III			Type-IV		
	sp^2	sp^3	p	sp^2	sp^3	p	sp^2	sp^3	p	sp^2	sp^3	p
SiGe (3,3) - 30	3	70	27	20	63	17	7	63	30	7	83	10
SiGe (4,4) - 40	57	25	18	27	33	40	30	38	32	32	28	40
SiGe (5,5) - 50	67	33	0	33	33	34	33	50	17	37	37	26
SiGe (6,6) - 60	67	33	0	13	87	0	33	60	7	40	33	27
SiGe (7,7) - 70	67	33	0	21	79	0	27	73	0	40	40	20
SiGe (8,8) - 80	67	33	0	20	80	0	33	67	0	36	56	7
SiGe (9,9) - 90	67	33	0	20	80	0	34	62	4	37	61	2
SiGe (10,10) - 100	67	33	0	53	47	0	37	63	0	32	66	2
SiGe (11,11) - 110	67	33	0	61	39	0	31	67	2	28	70	2

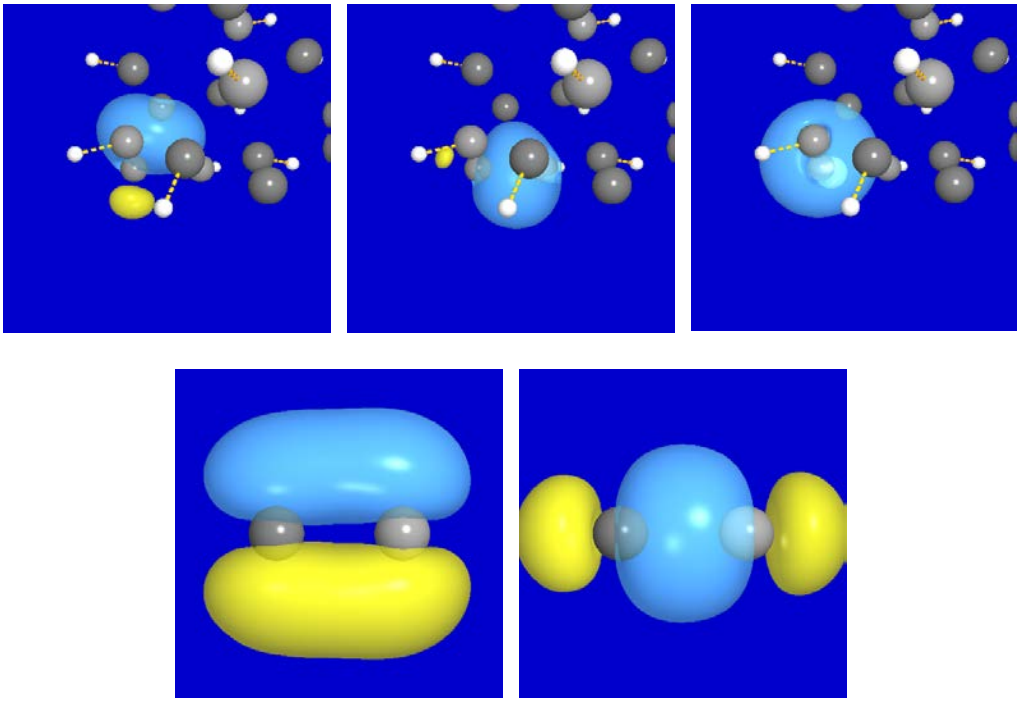

Figure 3.3: Upper three figures show the bonds made by a dehybridized Ge atom. All of them have over 90% p character. Si atoms are in dark gray color, Ge atoms in light gray color and H atoms in white color. Last two show p orbitals making pi bond and sigma bonds.

We also studied the HOMO-LUMO gaps to identify the conducting nature of the tubes. From the plot of HOMO-LUMO gaps in Figure 3.4, we can see all these tubes are semiconducting in nature and in general as diameter increases (increase of number of atoms implies increase of tube diameter) HOMO-LUMO gap decreases and saturate. The HOMO-LUMO gap of type I tubes saturate at around 1.0 eV and type IV tubes indicate the lowest saturation gap of about 0.47 eV. This wide spread nature of HOMO-LUMO gaps indicate higher potential of the SiGe nanotubes in the field of band gap engineering. Also our results have the same trend reported by Somil and Ray [96]. However our results are lower in value and it is expected to have lower values since use of all electron basis set give rise to more core and valence orbital overlapping which result in small band gaps. In Tables 3.4 and 3.5, we report the diameters and radial buckling obtained for all four types of relaxed tubes. Diameters are of the same order of magnitude for particular chiral indices regardless of the type they are in. However only type IV indicates approximate convergence in radial buckling as tube diameter increases.

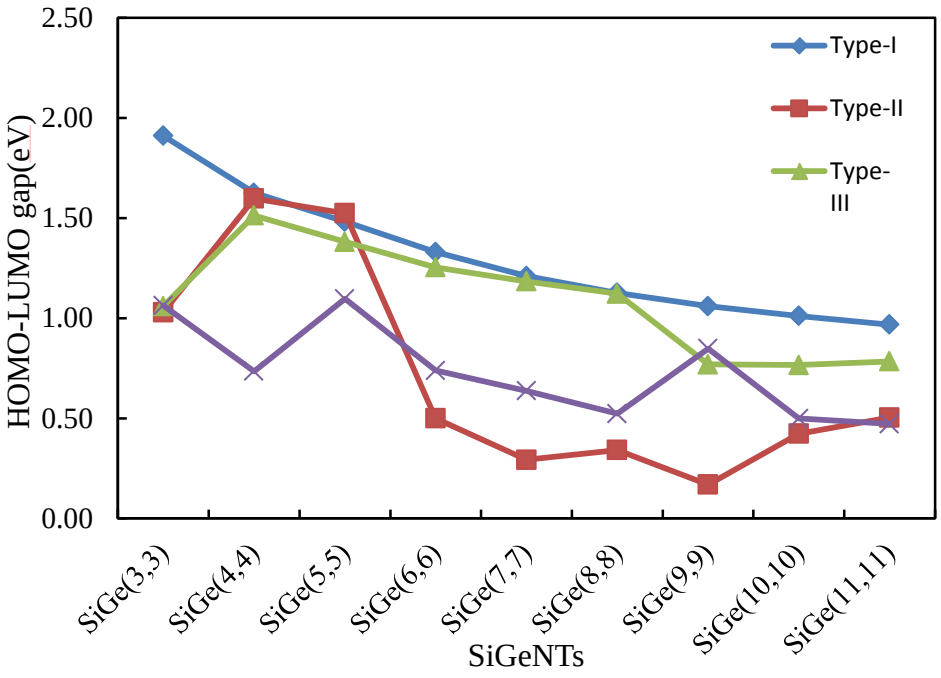

Figure 3.4: HOMO-LUMO gap variation with respect to number of atoms in the tube.

Table 3.4: Tube diameter in Å for type I-IV of SiGe armchair nanotubes.

System	Stoichiometry	Tube diameter (Å)			
		Type-I	Type-II	Type-III	Type-IV
SiGe (3,3)	$Si_{30}Ge_{30}H_{12}$	6.192	6.044	6.088	5.975
SiGe (4,4)	$Si_{40}Ge_{40}H_{16}$	11.742	11.662	11.650	10.361
SiGe (5,5)	$Si_{50}Ge_{50}H_{20}$	12.648	12.556	12.550	12.529
SiGe (6,6)	$Si_{60}Ge_{60}H_{24}$	13.598	13.324	13.499	12.875
SiGe (7,7)	$Si_{70}Ge_{70}H_{28}$	14.615	14.406	14.977	14.992
SiGe (8,8)	$Si_{80}Ge_{80}H_{32}$	17.221	16.692	17.105	17.133
SiGe (9,9)	$Si_{90}Ge_{90}H_{36}$	19.379	19.471	18.795	19.304
SiGe (10,10)	$Si_{100}Ge_{100}H_{40}$	21.539	21.278	21.346	21.308
SiGe (11,11)	$Si_{110}Ge_{110}H_{44}$	23.699	23.550	23.291	23.390

Table 3.5: Radial buckling in Å for type I-IV for SiGe nanotubes.

System	Stoichiometry	Radial buckling(Å)			
		Type-I	Type-II	Type-III	Type-IV
SiGe (3,3)	$Si_{30}Ge_{30}H_{12}$	0.608	0.376	0.914	0.619
SiGe (4,4)	$Si_{40}Ge_{40}H_{16}$	0.326	0.030	0.075	1.091
SiGe (5,5)	$Si_{50}Ge_{50}H_{20}$	0.336	0.036	0.043	0.163
SiGe (6,6)	$Si_{60}Ge_{60}H_{24}$	0.337	0.322	0.030	0.168
SiGe (7,7)	$Si_{70}Ge_{70}H_{28}$	0.341	0.356	0.204	0.146
SiGe (8,8)	$Si_{80}Ge_{80}H_{32}$	0.666	0.783	0.097	0.107
SiGe (9,9)	$Si_{90}Ge_{90}H_{36}$	0.660	0.384	0.080	0.095
SiGe (10,10)	$Si_{100}Ge_{100}H_{40}$	0.656	0.337	0.178	0.082
SiGe (11,11)	$Si_{110}Ge_{110}H_{44}$	0.652	0.270	0.191	0.064

In Figure 3.5, we have plotted the HOMOs and LUMOs of some of these nanotubes. It indicates for type I, localized nature in the electrons and for type IV, slightly delocalized nature. After relaxing the structures, average bond distances for Si-Si, Ge-Ge and Si-Ge are about 2.30Å, 2.37Å and 2.35Å respectively. These distances are large compared to CNTs or SiC nanotubes. Additionally the sp^3 hybridization state which atoms are in makes the electrons to be localized to their respective atoms unlike CNTs. Also using Gausssum-2.2.5 program [101], we plotted the density of states (DOS) and partial density of states (pDOS) for two sets of nanotubes (refer Figures 3.6-3.11). First set is SiGe (3,3) all four types and second set is SiGe (6,6) types I and IV. We chose these SiGe (3,3) nanotubes for the reason the reason of being highly puckered (another indication of atoms are changed of imposed sp^2 to sp^3 or p hybridization) and having equal number of hybridization on each category. On the other hand SiGe (6,6) types I and IV tubes were chosen to observe the contribution to HOMO-LUMO gap from different atom sections as diameter increases. Since when we increase the tube diameter type I, II and III behave similarly only one nanotube category was chosen. In every case we grouped the atoms into atoms from edges, H atoms and special bonding (sp^3, sp^2 or p). Also DOS are normalized into 1 atom where we can directly compare effects from a group. In all DOS plots, we note that the effect on HOMO and LUMO from H atoms is very low. This implies saturation of dangling bonds from H atoms will not change characteristics of the nanotubes. Also at

lower diameter edge effects are very low. In type I SiGe (3,3), sp^3 hybridization atoms are also edge atoms and we can conclude that if Si or Ge atoms are in sp^3 hybridization states, their contributions to HOMO and LUMO are very low. However with increase of tube diameter, contributions of edge atoms effects are considerable at gap region. In all of these tubes p bonding atoms (if available) have high contribution to HOMO and LUMO. Identification of these atomic contributions to LUMO will be very helpful when using these tubes as storage materials. We can specifically target these high contributing atoms as the storing locations. We also plotted the Mulliken charge distributions and it is shown in Figure 3.13. Since electron negativity of Si is around 1.90 and for Ge is around 2.01, we expect Ge to gain charge and Si to lost charge. This is what we observe in our plots where all the Ge atoms gain charge.

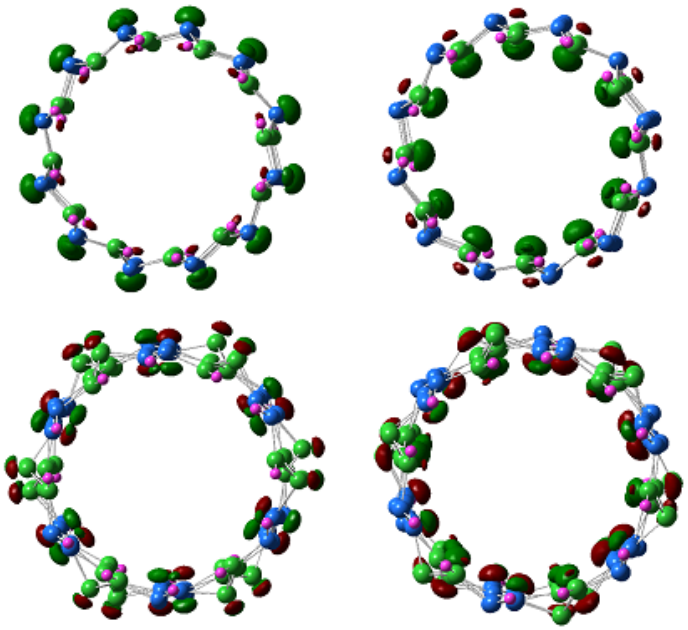

Figure 3.5: HOMO and LUMO plots of SiGe (6,6) type I and type IV. Top plots are SiGe (6,6) type I HOMO and LUMO. Bottom plots are SiGe (6,6) type IV HOMO and LUMO respectively.

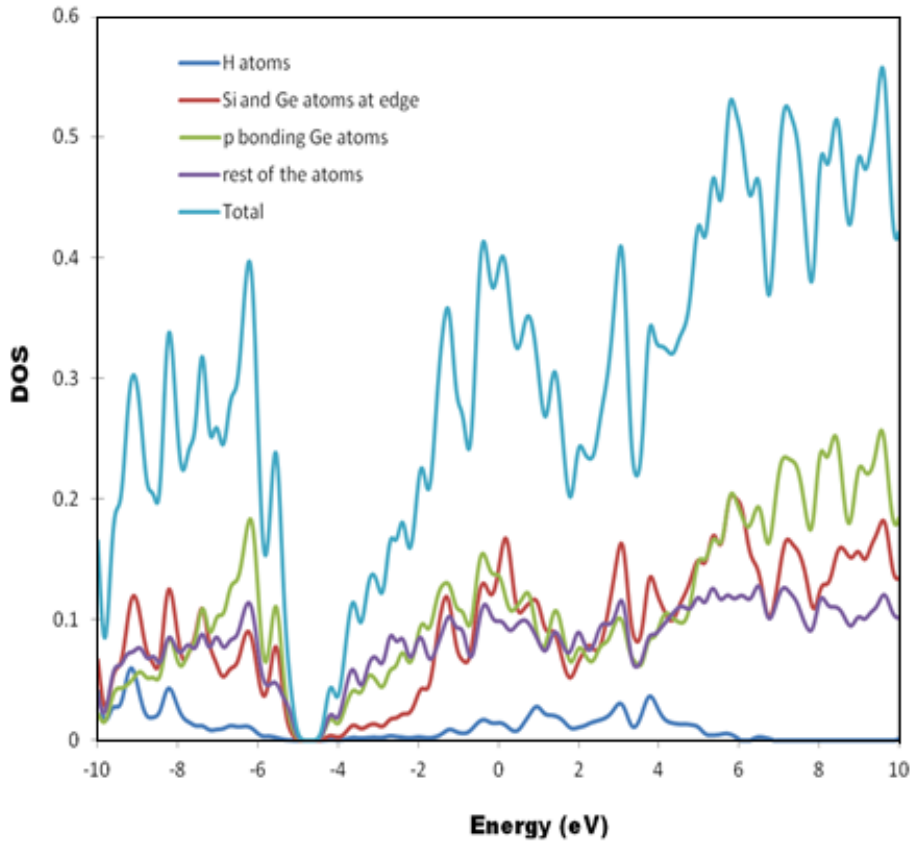

Figure 3.6: DOS plots of SiGe (3,3) type I nanotube. E_F is around -5.0eV.

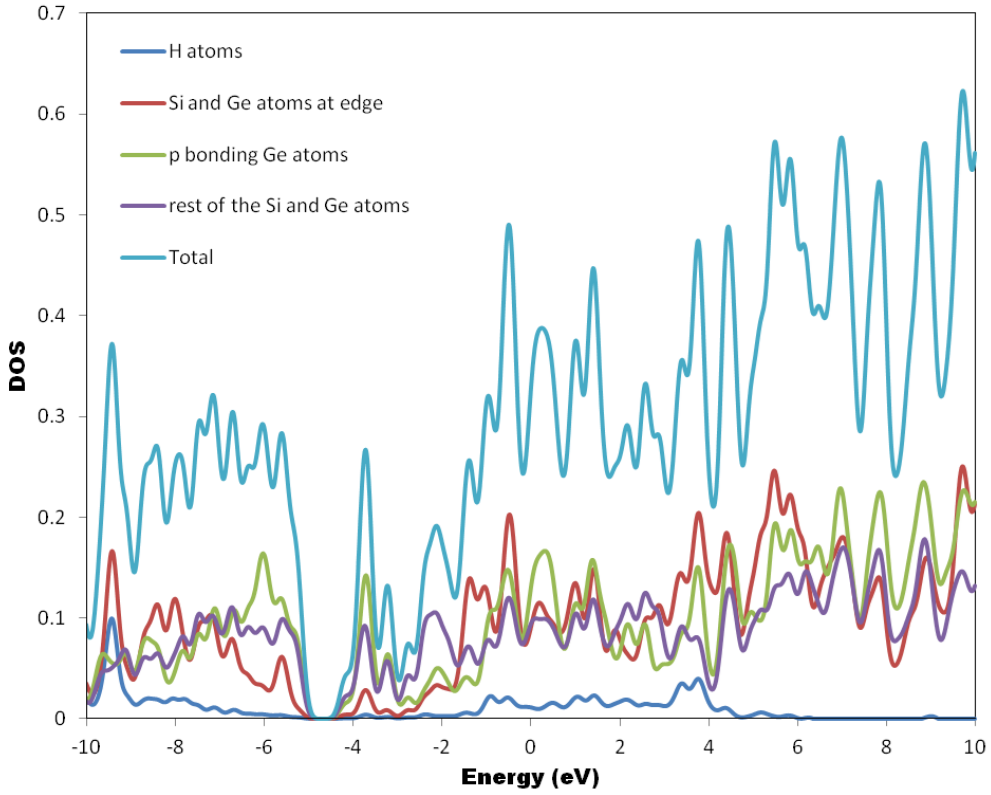

Figure 3.7: DOS plots of SiGe (3,3) type II nanotube. E_F is around -5.0eV.

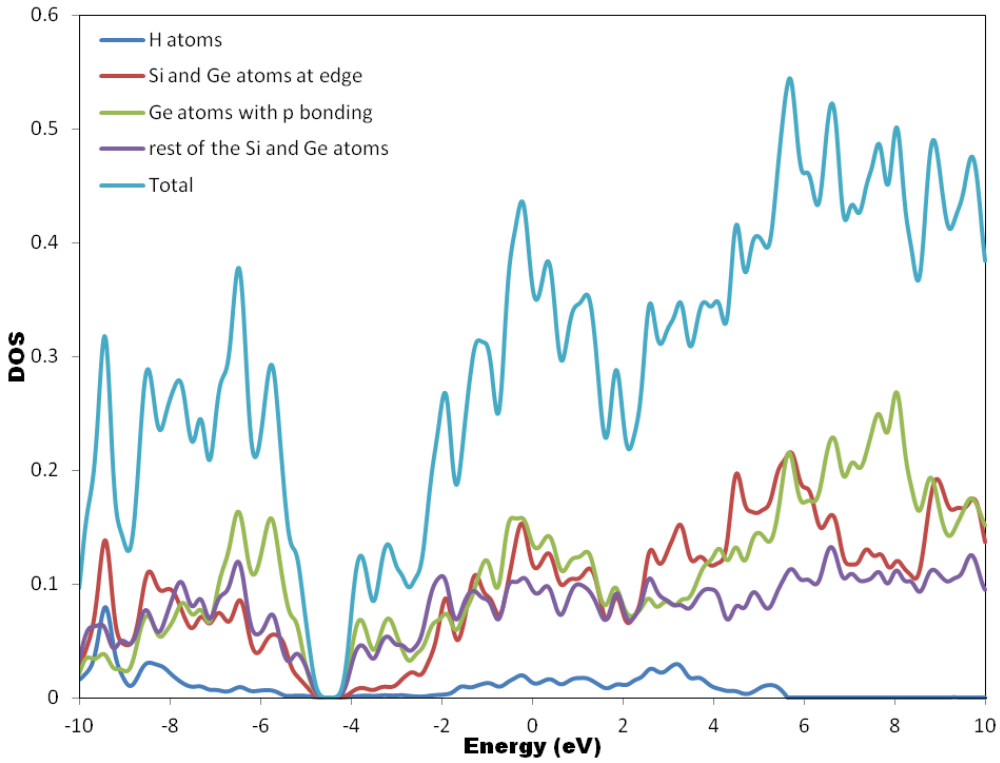

Figure 3.8: DOS plots of SiGe (3,3) type III nanotube. E_F is around -5.0eV.

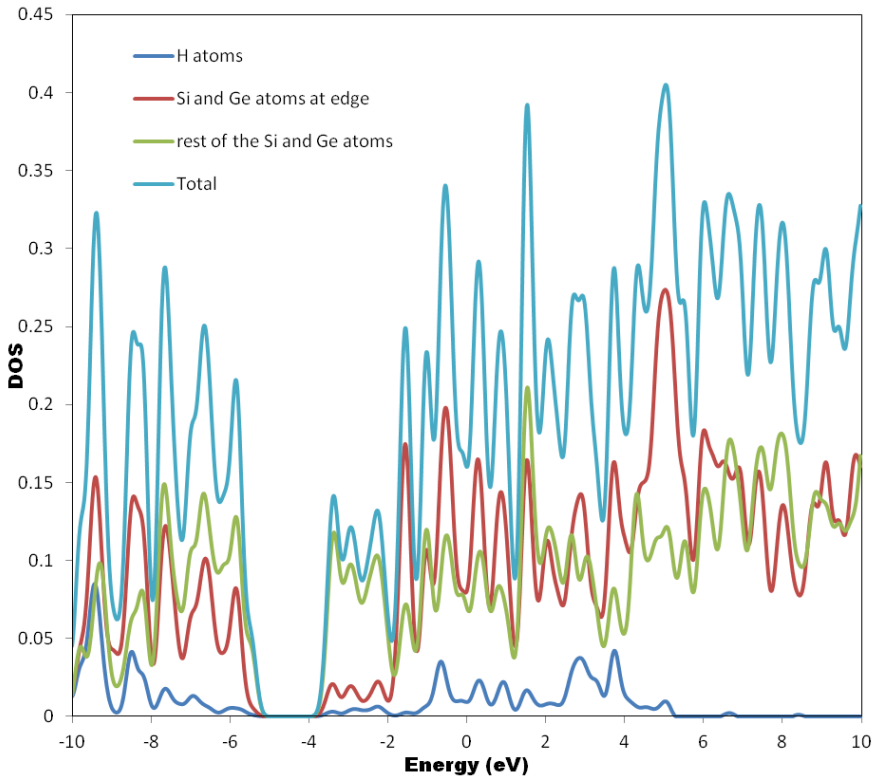

Figure 3.9: DOS plots of SiGe (3,3) type IV nanotube. E_F is around -5.0eV.

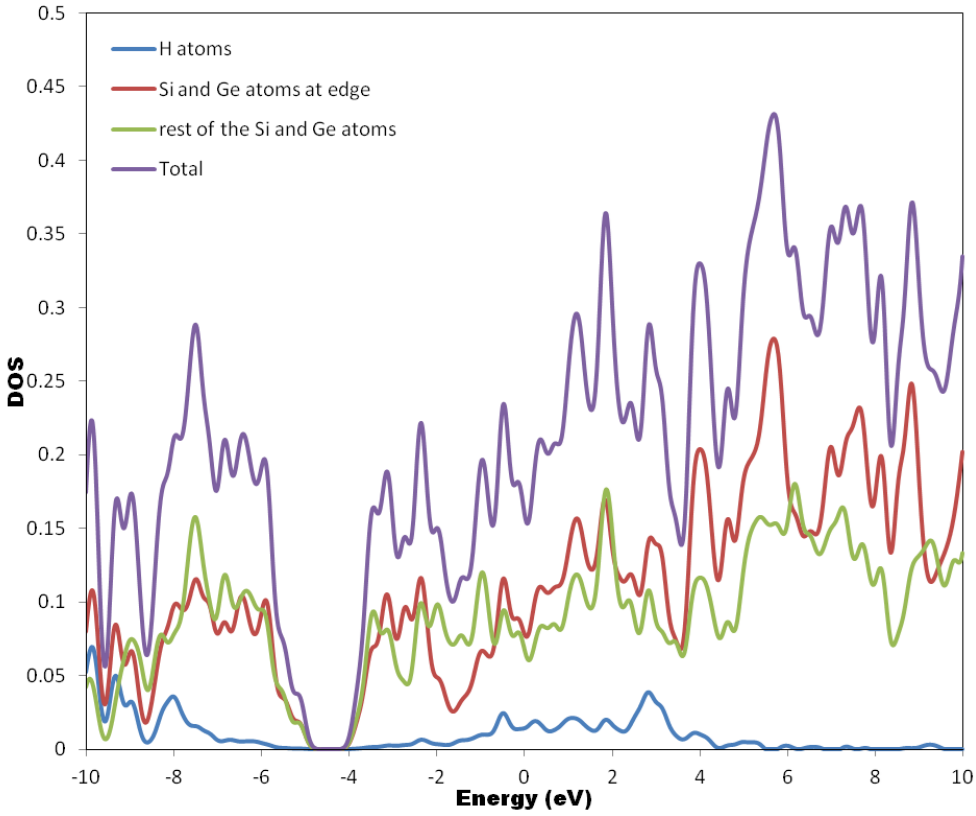

Figure 3.10: DOS plots of SiGe (6,6) type I nanotube. E_F is around -5.0eV.

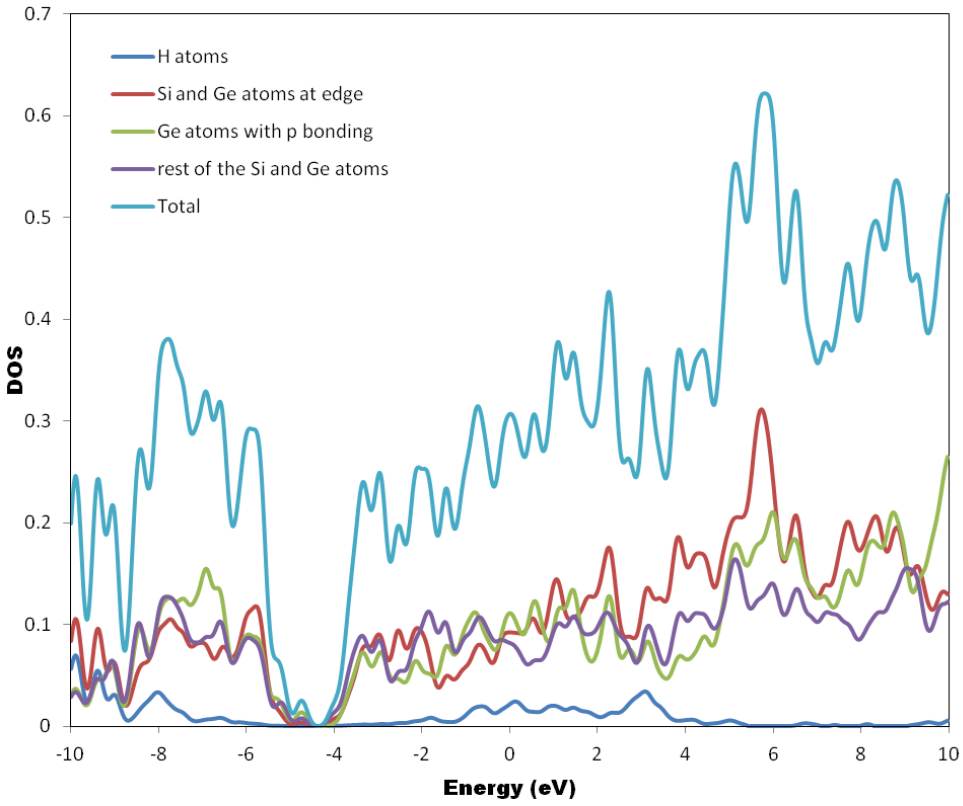

Figure 3.11: DOS plots of SiGe (6,6) type IV nanotube. E_F is around -5.0eV.

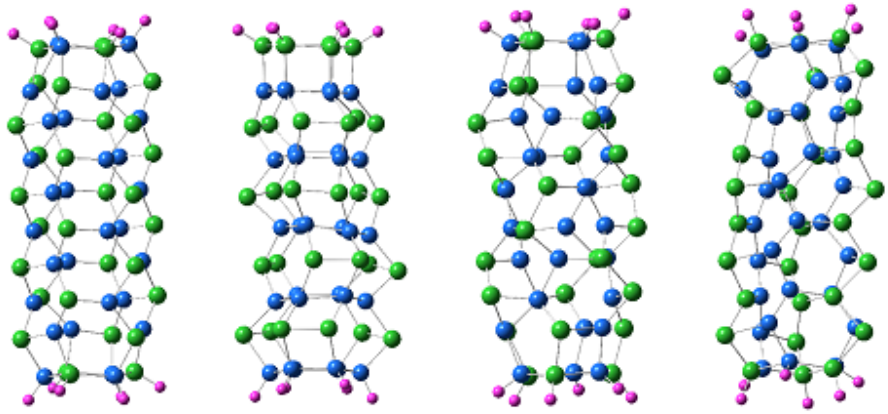

Figure 3.12: Side view of SiGe (3,3) type I, II, III and IV tubes respectively.

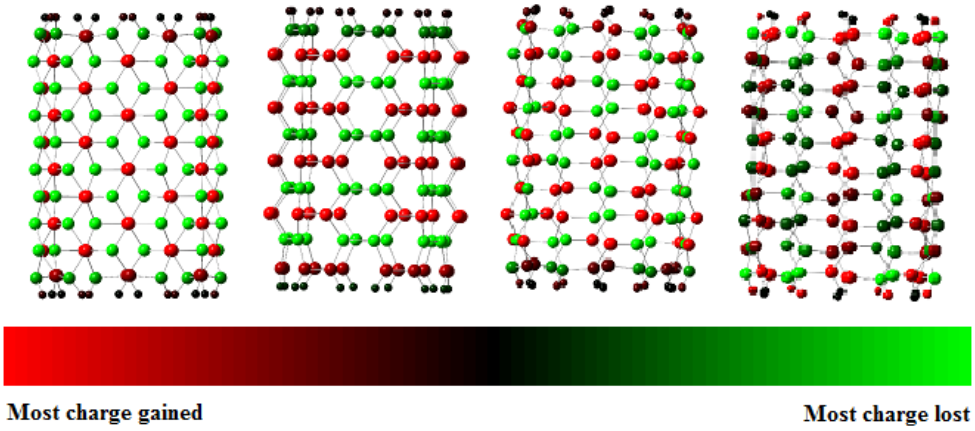

Figure 3.13: Mulliken charge distributions for SiGe (6,6) nanotubes from type I, II, III and IV.

Chapter 4

Interaction of a Single Li Atom with Single Walled SiGe (6,6) Nanotubes

4.1 Introduction

One of the interesting applications of nanotubes is its application in the area of rechargeable Li ion battery technology. The hollow interior of NTs creates a quasi-one-dimensional diffusion path for Li ions, and due to nanotube's curvature, externally adsorbed Li ions have more screening with each other. These factors result in fast kinetics and high Li ion capacity, respectively. Carbon electrodes made out of graphite is the current commercialized anode material, and exhibit excellent properties such as flatter discharge curve, higher capacity of Li ions, and long term cyclic ability [102]. However, there are number of materials, which capable of producing higher Li ion capacity than the theoretical maximum capacity of graphite [103-106].

Among many nanotube materials, Si nanotubes with hexagonal lattice structure are very promising [107]. Compared to graphite, SiNTs have very high capacity. However, experimental evidence shows that during charging and discharging cycles, SiNTs exhibit a large volume change which may lead to a structural deformation. Nevertheless, Song *et al.* [107] showed, that the use of Si hemisphere terminated SiNTs can reduce the large volume change significantly.

Due to the high charge transfer rate of Si, the release rate of Li ions in a Si based material is higher than any C based anode materials. Therefore, the amount of power available with the Si based anode material is high. Furthermore, Song *et al.* [107] reported the use of SiGe double layered NTs, where inner layer made out of Si and outer layer made out of Ge can deliver better results when used as the anode material. The use of the Ge layer not only increased the electrical conductivity and Li ion diffusivity but also reduced the vast volume change associated with SiNT.

As mentioned in Chapter 3, rolling of the SiGe hybrid nanosheets may use to create another form of SiGeNTs [90]. In the method developed by Schmidt and Eberl [90], the number of walls in a NT can be controlled precisely. These SiGeNTs are reported to have high thermal stability, high aspect ratios, precisely known wall thicknesses, and lengths. Due to different atomic arrangements, it is possible to have four different types of NTs. As discussed in Chapter 3, all four types were stable and semiconducting in nature. In this work, we present systematic studies done on the interactions between those SiGeNTs and a single Li atom. The purpose is to identify the SiGeNT ability to perform as anode material in Li ion batteries.

4.2 Results and discussion

We have carried out this work with the same functional B3LYP [73,75] as implemented in the GAUSSIAN 09 [48]. Because of severe demands on computational resources in an all-electron calculations for a large cluster, the geometries were first optimized with the 3-21G* basis set followed by single-point energy runs with the 6-311G** basis set [95]. We note here that, as is known, geometrical parameters are not highly sensitive to the choice of the basis set. All structures reported here are geometry as well as spin optimized with the energy convergence criterion set at 10^{-6} a.u.

The SiGe nanotubes for Li adsorption were created using the same method as discussed in Chapter 3 and before introducing the Li atom, the SiGe nanotube structures were fully optimized. From our study on SiGeNTs size (3,3) (cluster of $Si_{30}Ge_{30}H_{12}$) through (11,11) (cluster of $Si_{110}Ge_{110}H_{44}$) revealed that the binding energy per atom for all four types showed saturation from NT size (6,6) onwards (refer chapter 3, Figure 3.2). Additionally, we were able to identify, from the HOMO-LUMO gaps as shown in Figure 3.4, all those SiGe nanotubes are semiconducting in nature and in general, as diameter increases (increase of number of atoms implies increase of tube diameter) HOMO-LUMO gap tends to decrease with some oscillations. Considering all these factors and the associated computational costs of all-electron computations, we have selected NT size (6,6) in order to study the interaction of SiGeNTs with Li, The assumption here is that

this would accurately represent the entire range of SiGeNTs and their interactions with Li. Furthermore, by choosing a bigger NT size, for example (8,8) or (10,10), no additional chemically or physically information will be obtained.

Figure 4.1 shows the input sites considered for Li atom to adsorb in all four types of nanotubes. Those Li atom positions were common for both internal and external adsorptions. For type I, there were five different adsorption sites, Hollow (where Li lies in the middle of a hexagonal ring), Si Top, Ge Top, Si-Ge Normal Bridge, and Si-Ge Zigzag Bridge sites. Bridge site orientations were determined with respect to tube axis (red lines in Figure 4.1). For type II, we were able to identify 7 possible initial adsorption sites. Among those 7 sites, 3 sites were already identified in type I (Si Top, Ge Top, Si-Ge Bridge). The new sites were on Si-rich Hollow, Ge-rich Hollow, on Si-Si Bridge and Ge-Ge Bridge. There were six adsorption sites in types III and IV: Hollow, Si Top, Ge Top, Si-Ge Bridge, Si-Si Bridge, and Ge-Ge Bridge. Initial bond lengths from Li to the respective sites were set to be 2.7Å and this was determined following the experimental observations of Li-Si and Li-Ge bond lengths.

After optimization, we found that the structures followed two trends: structures retaining the tubular form with small local deformations and structures not retaining the tubular form with large deformations. Since the non-tubular forms do not convey any significant chemical and physical information regarding

their usage towards the Li ion battery technology, we present results primarily for the first kind and at the end of this Chapter we will explain the reason for large deformations showed by some of the Li adsorbed SiGeNTs.

One particular measurement that gives an idea of how strongly the Li atom binds to the system is the adsorption energy. In our calculations, the adsorption energy was calculated using the equation 4.1.

$$E_a = (E_{NT} + E_{Li}) - E_T, \tag{4.1}$$

where E_{NT} is the ground state energy of the SiGe (6,6) nanotube type x (x=I, II, III, or IV), and E_{Li} is the ground state energy of the Li atom. E_T is the ground state energy of the total system (nanotube + Li). According to equation 4.1, positive adsorption energy implies binding of the Li atom to the nanotube, and comparatively higher adsorption energy indicates preferential binding of one site over another site.

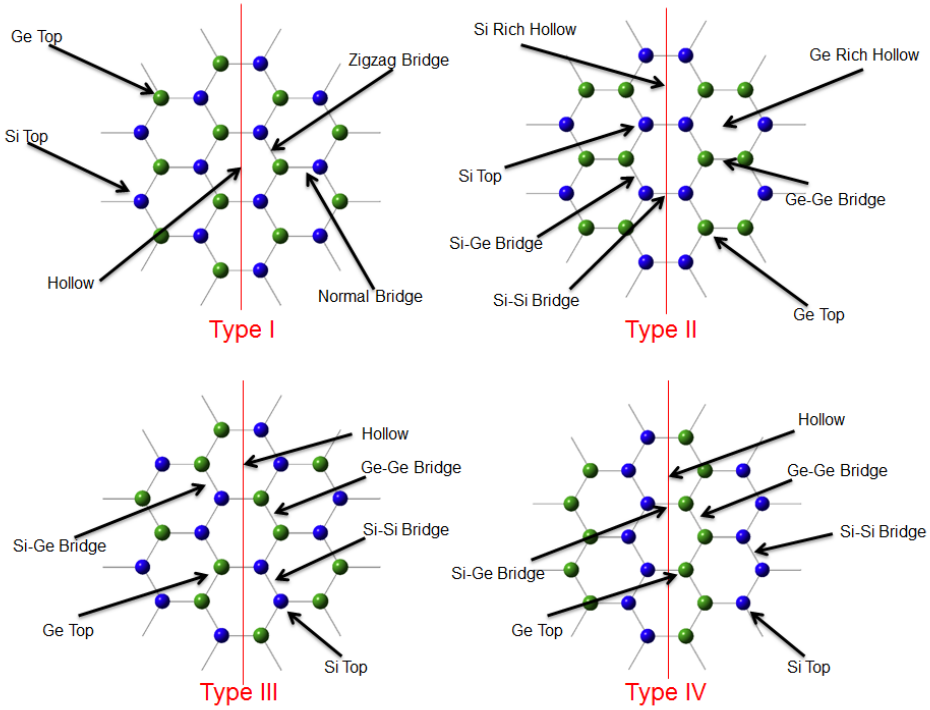

Figure 4.1: Local atomic arrangements of SiGe (6,6) four types of nanotubes with possible initial Li positions. Si atoms are in blue color, Ge atoms are in green color and the red lines indicate the direction of tube axis.

In Table 4.1, we present the results obtained for type I SiGe (6,6) NT and external Li atom interactions. We observed, regardless of the initial site, in type I SiGeNTs, Li always moves to an approximate Ge Top site. Since the final site was not precisely on a top site, we report the final position as “Quasi Ge Top”. We do note that the adsorption energies were slightly different from each other and this is expected since the quasi sites are not identical. All adsorption energies are positive, ranging in values from 1.607 eV to 1.639 eV. Since in Pauling scale, [108] the electronegativity of Ge is 2.05, that of Si is 1.90 and of Li is 0.96, when introduced, Li should donate its outermost electron to the SiGeNT and turn into a Li cation. In addition, both Si and Ge have the ability to attract the Li cation due to their high electronegativity. However, Ge should have higher probability to attract Li ion due to relatively high electronegativity compared to Si. Hence, Li-ion moves to on Ge Top site.

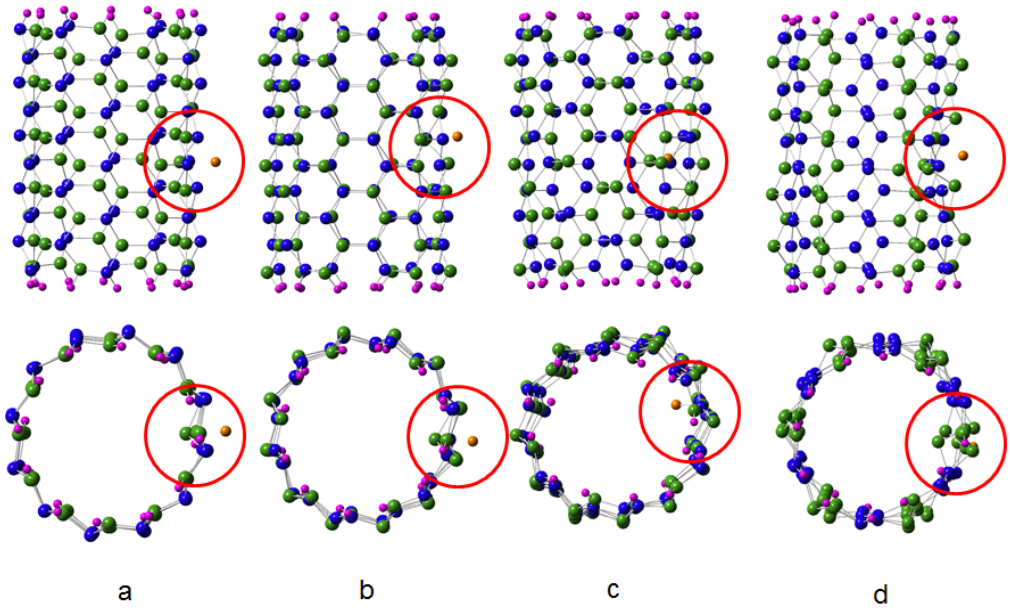

Figure 4.2: Optimized structure of Li + SiGe (6,6) side and top view, (a) type I NT (b) type III NT (external adsorption) (c) type III NT (internal adsorption) (d) type IV NT. Red circle: area where local bond stretching. Li atom is in orange color.

In Figure 4.2a, we show the optimized structure with side and top views of type I SiGeNT (6,6) + Li (external) adsorption. Initial bond lengths of the NT were around 2.34 Å. However, after addition of the Li atom, the nearest neighbor bond lengths around Li stretched to 2.42 Å. Nevertheless, the next nearest neighbor bond lengths were around 2.34 Å. Hence the bond elongation was highly localized. In order to facilitate such a local bond stretching, tubes have undergone a local deformation while optimization. This is clearly visible in the top view of the structure in Figure 4.2a where the out of boundary Ge atom inside the red circle indicate the local deformation.

Natural Bond Orbital (NBO) charge population analysis [97] showed that Li had lost almost one electronic charge for all cases where tubes retained the tubular shape (in type I adsorptions). Due to the tube's curvature, externally adsorbed Li interacts within a small area of the NT, to be exact, the four nearest neighbor atoms. Thus, the charge transferred by the Li should concentrate in that area. This is visible in Figure 4.3a and Figure 4.4, where Li had altered the symmetric nature of charge population and forced to concentrate around the adsorption site.

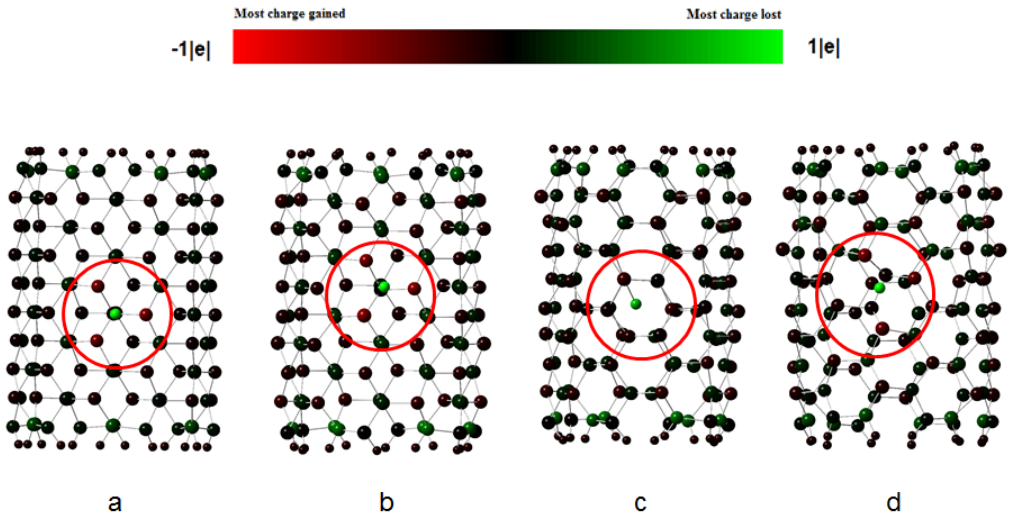

Figure 4.3: NBO charge distribution of SiGe (6,6) + Li, (a) type I (b) type III (external adsorption) (c) type III (internal adsorption) (d) type IV adsorptions. Li atom is positively charged and affected Si and Ge atoms are negatively charged.

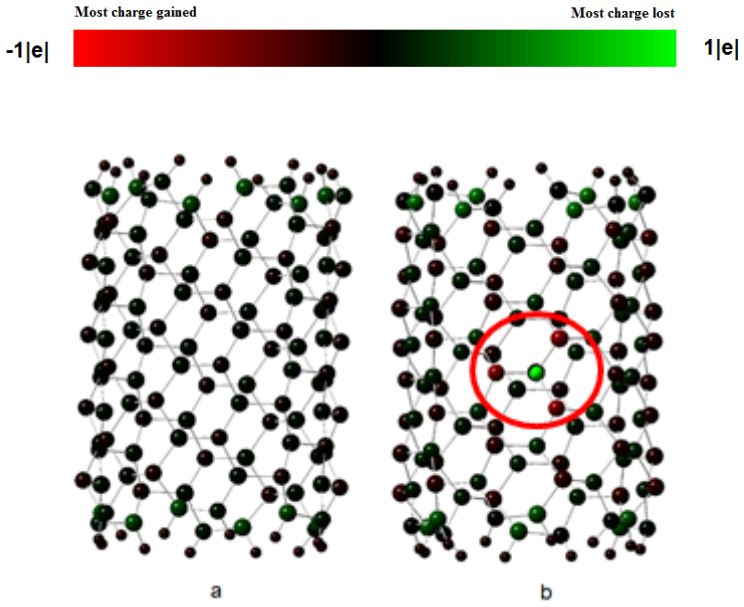

Figure 4.4: NBO charge distribution of (a) SiGe (6,6) and (b) SiGe (6,6) type I NT + Li. Charge distribution is localized to the vicinity of Li adsorption site. Li atom is positively charged and affected Si and Ge atoms gained negative charge.

Bond lengths of the nearest Si-Li and Ge-Li, happen to be in the range of 2.65Å-2.67Å (tabulated in Table 4.1). These values agreed well with the experimental values reported for Si-Li and Ge-Li by [109]. For type I, HOMO-LUMO gaps of the optimized structures were around 0.8 eV. Before Li adsorption, it was around 1.3 eV (on pristine SiGe (6,6) NTs). Figures 4.5a and 4.5d shows the LUMO of type I SiGeNT and HOMO of type I SiGeNT + Li (external), respectively. From those figures, it is clear that the delocalized electrons become localized after adsorption of the Li atom.

Li adsorption on external Hollow site of type I belongs to the second trend where the adsorption caused the tube to deform. In addition, internal adsorptions in type I SiGeNT also belong to this category. From our study, we are able to identify that in type I, total of 6 adsorptions (1-external and all 5 internal) resulted in deformed tubular structures. In type II, all 14 (7- external and 7- internal) adsorptions also resulted in severe tubular deformations. In type III, this happened in only one adsorption site (internal adsorption of Li on Si-Si Bridge). Finally in type IV, 9 sites (3- external and 6- internal) were severely deformed. In Figure 4.6, we have shown *some* such severely deformed structures representing each type. Later in this Chapter, we discuss the possible reasons behind these severe deformations.

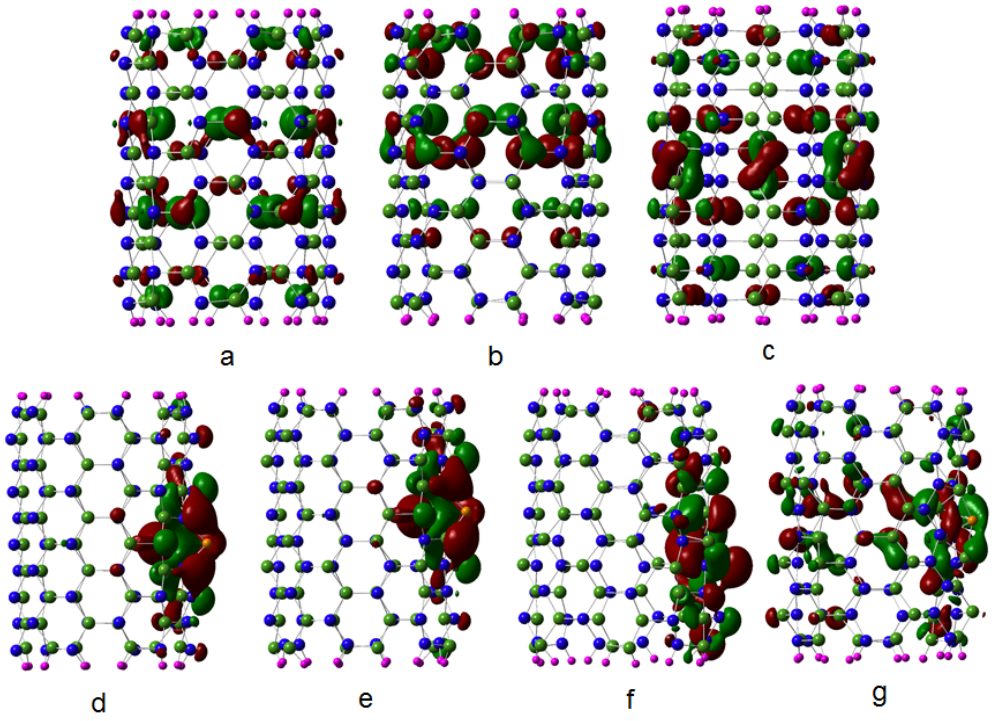

Figure 4.5: (a)-(c) LUMO of SiGe NT type I, type III and type IV. HOMO of SiGe NT + Li (d) type I, (e) type III external, (f) type III, internal and (g) type IV.

Table 4.1: External adsorption of single Li on type I SiGe (6,6) NT.

Initial position	Adsorption energy (eV)	Band gap (eV)	NBO Charge (lost by Li) |e|	Bond length (From Li to closes Si and Ge) (Å)	Final position
Ge Top	1.637	0.822	0.907	Ge-Li 2.669 Si-Li 2.654	Quasi Ge Top
Si Top	1.607	0.854	0.904	Ge-Li 2.662 Si-Li 2.669	Quasi Ge Top
Normal Bridge	1.638	0.835	0.905	Ge-Li 2.669 Si-Li 2.663	Quasi Ge Top
Zigzag Bridge	1.639	0.834	0.905	Ge-Li 2.662 Si-Li 2.669	Quasi Ge Top
Hollow			Deformed		

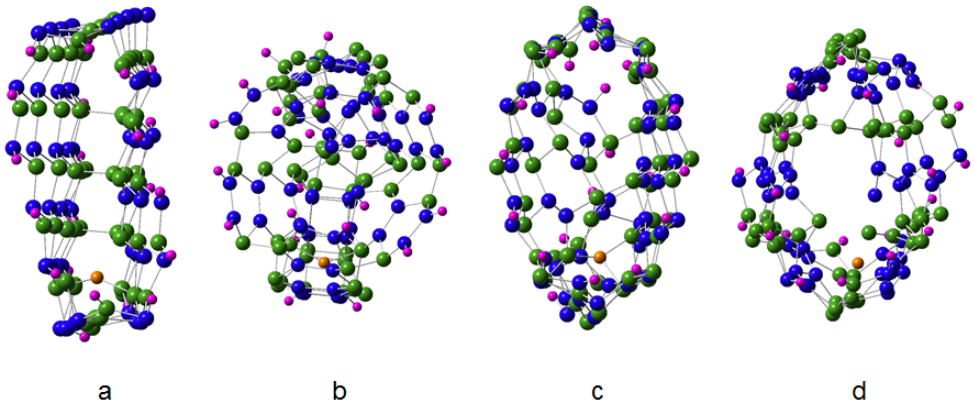

Figure 4.6: Top view of deformed structures of Li + SiGe (6,6) NTs (a) type I internal (b) type II external (c) type III internal (d) type IV internal.

When considering Li adsorption on type III SiGe NTs, there were 12 possible adsorption sites (counting both internal and external sites), and in 11 sites, the tubular shape was maintained after optimization. Tables 4.2 and 4.3 show the results obtained by the external and internal adsorptions of Li in type III SiGeNT of size (6,6), respectively. There is one major difference between the results of type I and type III external adsorptions. As in type I, type III final adsorption sites did not end in one site. Initial Hollow, Si-Si Bridge and Si Top adsorptions ended in Quasi Hollow, Quasi Si Top, and Quasi Si Top sites, respectively. In addition, any Li adsorption started with a higher density of Ge atoms in the vicinity of the adsorption site, adsorbed into a Quasi Ge Top site. These different finishing sites should be expected in type III, since initial adsorption sites of type III does not have equal numbers of Ge or Si atoms as in the case of type I. In some cases, Si dominates the nearest neighbor environment, and in some cases, Ge dominates the nearest neighbor environment. Therefore, in type III, the final site which Li atom moves in always depends on the initial placement site.

Table 4.2: External adsorption of single Li on type III SiGe (6,6) NT.

Initial position	Adsorption energy (eV)	Band Gap (eV)	NBO Charge (lost by Li) |e|	Bond length (Å)	Final position
Hollow	1.453	0.685	0.698	Ge-Li 2.586 Si-Li 2.598	Quasi Hollow
Si–Si Bridge	1.625	0.918	0.684	Ge-Li 2.652 Si-Li 2.678	Quasi Si Top
Si–Ge Bridge	1.615	0.857	0.910	Ge-Li 2.645 Si-Li 2.650	Quasi Ge Top
Ge–Ge Bridge	1.615	0.857	0.910	Ge-Li 2.645 Si-Li 2.650	Quasi Ge Top
Si Top	1.632	0.930	0.683	Ge-Li 2.652 Si-Li 2.678	Quasi Si Top
Ge Top	1.615	0.857	0.910	Ge-Li 2.645 Si-Li 2.650	Quasi Ge Top

Table 4.3: Internal adsorption of single Li on type III SiGe (6,6) NT.

Initial position	Adsorption energy (eV)	Band gap (eV)	NBO Charge on Li |e|	Bond length(Å)	Final position
Hollow	1.657	0.746	0.612	Ge-Li2.780 Si-Li 2.583	Quasi Hollow
Si–Si Bridge			Deformed		
Si–Ge Bridge	1.610	0.775	0.655	Ge-Li 2.583 Si-Li 2.795	Quasi Hollow
Ge–Ge Bridge	1.611	0.774	0.655	Ge-Li 2.583 Si-Li 2.797	Quasi Hollow
Si Top	1.655	0.748	0.612	Ge-Li 2.780 Si-Li 2.584	Quasi Hollow
Ge Top	1.606	0.775	0.655	Ge-Li 2.583 Si-Li 2.795	Quasi Hollow

From the external adsorption results of type III SiGeNTs, we conclude that the most probable site for Li to reside was Quasi Ge Top site with adsorption energy of 1.615 eV. However, adsorption energies for different sites indicated that the most stable site for external Li adsorption in type III was quasi on Si Top with adsorption energy of 1.632 eV. Unlike the external Hollow site of type I, type III Hollow site adsorption did not produce a deformation of the nanotube. However, the Hollow site was the least stable site out of possible external sites of type III, and the adsorption energy was 1.453 eV. Again, we observed the stretching of bond lengths between the nearest neighbor atoms of Li. Ge-Ge bond length had stretched from 2.39 Å to 2.51 Å, and Si-Ge bond length had stretched from 2.34 Å to 2.39 Å and finally Si-Si bond length had stretched from 2.27 Å to 2.33 Å. Again, this stretching was not observed for the next nearest neighbor atoms, where bond lengths remained at the values of bare SiGeNTs. Figure 4.2b shows the external adsorption of Li on type III SiGeNT (6,6). According to Figures 4.2a and 4.2b, it is clear that the final structures are similar in type I and type III. However, the NBO population analysis predicted that charges on Li in type III (tabulated in Table 4.2) was not as steady as in type I external adsorption. Whenever Li adsorption ended in Quasi Ge Top site, NBO charge on Li was close to 1|e|. For all other sites, Li showed a NBO charge of around 0.6|e|. We believe that this is due to the influence of high electronegativity of Ge. When on top of

the Ge site, large amount of charge transfer occurred from Li to the NT to form a strong Li cation.

Type III internal adsorptions are energetically more favorable compared to external adsorption. Unlike external adsorptions, internal adsorptions preferred to reside on the Hollow site. We believe that this is a consequence of NT curvature. In general, the atoms are in sp^2 hybridization for all NTs with the hexagonal lattice structure. In the case of SiGeNTs, the situation was similar. Si and Ge atoms were in sp^2 hybridization, and they have conjugated p orbitals perpendicular to tube surface. Due to curvature of the NTs, external parts of these p orbitals were apart, and internal parts of these p orbitals were close. Hence, the internal overlaps of these p orbitals were much stronger than external overlap (refer Figure 4.7). This quasi overlapping of p orbitals caused Si and Ge atoms to act as individual electrophile centers in externally. Therefore, in external adsorptions, we expected and observe that Li moved to on top of an atom center. Since internal overlapping was stronger, p orbitals created an electrophilic rings under the hexagonal rings. Hence, when introduced, Li observed the attraction equally in every direction and moved to a Hollow site to minimize the attraction from every direction.

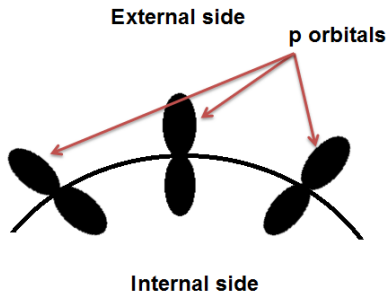

Figure 4.7: Quasi overlapping of p orbitals. Because of the curvature of NT, externally the pi bonds are apart and internally the pi bonds are close.

In Table 4.4, we report the results obtained for type IV SiGeNT and external Li adsorptions. In type IV, the tubular structure was retained for only the adsorption sites with a higher number of Ge atoms in the vicinity of the adsorption site. In addition, we did not observe any bond stretching. Possible reason might have been the absence of the local deformation. It is also visible from the Figure 4.2d, where larger area was deformed compared to other types. In addition, adsorption energies were considerably lower in value compared to other types. The lower adsorption energies of type IV tube indicate the inability to adsorb Li atoms as in other types of SiGeNTs. HOMO-LUMO gaps of type IV structures do not show significant change as in other types. However, NBO population analysis showed that Li transferred part of its charge.

Based on the structures, which retained the tubular shape, we can identify several factors. In all pristine SiGeNTs, LUMOs were highly delocalized and Figures 4.5a-c shows this clearly. When Li adsorbed, those delocalized nature became localized. This is visible in the HOMO plots of SiGeNT + Li (refer Figure 4.5d-g). We note that the localization was not pronounced in type IV compared to types I and III. In addition, the charge accumulation was higher in those effected regions of type I and III compared to type IV. The spread out nature of charge population in type IV SiGeNTs implies that for a given length, the number of Li atoms that can be adsorbed is lower than the numbers in types I and III.

At the start of our calculation, we assumed that the B3LYP functional was well suited to model these semiconducting structures correctly. In order to understand whether there was any functional dependence to the severe deformations of *some* nanostructures, we carried out another calculation of SiGe type I (6,6) NT with internal adsorption of Li with the PBE0 functional [110]. However, the result was same, and the structure ended in a severely deformed form. Another assumption we made was to use size (6,6) NTs instead of a larger diameter tube. Therefore we checked the internal adsorption of Li atom on type I size (8,8) and (10,10) SiGeNTs, and those structures also ended in a severely deformed form as shown in Figure 4.8.

All these observations confirmed that the deformations observed were not due to the size of the tube chosen to study or the functional used. In addition, we carried out another calculation on internal adsorption of SiGe hemisphere capped type I (6,6) NT. The purpose was to find whether the capping would remove the deformation as observed in SiNTs by Song et al. (2010). First, we capped the type I SiGeNT (6,6) with a SiGe hemisphere and optimized the structure. Later on, Li was added internally to the capped NT and re-optimized the structure. It turned out that the result was same and the structure was deformed (refer Figure 4.9).

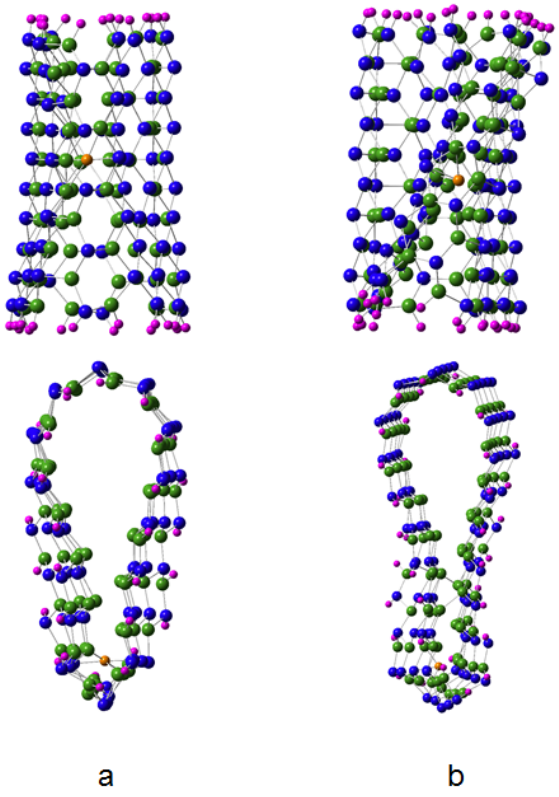

Figure 4.8: (a) Side and top views of SiGe type I (8,8) NT + internal Li adsorption. (b) Side and top views of SiGe type I (10,10) NT + internal Li adsorption.

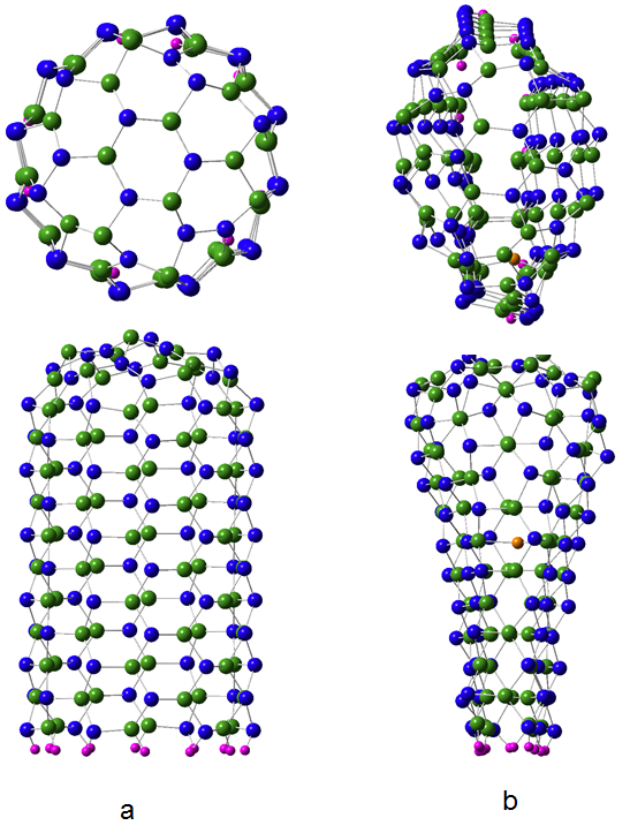

Figure 4.9: Top and side views of semi-capped SiGe type I (6,6) NT (a) before Li adsorption (b) after Li adsorption.

Considering all four types and their different initial adsorption sites, we have 48 input structures. From those 48 structures, only 18 were able to retain the tubular shape after Li adsorption. In type I, 60% of input geometries ended in severe deformation. In type II, deformation was 100% and in type III, it was less than 10%. In type IV, the deformation went up to 75%. These deformations were indeed a problem for the SiGeNTs to be used as anode material. It is vital to keep the tubular shape to ensure the prompt release of Li ions and fast kinetics associate with the anode materials. Hence understanding the reason behind these severe deformations was critical.

In literature, there are some reports of similar observations with Li adsorption on polyacenes [111]. Upon adsorption of one Li atom, polyacenes structure, which was under consideration had bended around the adsorbed Li atom. They had reported that the reason for bending might have been the Jahn-Teller effect [112]. According to the Jahn-Teller effect, a nonlinear molecule cannot have both orbital electronic degeneracy and stability of the nuclear configuration simultaneously. Whenever orbital degeneracy occurs, it forces the nuclear configuration to rearrange (by reducing the symmetry to a lower level) in order to lift the orbital degeneracy. The distortion from orbitals degenerating deeper levels from the Fermi level are small. In addition, in their work, Szakacs *et al.* [113] predicted that ionized and excited CNT might have Jahn-Teller active orbitals and could cause distortions in tube shape. According to their study, CNTs

in neutral form or ground state do have degenerate orbitals near Fermi level. Since those orbitals in either fully filled or completely empty state, they were in Jahn-Teller inactive mode. However, excitation or ionization of these tubes could lead electrons to fill those degenerate orbitals partially. In such a situation, those orbitals become Jahn-Teller active and eventually nuclear positions had rearranged to lift the orbital degeneracy. Transition from higher symmetry to lower symmetry results in deformed tubular shape. This is also true for the anions. Koga *et al.* [114] and Tanaka *et al.* [115], in their works on C_{60} and C_{60} anions, predicted that the LUMO of C_{60} had three-fold degeneracy. When C_{60} anions were made ($(C_{60})^{-1}$- $(C_{60})^{-5}$), LUMOs converted into partially filled states and ended up having Jahn-Teller active orbitals near the Fermi level. Therefore, the rearranged structure had distorted the bucky-ball shape into a squashed shape. In fact, they have found that due to Jahn-Teller effect, high symmetry I_h configuration distorted into low symmetry D_{5d}, D_{3d} or D_{2h} structures.

The present works of SiGeNT + Li systems also have similar relation to work of C_{60} anions. SiGeNTs were in neutral and ground state form before the adsorption of the Li. The introduction of a Li atom into SiGeNTs made SiGe anionic NTs. If SiGe anionic NTs have Jahn-Teller active orbitals it could distort the tubular shape. Based on the success rate of different types keeping the tubular shape, we can deduce the order of LUMO degeneracy of bare SiGeNTs to be as follows;

type II > type IV > type I > type III,

where type II has the highest degeneracy and type III, the lowest degeneracy.

Figure 4.10 shows the frontier orbitals (first five HOMOs and LUMOs) of SiGe (6,6) pristine NTs. In all four types, there exist at least one pair of degenerate HOMOs, and they were doubly occupied and fully filled with electrons. Therefore they were in Jahn-Teller inactive state. This explains our observations of not having any distortions in bare SiGeNTs. As expected, LUMO and LUMO+1 orbitals of type II were highly degenerate. In addition, LUMO+2 and LUMO+3 orbitals of type II were degenerate (refer Figure 4.10b). In type I, degeneracy of LUMO and LUMO+1 orbitals were lower than type II, and their LUMO+2 and LUMO+3 orbitals were degenerate (refer Figure 4.10a). In type III, degeneracy occurred at LUMO+2 and LUMO+3 orbitals (refer Figure 4.10c) and not in LUMO and LUMO+1 orbitals. In type IV, even though the LUMO was not degenerate, LUMO+1 and LUMO+2 orbitals were highly degenerate. From the orbital energy diagram of pristine SiGeNTs (refer Figure 10), it is clear that type II shows the highest effective degeneracy, and type III shows the lowest effective degeneracy. Therefore, we expect to have highest and lowest number of distorted tubular structures from types II and III, respectively. This reasoning agrees well with our results.

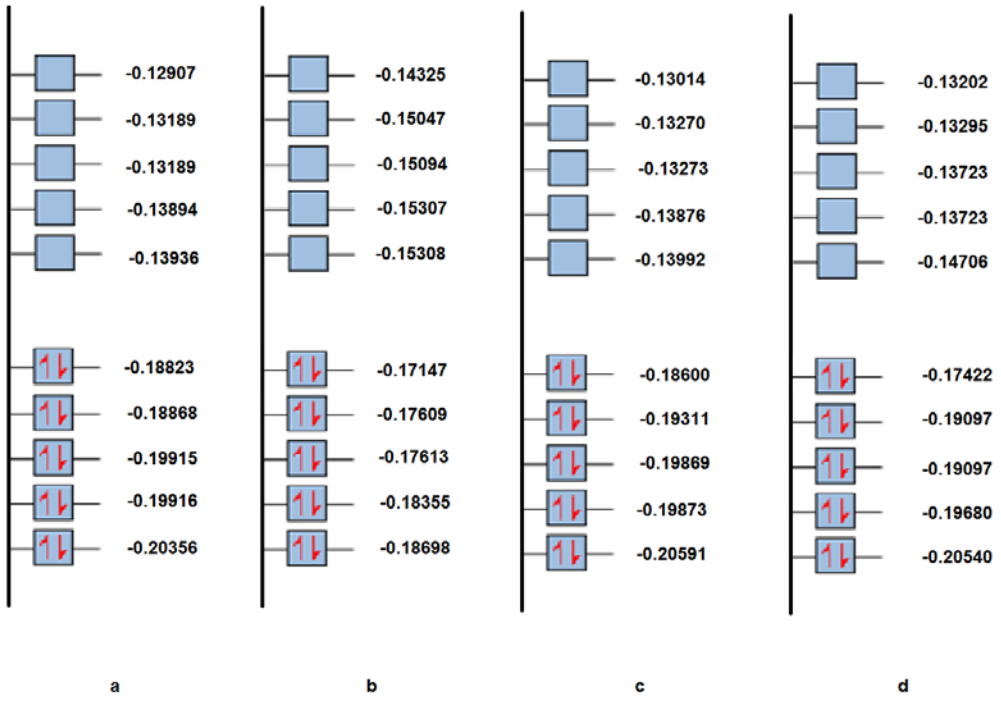

Figure 4.10: Illustrative molecular orbitals near frontier orbitals (first five LUMOs and HOMOs), (a) type I (b) type II (c) type III (d) type IV. (Energies in hartree and not drawn according to scale).

It is also worth checking the orbital energies of the structures that retain the tubular shape. In practical conditions, it is desirable to add more than one Li if these tubes are to be used as anode materials. Therefore, the default question is whether these tubes survive in high Li concentration. In Figure 4.11, we illustrated the frontier molecular orbitals of the structures representing each category that retained the tubular shape. From that figure, it is clear that orbital degeneracy has been lifted from the orbitals near the Fermi level. Therefore, we do not have any Jahn-Teller active orbitals, and hence there would be no further distortions. This implies that, these tubes can survive in high Li concentrations.

In addition we performed Li interaction with much longer (~37 Å) SiGe nanotubes. With the increase of length, we found that the degenerating orbitals presented around Fermi level in earlier short pristine SiGeNTs have vanished. This degenerating orbital disappearance with the increment of tube length had also observed in CNTs by Szakacs *et al.*[113]. Hence as expected, adsorption of one Li did not change the tubular structure. However the adsorption energy has decreased by 0.02 eV with respect to the shorter length tubes. In addition longer tubes showed much reluctance towards the deformation. We can conclude that having SiGeNTs with longer lengths will be very successful in performing as Li ion anode material.

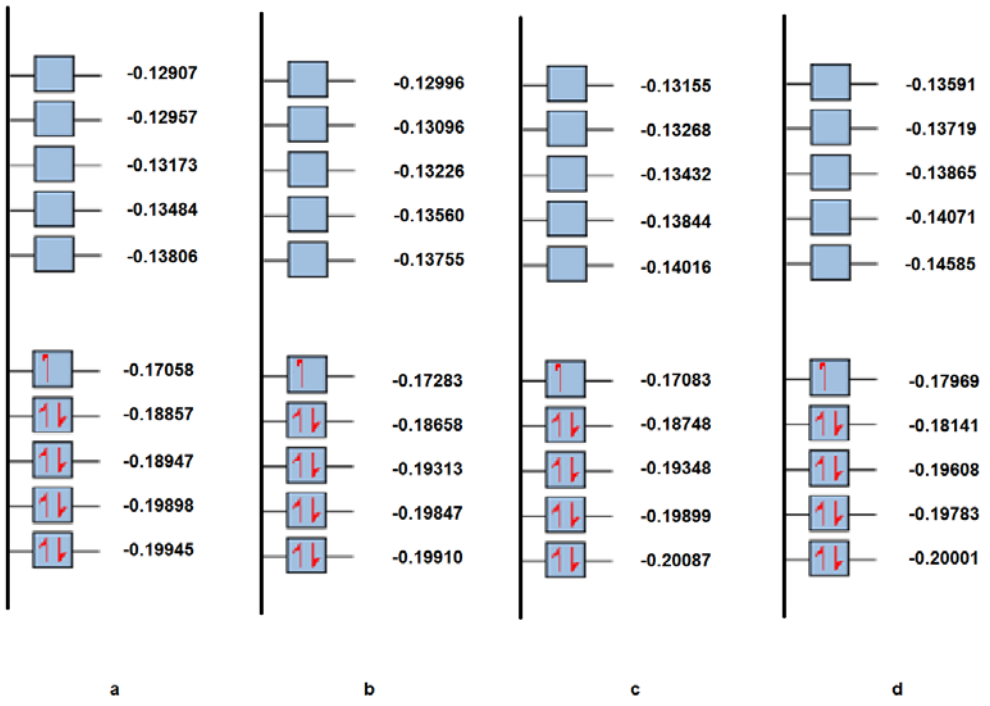

Figure 4.11: Illustrative molecular orbitals near frontier orbitals (first five LUMOs and HOMOs), (a) type I + external Li (b) type III + external Li (c) type III + internal Li (d) type IV + external Li. (Energies in hartree).

Chapter 5

Influence of H, H_2, O and O_2 on Armchair SiGe Nanotubes

5.1 Introduction

As mentioned earlier SiGeNTs have the characteristic puckered surface nature. In addition, it is also reported that SiGe NTs are semiconducting in nature irrespective of their chirality, and spread in wide range of band gap energies [116]. This is an added advantage in fundamental electronic devices as metal oxide semiconductor field effect transistors (MOSFETs) and field effect transistors (FETs) since no need for the selection of NTs based on their chirality[87,116,117]. However the stability of the NT in terms of geometry and the semiconducting nature might effect from most common impurities like oxygen (O) and hydrogen (H) [117-122]. O is highly reactive with Si and it benefits in creating MOSFET devices. Alternatively Ge oxides are undesired in MOSFETs owing to its poor electrical properties[29]. Also H is known to stabilize the surfaces of reactive materials[120-122]. In these SiGeNTs the coordination number of Si and Ge are 3, which is one less in their desired sp^3 coordination number of 4. Due to H attachment, the tube wall can be stabilized by raising the coordination number to 4. In addition H is known to increase the band gaps when the respective materials introduced to H rich environments by creating the hydrogenation[121,122]. However it is also reported that with controlled

exposure, O and H can be attached as point defects and O in particular could result in decreasing the band gaps even making SiNT metallic[119].

SiGeNTs immerging as potential material for next generation nanodevices, it is highly important to identify the influence of most common impurities like H and O on SiGeNTs. In this work we report our results on interaction of SiGe and X (X= H, O, H_2, O_2). In this Chapter we will specifically focus on HOMO-LUMO gaps, the adsorption energies and trends, the changes and trends in geometric structures of SiGeNTs.

5.2 Results and discussion

In this work, we have used the hybrid functional, B3LYP [73,75], and the all electron 3-21G* basis set [95] as implemented in the GAUSSIAN 09 suite of programs [48]. All structures reported here are geometry as well as spin optimized with the energy convergence criterion set at 10^{-6} a.u.

Since large diameter NT increases the computational demand significantly with an all-electron basis set, we have used the SiGe (6,6) NT (which contains total of 144 atoms with stoichiometry of $Si_{60}Ge_{60}H_{24}$, where H atoms are used to terminate the NT) to mimic the SiGeNTs for the calculations reported in this work. In addition, as mentioned in Chapter 4 which is the study of interaction of

SiGeNTs with Li [123] yielded that there is a possibility for tube wall to be collapsed with a smaller length (~20Å). However with a longer length (~35Å and higher), wall collapsing is suppressed. Since computational cost to model a long SiGeNT is highly demanding, we decided to focus our adsorptions on shorter length (~20Å) and more prudent SiGeNT type (type III) [123]. It is note here that by focusing only on type III SiGe (6,6) NT [116], we will not lose any additional chemical or physical properties.

The E_a adsorption energy for each system was computed using the following equations. For the atomic adsorption

$$E_a = E_{SiGeNT} + E_X - E_{SiGeNT+X}, \quad (5.1)$$

and if the molecule does not dissociate

$$E_a = E_{SiGeNT} + E_{X_2} - E_{SiGeNT+X_2}, \quad (5.2)$$

or, if the molecule dissociates

$$E_a = [E_{SiGeNT} + 2E_X - E_{SiGeNT+2X}]/2, \quad (5.3)$$

where E_{SiGeNT} is the ground state total energy of the pristine SiGeNT, E_{x_2} and E_X are the ground state energies of the X(=H,O) molecule and atom, respectively. $E_{SiGeNT+X_2}$ and $E_{SiGeNT+X}$ are the ground state total energies of the clusters incorporating SiGeNT and the adsorbed molecule and atom, respectively. All nanotubes are hydrogen terminated at the ends to saturate the dangling bonds and to simulate the “infinite” nature of the nanotubes.

5.2.1 H atomic adsorption

The adsorption of atomic H or O, initiates with different adsorption sites due to distinct Si and Ge atomic arrangement in type III SiGeNT. Figure 5.1b present those initial H and O placement sites. These adsorption sites are common to both external and internal adsorptions. Each site of “Ge top”, “Si top” and “Si-Ge Bridge” has additional adsorption sites due to puckered nature of the tube wall. We present H external and internal adsorption results on Tables 5.1 and 5.2. One important observation is that after optimization, except for the external “Ge-Ge Bridge” site, H has always moved to either “Si top” or “Ge top” site. In addition, the “Si top” site seems to be the most preferred and stable site since in either external or internal adsorption, the “Si top” energy is higher than “Ge top” adsorption energy (refer Table 5.1 and Table 5.2). Internally adsorbed H, which is at the inside “Si top” site, interact with more Si and Ge atoms compared to externally adsorbed H due to the curvature of nanotube, and hence the internal adsorption energies are higher compared to external adsorption energies.

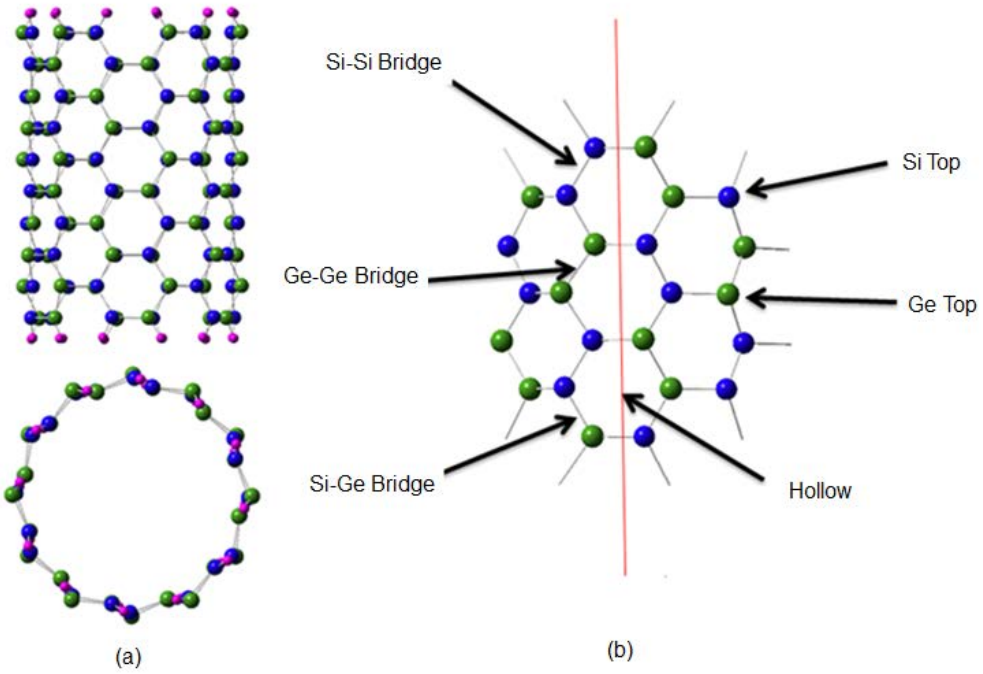

Figure 5.1: (a) Type III, SiGe (6,6)NT side and top view. Si atoms in blue color, Ge atoms in green color, and H atoms in pink color respectively. (b) Initial placement positions for adatom.

Table 5.1: H atom external adsorptions.

Position		D_{Si-H} or D_{Ge-H}	E_a[c]	HOMO-LUMO
Initial site	Final site[a]	(Å)	(eV)	gap (eV)
Ge top	Ge top	1.57	1.89	0.81
Ge top - 2nd	Ge top	1.57	1.99	0.54
Si top	Si top	1.50	2.07	0.58
Si top - 2nd	Si top	1.49	2.29	0.81
Si-Ge bridge	Si top	1.50	2.07	0.58
Si-Ge bridge - 2nd	Si top	1.49	2.29	0.81
hollow	Si top	1.49	2.29	0.81
Si-Si bridge	Si top	1.49	2.29	0.81
Ge-Ge bridge	Ge-Ge bridge	1.66	1.29	0.82

[a]Final site is the H atom location after optimization. [b]D_{Si-H} or D_{Ge-H} is the distance from H atom to attached Si or Ge atom. [c]E_a is the adsorption energy.

Table 5.2: H atom internal adsorptions.

Position				
Initial site	Final site[a]	D_{Si-H} or D_{Ge-I} (Å)	E_a[c] (eV)	HOMO-LUMO gap (eV)
Ge top	Si top	1.50	2.28	0.63
Ge top - 2nd	Ge top	1.58	2.01	0.58
Si top	Si top	1.50	2.29	0.64
Si top - 2nd	Si top	1.50	2.16	0.75
Si-Ge bridge	Si top	1.50	2.28	0.63
Si-Ge bridge - 2nd	Ge top	1.58	2.06	0.65
hollow	Ge top	1.58	2.01	0.58
Si-Si bridge	Si top	1.50	2.29	0.64
Ge-Ge bridge	Ge top	1.58	2.01	0.57

[a]Final site is the H atom location after optimization. [b]D_{Si-H} or D_{Ge-H} is the distance from H atom to attached Si or Ge atom. [c]E_a is the adsorption energy.

The pristine SiGeNT has sp^2 or sp^3 hybridization for the Si and Ge atoms. When in sp^3 hybridization the Si and Ge atoms are under coordinated. We observe that when H introduced, the Si or Ge atom which H attached becomes fully coordinated. Furthermore the bond distances of Si-H and Ge-H are typical bond lengths reported in literature[31]. In addition the single adsorption which ended in "Ge-Ge bridge" site (refer Table 5.1) has the highest length from the tube wall with a relatively low adsorption energy compared to other sites. This indicates that the "Ge-Ge Bridge" site is less favored and less stable.

In pristine SiGe (6,6) NT, the energy difference of HOMO energy and the LUMO energy is ~1.27 eV. After adsorption of H atom, the HOMO-LUMO energy gap of the system in general decreased and the values in the energy range of 0.54-0.82 eV (refer Tables 5.1 and 5.2). Since optimizations of SiGe (6,6) NT + H atom revealed that H atom prefers to move onto "Si top" or "Ge top" sites, we plotted the density of states (DOS) only for those two sites (refer Figure 5.2). It indicates that the overall DOS remains similar to the pristine SiGeNT. However there is additional defect density appearing around the frontier orbital region and it is due to this defect that the HOMO-LUMO gap decrease.

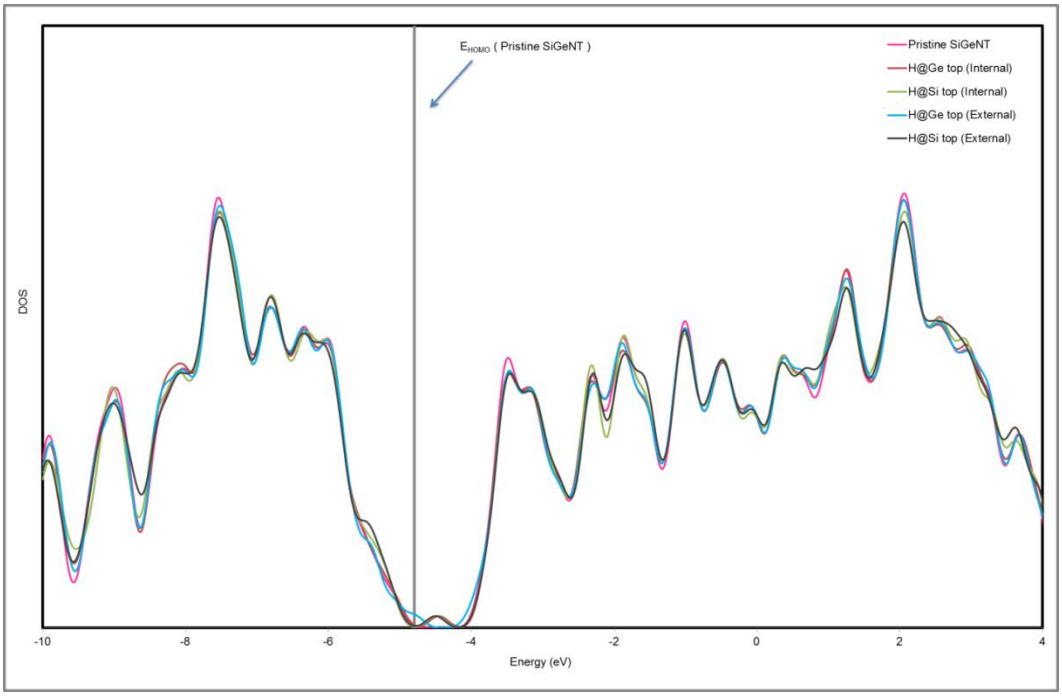

Figure 5.2: DOS of the pristine SiGeNT and the internal and external adsorptions of H on Si top and Ge top sites. Vertical line is the reference line for HOMO energy of pristine SiGeNT.

It is interesting to know the change on DOS as the nanotube exposed to more H. Therefore we have carried out a calculation of SiGe (6,6) NT + 24 H system with all the H directly attached onto either “Ge top” site or “Si top” sites internally and externally. The 24 H is selected due to the fact that it is the number of H needed to saturate two middle layers of the SiGe (6,6) NT. The optimized structure for SiGe (6,6) NT + 24 H system is presented in Figure 5.3. By comparing the DOS plot of this SiGe (6,6) NT + 24 H system (in Figure 5.4) along with the DOS of pristine SiGe (6,6) NT one could clearly identify that the addition of large number of H cause the increases of HOMO-LUMO energy gap (in fact the value changed from 1.27 eV to 1.61 eV). Because of the adsorbed H atoms, Si or Ge atoms which they attached becomes fully coordinated sp^3 hybridized atoms. Those Si and Ge atoms create more localized orbitals which resulted in increasing the HOMO-LUMO energy gap. According to Mulliken population analysis (MPA) scheme, the charge transfer between the H atom and the SiGe (6,6) NT is very low. Charges of the H atom vary between a loss of 0.072 and a gain of 0.027, in units of electron charge (|e|). This indicates that Si and Ge making covalent nature bonds rather than ionic bonds with H atoms.

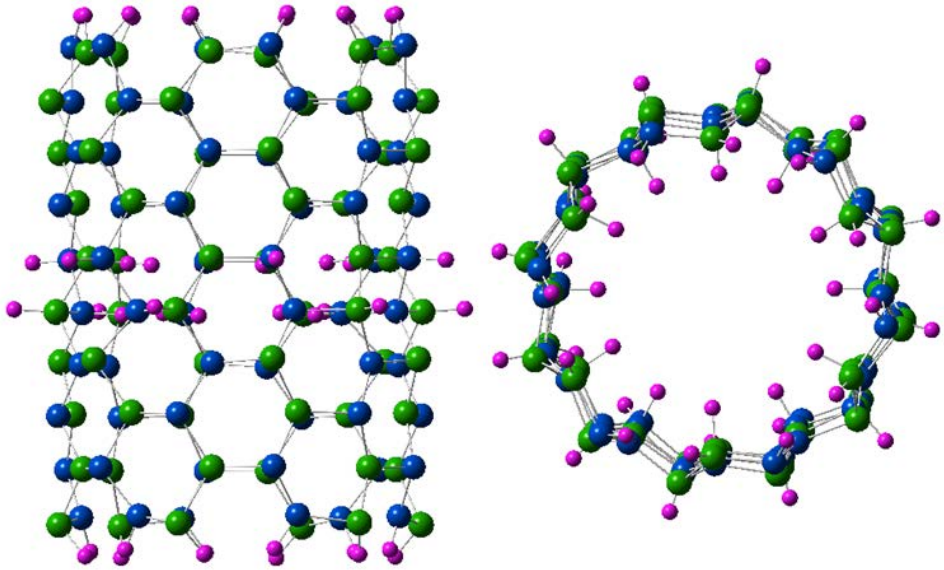

Figure 5.3: Side and top view of optimized SiGeNT + 24 H system. Atoms are in usual colors and only the middle layer is saturated with H in order to identify the effect of H rich interaction with SiGeNTs.

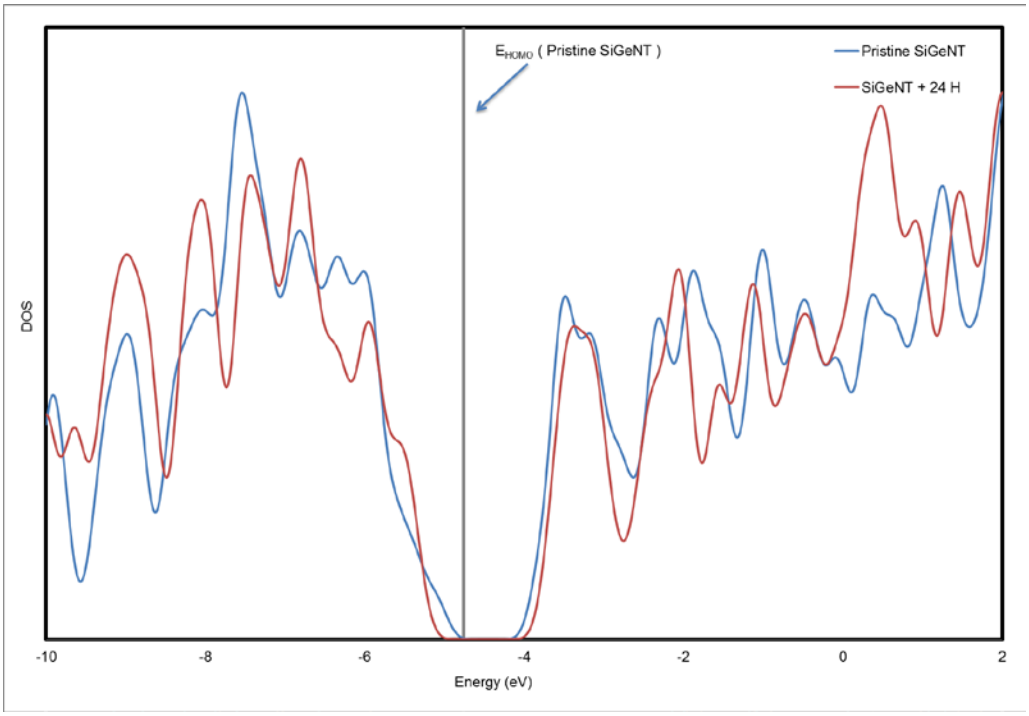

Figure 5.4: DOS of the pristine SiGeNT and SiGeNT + 24 H system. The vertical line is the reference line for HOMO energy of pristine SiGeNT.

5.2.2 O atomic adsorption

Initial adsorption sites of O atom are same as H adsorption. However unlike H, O is much more electronegative compared to Si and Ge. Therefore, charge transfer happened from the NT to O atom. Furthermore, O atom tend attack the tube wall and break the constitute bonds of SiGeNT. Therefore we observed that O can attach as an adatom making bonds with nearby Si and Ge atoms or incorporate into Si-Si, Si-Ge or Ge-Ge bonds making Si-O-Si, Si-O-Ge or Ge-O-Ge bonds. We have listed the O attachments on the SiGeNT in Figure 5.5. For the clarity we only present the local area around the adsorption sites.

In Tables 5.3 and 5.4, we present the O external and internal adsorption results. The main difference in O adsorption compared to H adsorption is that there is no “Ge top” or “Si top” site as final site. In addition the adsorption energy is much higher in O adsorptions than H adsorption. There is no adsorption energy increment when moving from external to internal sites. This is different from H adsorption where we observed the increase in adsorption energy moving from external to internal. The reason for this difference is that in H adsorption, the internal or external adsorption can be identified after adsorption. However in O adsorption, once the bond was broken and O atom incorporated into the tube wall, there was no geometrical trace of whether it was an internal or external adsorption. Hence the adsorption energy should not change in O adsorption when moving from external to internal.

Also we have noticed that the external adsorptions of O tend to incorporate into the NT wall by breaking the bonds while internal adsorptions tend to attached to both Si and Ge atoms in order to incorporate into wall. Also breaking the Si-Si bond and attaching into the wall is energetically more favored in both internal and external adsorptions. Unlike the H adsorption we notice large amount of charge transfer with O adsorption and O had gained a charge ~0.5|e| in general. Which indicate O attached by making ionic nature bonds.

We note that O adsorption with “Broke Si-Si bond” have the highest charge transfer where it is a gain of ~0.6|e| which indicates even stronger ionic bond. This is also reflected in relatively higher adsorption energies recorded in “Broke Si-Si bond” O adsorptions (refer Tables 5.3 and 5.4). Strong charge transfer with Si is resulted in due to the fact that Si is less electronegative compared to Ge. Hence Si loses charge easily compared to Ge, when interacting with a high electronegative element like O. In addition, the “Broke Ge-Ge bond” is the least stable, which agrees well with the above mentioned reasoning where Ge makes relatively weak ionic bonds with O and hence resulted in lower adsorption energy. These observations are also agree well with the experimental results of forming strong SiO_2 and forming weak GeO_2 on SiGe thin films and bulk materials [29].

HOMO-LUMO energy gap did not decreased significantly as in H adsorptions which indicates O adsorptions does not generate any defect density state around Fermi energy region. In Figure 5.6 we present the DOS of O adsorptions. We observe that for O adsorptions there was no generation of any defect density as in H adsorptions. However, compared to pristine SiGeNT, very minimal HOMO-LUMO energy gap decrement can be observed on DOS (refer Figure 5.6).

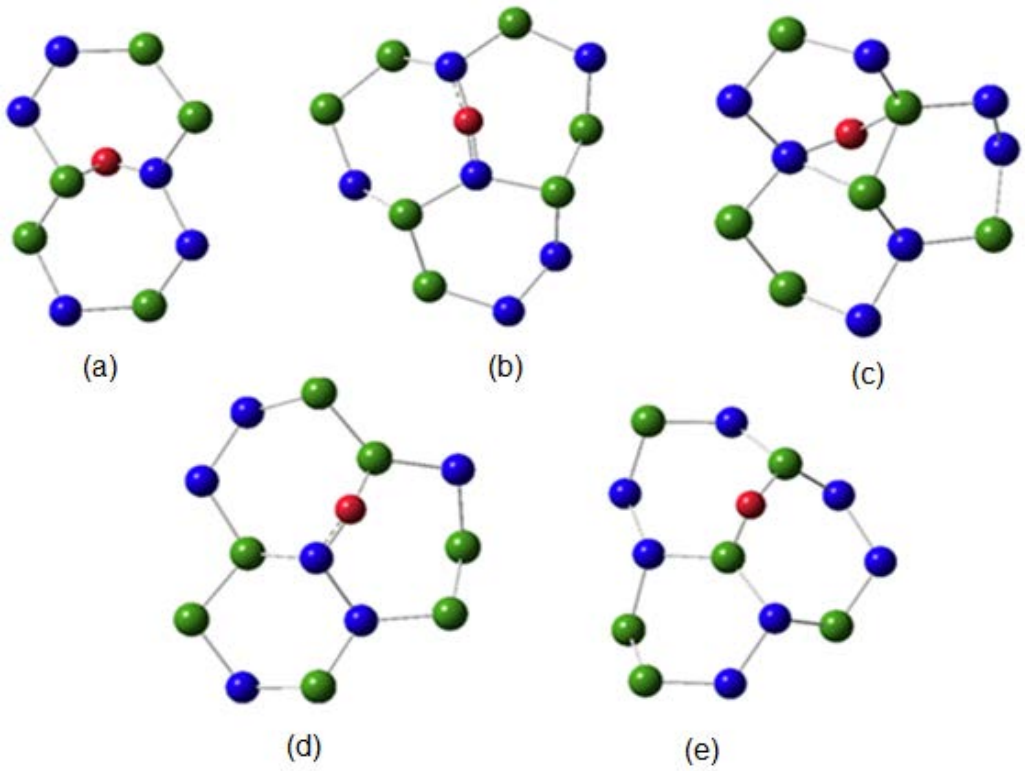

Figure 5.5: Different O attachments in SiGeNT. (a) Attached into both Si and Ge (b) broke the Si-Si bond (c) skipped the middle atom (d) broke the Si-Ge bond (e) broke the Ge-Ge bond. Si and Ge atoms are in usual colors while O is in red color.

Table 5.3: O atom external adsorptions.

Position				
Initial site	Final site[a]	E_a[b] (eV)	HOMO-LUMO gap (eV)	Mulliken charge gained by O atom |e|
Ge top	Broke Ge-Ge bond	4.48	1.24	0.46
Ge top - 2nd	Attached to both Si and Ge	5.52	1.22	0.46
Si top	Broke Si-Si bond	6.10	1.18	0.59
Si top - 2nd	Attached to both Si and Ge	5.52	1.22	0.46
Si-Ge bridge	Attached to both Si and Ge	5.50	1.25	0.50
Si-Ge bridge - 2nd	Broke Si-Ge bond	5.36	1.21	0.55
Hollow	Broke Si-Ge bond	5.36	1.21	0.55
Si-Si bridge	Broke Si-Si bond	6.10	1.18	0.59
Ge-Ge bridge	Broke Ge-Ge bond	4.48	1.24	0.46

[a]Final site is the O atom location after optimization. E_a[b] is the adsorption energy

Table 5.4: O atom internal adsorptions.

Position				
Initial site	Final site[a]	E_a[b] (eV)	HOMO-LUMO gap (eV)	Mulliken charge gained by O atom |e|
Ge top	Attached to both Si and Ge	4.97	1.16	0.45
Ge top - 2nd	Attached to both Si and Ge	4.96	1.05	0.46
Si top	Broke Si-Si bond	6.10	1.18	0.59
Si top - 2nd	Attached to both Si and Ge	4.58	1.18	0.45
Si-Ge bridge	Attached to both Si and Ge	4.97	1.16	0.45
Si-Ge bridge - 2nd	Broke Si-Ge bond	4.99	1.19	0.53
hollow	Broke Si-Ge bond	4.97	1.08	0.46
Si-Si bridge	Broke Si-Si bond	6.10	1.18	0.59
Ge-Ge bridge	Attached to both Si and Ge (skipped the middle atom)	4.97	1.08	0.46

[a]Final site is the O atom location after optimization. [b]E_a is the adsorption energy

Again we have performed a calculation with SiGeNT + 24 O, in order to understand the consequences of SiGeNT exposed into O rich environment. Similar to SiGeNT + 24 H system we brought in O internally and externally and let it fully optimized. In Figure 5.7 we present the final optimized structure. Structurally adding O expands the SiGe bond lengths and it is visible in side view of the system in Figure 5.7. However, the DOS of this system (refer Figure 5.8) shows that unlike adding H, adding the same number of O resulted in decrease of HOMO-LUMO energy gap from 1.27eV to 0.99eV. Furthermore, the average charge gain of O is ~0.52|e| which indicates attachment of O kept its originality which is the ionic bonding nature.

The interesting question would be why HOMO-LUMO energy gap decreased with multiple O atom adsorptions. In their work, Adhikari *et. al*. [124,125] reported that the ionic character of a system, the curvature of the nanotube and the hybridization of constituent atoms of the NT plays a major role in determining the HOMO-LUMO energy gap of nanotubes. However, comparing the average charge gained by an O atom in the system of SiGeNT + 24 O system and atomic O adsorption cases have very similar values (~0.5|e|). In addition, the O atoms being incorporated into the tube wall and not onto “top” sites made the hybridization of Si and Ge atoms unchanged. Therefore the HOMO-LUMO energy gap decrease is not due to ionic character of the system or the hybridization of the atoms. Nevertheless, due to incorporation of O into Si-Si, Si-

Ge and Ge-Ge, these bonds elongated. Si-Si bonds stretched from average value of 2.30 Å to 3.27 Å, Si-Ge bonds stretched from average value of 2.35 Å to 3.06 Å and Ge-Ge bonds stretched from average value of 2.4 Å to 3.12 Å. Therefore stretching of these bonds makes the SiGe (6,6) NT less curved, resulting in reduction of HOMO-LUMO energy gap.

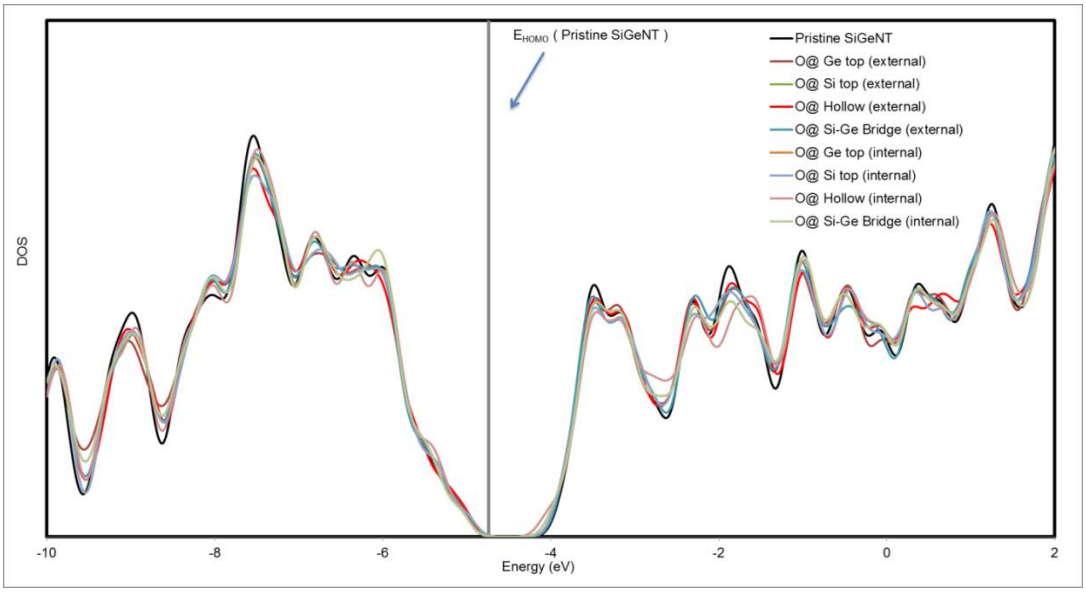

Figure 5.6: DOS of the pristine SiGeNT and the external and internal adsorptions of O on SiGeNT. Vertical line is the reference line for HOMO energy of pristine SiGeNT.

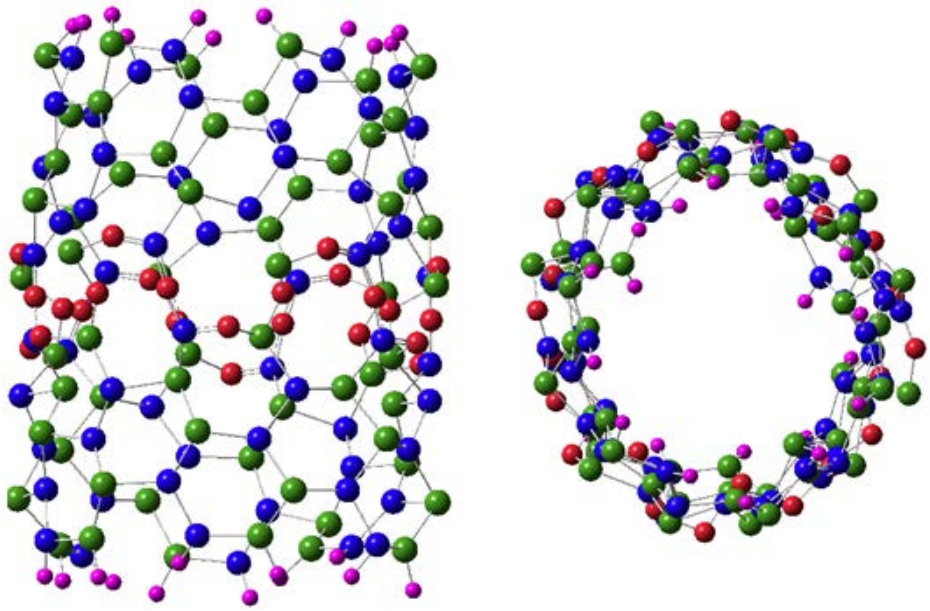

Figure 5.7: Side and top view of optimized SiGeNT + 24 O system. Atoms are in usual colors and only the middle layer is saturated with O in order to negate the edge effects.

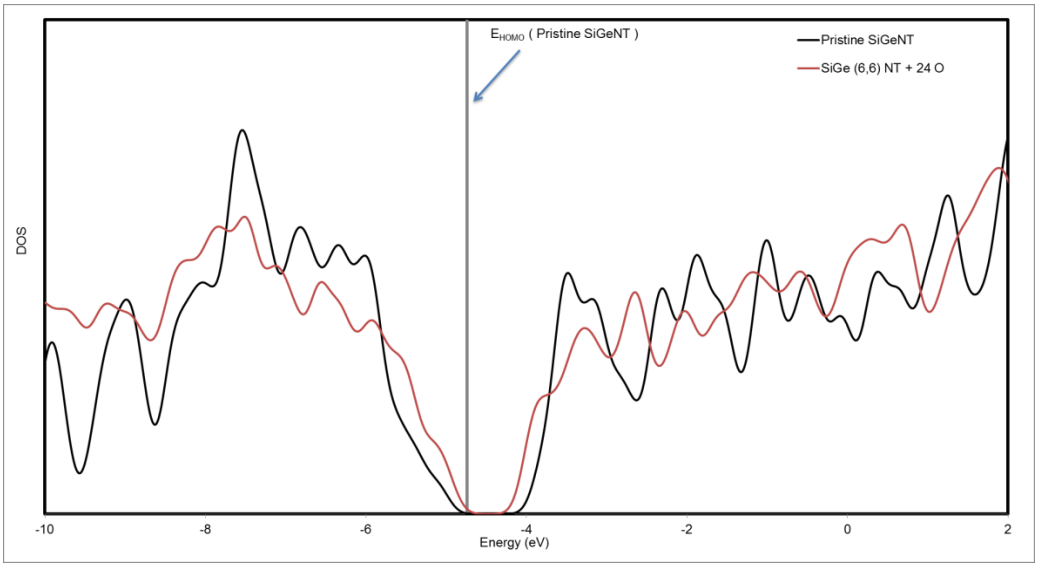

Figure 5.8: DOS of the pristine SiGeNT and SiGeNT + 24 O system. The vertical line is the reference line for HOMO energy of pristine SiGeNT.

5.2.3 H molecular adsorption

Next we focused on the H molecular (H_2) interaction on SiGeNTs. Due to geometric nature of H_2, we can identify two separate orientations for the adsorption. H_2 is being parallel to the tube axis and H_2 is being perpendicular to the tube axis (two images on Figure 5.9 can be referred as such arrangement). Since the H atomic adsorption clearly indicated that the energetically favored adsorptions are onto "Si top" and "Ge top" sites, we only performed the H_2 molecule adsorption on "Si top" and "Ge top" sites.

We present our results in Table 5.5. We noticed that after optimization, H_2 molecule always has the perpendicular to tube axis orientation (In Figure 5.9 we present such a geometry change). In addition we found that the H-H bond length of H_2 molecules in all cases has the value of 0.75 Å which indicates that the H_2 molecules remain intact. Our initial distance from the closest H atom of the H_2 molecule to the SiGeNT tube wall has increased after optimization (initial value is 1.5 Å) up to ~3.0 Å (exact values tabulated in Table 5.5). Adsorption energies are very small compared to H and O atomic adsorptions. HOMO-LUMO energy gaps indicated no change from pristine SiGe(6,6) NT value. DOS of this system is shown in Figure 5.10 for few selected cases and it is clear that the H_2 molecular interactions with SiGeNT are very minimal. Adsorption type of H_2 onto SiGeNT can be categorized as physisorption in nature due to very low adsorption energy

(~ 0.04 eV) along with no change in HOMO-LUMO gap and the distance from NT wall to H_2 is ~3.0 Å. Further examination on H_2 molecule revealed that the charge transfer is negligible (on the order of 10^{-3} in the units of electronic charge).

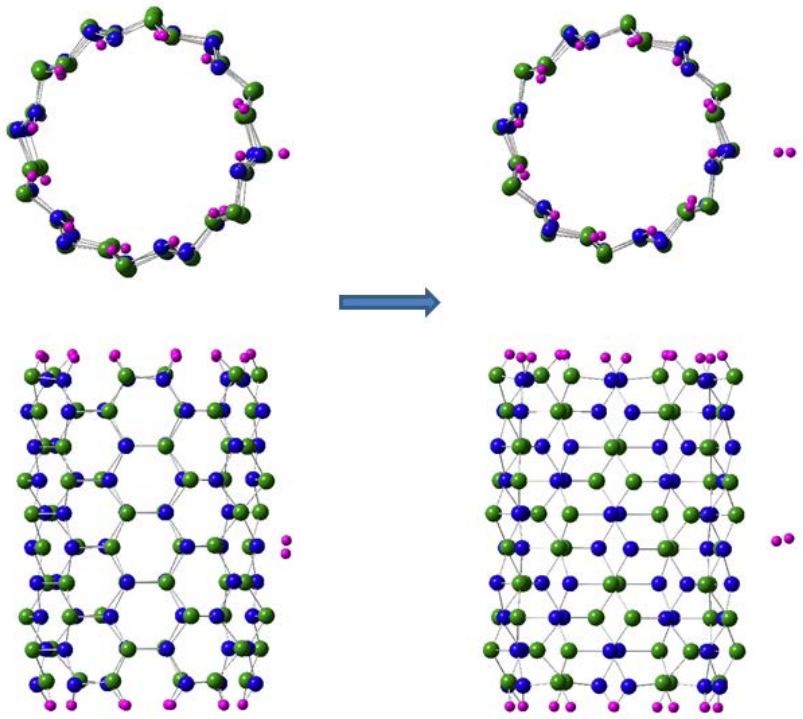

Figure 5.9: Top and side view of before and after optimization of SiGeNT + H2 system.

Table 5.5: H2 molecule external and internal adsorptions.

Orientation	Position		E_a[b] (eV)	HOMO-LUMO gap (eV)	D_{Si-H} or D_{Ge-H}[c] (Å)	D_{H-H}[d] (Å)
	Initial site	Final site[a]				
External H_2 adsorption						
Parallel	Ge top	Perpendicular and close to Ge top	0.04	1.27	3.02	0.75
	Si top	Perpendicular and close to Si top	0.02	1.27	3.14	0.75
Perpendicular	Ge top	Perpendicular and close to Ge top	0.03	1.27	3.06	0.75
	Si top	Perpendicular and close to Si top	0.02	1.27	3.18	0.75
Internal H_2 adsorption						
Parallel	Ge top	Perpendicular and close to Ge top	0.04	1.27	3.02	0.75
	Si top	Perpendicular and close to Si top	0.02	1.27	3.14	0.75
Perpendicular	Ge top	Perpendicular and close to Ge top	0.03	1.27	3.06	0.75
	Si top	Perpendicular and close to Si top	0.02	1.27	3.18	0.75

[a]Final site is the H_2 molecule location after optimization. [b]E_a is the adsorption energy. [c]D_{Si-H} or D_{Ge-H} is the distance from closes H atom of the H_2 molecule to closes Si or Ge atom. [d]D_{H-H} is the distance between H atoms.

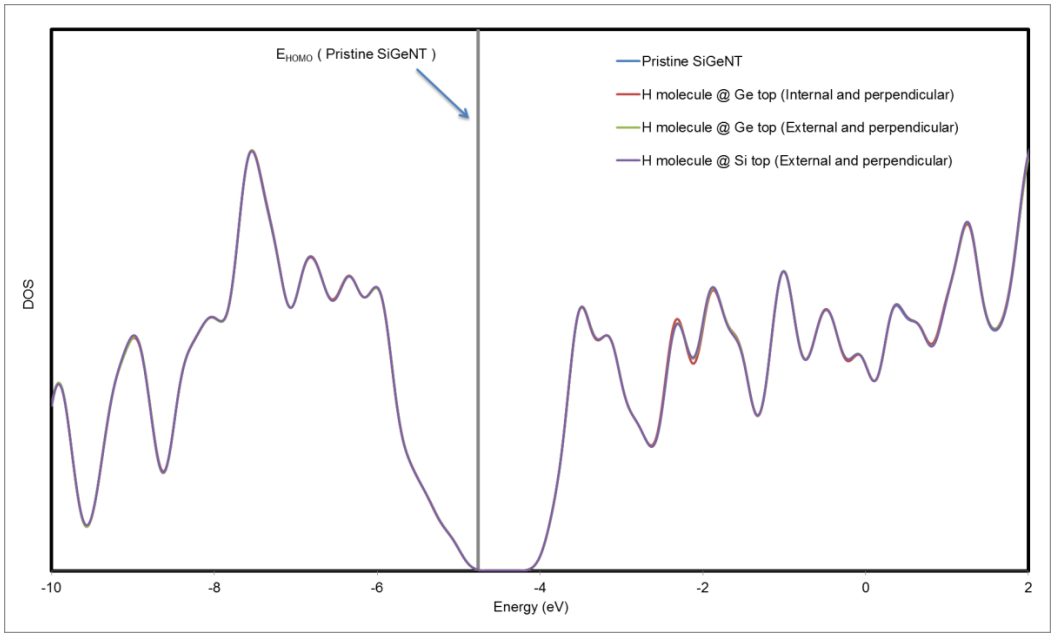

Figure 5.10: DOS of the pristine SiGeNT and SiGeNT + H2 system. The vertical line is the reference line for HOMO energy of pristine SiGeNT.

5.2.4 O molecular adsorption

Unlike the H_2 adsorption we could not reduce the number of initial O molecular (O_2) adsorption sites due to diverse final adsorption sites observed in O atomic adsorptions. Furthermore, as in H_2 adsorptions we have parallel and perpendicular orientations with respect to tube axis. In Figure 5.11, we present the final adsorptions of O_2 on SiGe (6,6) NT. In Tables 5.6-5.9 we present the results of O_2 adsorptions.

We note that unlike the O atomic adsorptions, majority of O_2 tend to attached into "Si top" or "Ge top" sites while keeping the O-O distance to ~1.6 Å. This indicates the molecular nature of O is still intact but with extended bond length. The adsorption energies of O_2 are less compared to atomic O adsorption. However there are several situations when the adsorption energy reach ~6.0 eV. In such situations the O_2 is attached into Si rich local environment. In addition the O-O distance is more than 2.0 Å indicating that the O_2 has dissociated and treated as two individual adsorptions. Also it is worth mentioning that if O_2 attached into Ge rich environment, the adsorption energy is relatively low (~2.0 eV). This is another indication of the reluctance GeO_2 formation and keenness of SiO_2 formation.

The Mulliken charge of atomic O after adsorption is ~-0.5|e| and in general the Mulliken charge of O atoms in O_2 adsorptions are ~ -0.3|e| per atom

and it is acceptable since two O atoms are competing to get the charge from the SiGeNT in close vicinity. The HOMO-LUMO energy gap values have spread out in wide range. The values vary between 0.46 eV and 1.25 eV. This indicates in general the gap has decreased. Since the O atoms of O_2 are attaching onto "Si top" or "Ge top" sites (Figure 5.11), it brings the reasonable doubt whether the big drop of HOMO-LUMO gap are similar to what we observe in H atomic adsorption (generation of defect state around the frontier orbital region). In Figure 5.12 we present the DOS of several O_2 adsorptions on SiGeNT. From the DOS we can identify that some adsorption sites (Ge top 2^{nd} external adsorption-parallel to tube axis orientation) follow the DOS of pristine SiGeNT which points to the relatively smaller decrease of HOMO-LUMO gap, while the other cases show the rise of a defect density which indicates the higher gap decrease cases. Additionally the much broader defect density is visible in DOS (Figure 5.12) due to having two defect density states around the frontier orbital region.

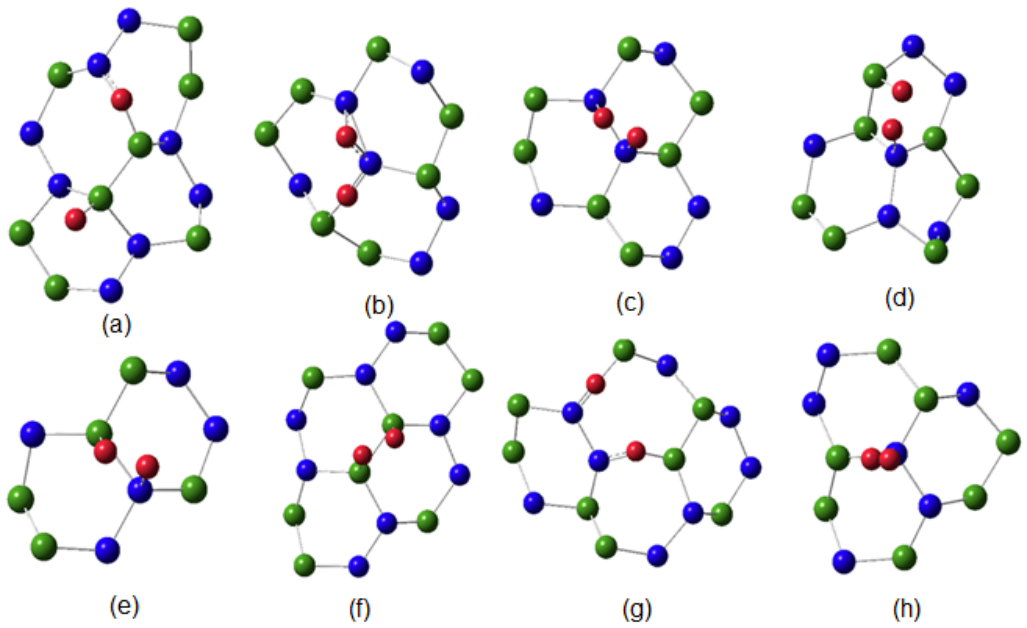

Figure 5.11: O2 attachments. (a) B. the Si-Ge and Si top (b) B. the Si-Ge and A. to Si-Si (c) A. to Si-Si and Si top (d) Ge top and Si top (skip the middle atom) (e) Ge top and Si top (f) two Ge tops (g) B. Si-Ge (h) A. to Ge as O2. B: bond breaking and A: attached.

Table 5.6: O2 molecule external and parallel to tube axis adsorptions.

Position		D_{O-O}[b] (Å)	HOMO-LUMO gap (eV)	E_a[c] (eV)	Mulliken charges gained by O atoms |e|
Initial site	Final site[a]				
Ge top	Ge top and broke Si-Ge bond	4.80	1.17	2.08^{+}	0.40 and 0.52
Ge top - 2nd	Si top and Ge top	1.58	1.19	3.13^{++}	0.48 and 0.54
Si top	Attached to Si-Si and broke Si-Ge bond	2.70	0.98	6.27^{+}	0.32 and 0.26
Si top - 2nd	Si top and Si top	1.58	1.14	3.17^{++}	0.32 and 0.31
Si-Ge bridge	Si top and Ge top (expanded Si-Ge bond from 2.35 Å to 3.19 Å	1.56	0.86	2.56^{++}	0.31 and 0.27
Si-Ge bridge - 2nd	Si top and Ge top	1.58	1.00	2.67^{++}	0.32 and 0.26
hollow	Si top and Ge top (skipped the middle atom)	1.56	0.63	3.05^{++}	0.30 and 0.24
Si-Si bridge	Si top and Si top	1.58	1.14	3.17^{++}	0.32 and 0.31
Ge-Ge bridge	Ge top and Ge top	1.56	1.07	1.94^{++}	0.26 and 0.27

[a]Final site is the O_2 molecule location after optimization. [b]D_{O-O} is the distance between O atoms of the O_2 molecule. [c]E_a is the adsorption energy, $^{+}$calculated using equation 3. $^{++}$ Calculated using equation 2. Initial O-O distance is 1.32 Å.

Table 5.7: O2 molecule external and perpendicular to tube axis adsorptions.

Position					
Initial site	Final site[a]	D_{O-O}[b] (Å)	HOMO-LUMO gap (eV)	E_a[c] (eV)	Mulliken charges gained by O atoms |e|
Ge top	Ge top and Ge top	1.56	1.08	3.17^{++}	0.26 and 0.27
Ge top - 2nd	Si top and Ge top (skipped the middle atom)	3.25	0.81	5.12^{+}	0.53 and 0.52
Si top	Broke 2 Si-Ge bonds	1.57	0.94	3.40^{++}	0.32 and 0.23
Si top - 2nd	Attached to Si-Ge bond and attached to Si-Si bond	2.83	0.70	5.65^{+}	0.46 and 0.48
Si-Ge bridge	Attached to Si as a O molecule	1.44	0.46	2.61^{++}	0.31 and 0.08
Si-Ge bridge - 2nd	Si top and Ge top (skipped the middle atom)	1.56	1.00	3.53^{++}	0.29 and 0.25
hollow	On hollow site	1.31	1.24	2.39^{++}	0.02 and 0.00
Si-Si bridge	Si top and Ge top (skipped the middle atom)	1.59	0.87	3.11^{++}	0.34 and 0.22
Ge-Ge bridge	Si top and Ge top	1.43	0.56	2.68^{++}	0.21 and 0.11

[a]Final site is the O_2 molecule location after optimization. [b]D_{O-O} is the distance between O atoms of the O_2 molecule. [c]E_a is the adsorption energy, $^{+}$calculated using equation 3. $^{++}$ Calculated using equation 2. Initial O-O distance is 1.32 Å.

Table 5.8: O2 molecule internal and parallel to tube axis adsorptions.

Position		D_{O-O}[b] (Å)	HOMO-LUMO gap (eV)	E_a[c] (eV)	Mulliken charges gained by O atoms |e|
Initial site	Final site[a]				
Ge top	Si top and Ge top (skipped the middle atom)	1.57	0.70	3.64^{++}	0.32 and 0.25
Ge top - 2nd	Ge top and Ge top (skipped the middle atom)	1.56	0.71	3.35^{++}	0.27 and 0.27
Si top	Si top and Si top	1.62	1.07	4.08^{++}	0.33 and 0.30
Si top - 2nd	Si top and Ge top	1.59	0.95	3.92^{++}	0.34 and 0.24
Si-Ge bridge	Broke Si-Si bond and attached to Si-Si bond	2.71	0.97	6.11^{+}	0.54 and 0.58
Si-Ge bridge - 2nd	Attached to Si as a O molecule	1.58	0.86	3.97^{++}	0.33 and 0.24
hollow	Attached to Si-Ge bond and attached to Si-Ge bond (skipped middle atom)	3.77	1.02	5.22^{+}	0.45 and 0.47
Si-Si bridge	Si top and Si top	1.62	1.07	4.08^{++}	0.33 and 0.30
Ge-Ge bridge	Attached to Si-Si bond and attached to Si-Si bond	3.34	1.25	5.50^{+}	0.50 and 0.52

[a]Final site is the O_2 molecule location after optimization. [b]D_{O-O} is the distance between O atoms of the O_2 molecule. [c]E_a is the adsorption energy, $^{+}$calculated using equation 3. $^{++}$ Calculated using equation 2. Initial O-O distance is 1.32 Å.

Table 5.9: O2 molecule internal and perpendicular to tube axis adsorptions.

Position		D_{O-O}[b] (Å)	HOMO-LUMO gap (eV)	E_a[c] (eV)	Mulliken charges gained by O atoms |e|
Initial site	Final site[a]				
Ge top	Attached to Si-Si bond and broke the Si-Si bond	1.90	0.97	6.11^{+}	0.27 and 0.32
Ge top - 2nd	Ge top and broke Si-Si bond	1.62	1.00	3.89^{++}	0.22 and 0.39
Si top	Attached to Si-Ge bond and attached to Ge-Ge bond	3.34	0.59	4.63^{+}	0.47 and 0.44
Si top - 2nd	Si top and Ge top	1.57	1.07	4.08^{++}	0.33 and 0.30
Si-Ge bridge	Si top and Ge top (skipped the middle atom)	1.59	0.93	3.59^{++}	0.31 and 0.23
Si-Ge bridge - 2nd	Si top and Ge top (skipped the middle atom)	1.58	0.99	3.79^{++}	0.33 and 0.23
hollow	Ge top and Ge top (skipped the middle atom)	1.56	0.75	3.36^{++}	0.27 and 0.27
Si-Si bridge	Ge top and attached to Si-Si bond	1.58	1.21	3.68^{++}	0.23 and 0.36
Ge-Ge bridge	Broke Ge-Ge bond and broke Si-Si bond	2.76	1.16	5.12^{+}	0.49 and 0.57

[a]Final site is the O_2 molecule location after optimization. [b]D_{O-O} is the distance between O atoms of the O_2 molecule. [c]E_a is the adsorption energy, $^{+}$calculated using equation 3. $^{++}$ Calculated using equation 2. Initial O-O distance is 1.32 Å.

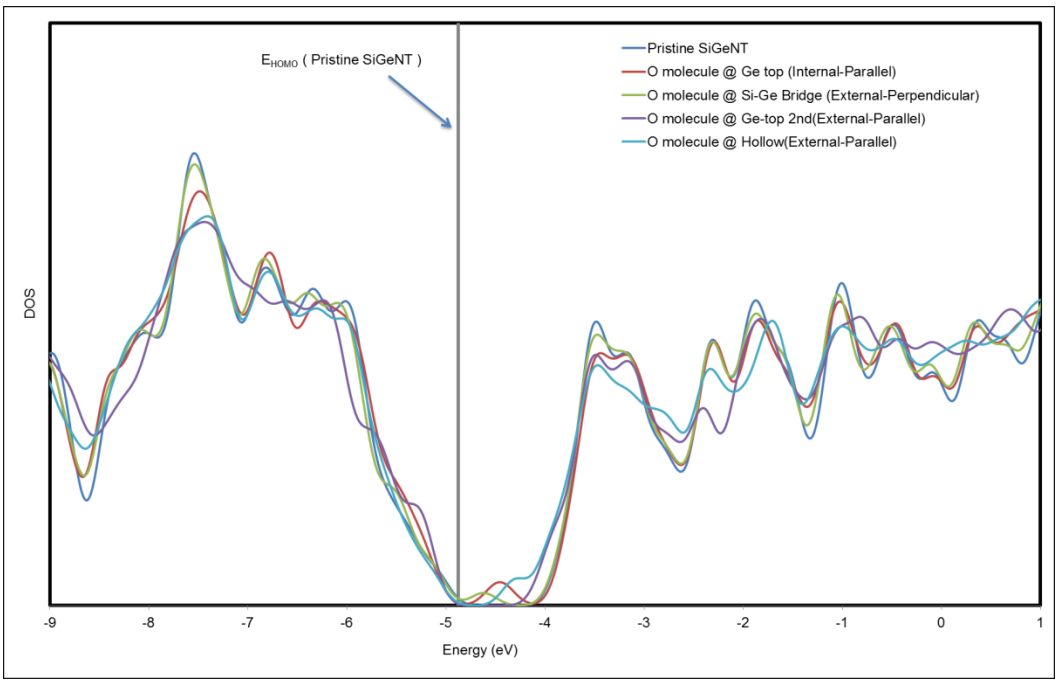

Figure 5.12: DOS of the pristine SiGeNT and the external and internal adsorptions of O2 on SiGeNT. Vertical line is the reference line for HOMO energy of pristine SiGeNT.

Chapter 6

Fully hydrogenated sp^3-hybridized SiGe Nanoribbons

6.1 Introduction

As we discussed in last few Chapters and in introduction, the success in synthesizing carbon nanostructures and the extraordinary properties they exhibited [1] triggered many researches [2-11] on nanostructure materials. Among those researches, finding nanostructures from other elements and compounds similar to carbon nanostructures took much attention. Specifically, the Si-based nanostructures [77-82,85-88], where once realized, could be highly compatible with existing Si micro/nanoelectronic [12,13] technologies.

It is also found that alloying of Si and Ge give rise to nanostructures quite easily. Their 4% built-in lattice mismatch aids in creating nanotubes [27,28]. In addition, alloying of these two elements [27,28] develop some properties that are absent in their elemental level. For example, Si and Ge both shows the indirect band gap nature in their elemental level but when alloyed could show direct band gap nature [27,28]. On the other hand, Ge has higher carrier mobility (electron mobility ~3900 $cm^2V^{-1}s^{-1}$ and hole mobility ~1900 $cm^2V^{-1}s^{-1}$) with respect to Si (electron mobility ~1500 $cm^2V^{-1}s^{-1}$ and hole mobility ~450 $cm^2V^{-1}s^{-1}$) [27,28] and being isoelectronic to Si, SiGe enables higher carrier speed and reduces the cost [27]. Furthermore, in Ge, the direct band gap at Γ point is only ~0.15 eV higher

compared to the indirect band gap of 0.65 eV. This small gap nature of Ge can be used to unravel near infrared responsivity of Si-based photonics [117,126]. Alloying of Si and Ge on bulk phase and thin films were already in practice of semiconductor industry for some time now [87,126-130].

Though C, Si, and Ge all reside in the same column, Si and Ge prefer sp^3 hybridized bonding while C prefers sp^2 hybridized bonding. As a consequence, carbon-based nanostructure materials have much smooth surface while SiGe based materials inherit more puckered surface structure. This wiggled surface could be very useful in situations where it is used as an adsorption material due to the fact that the adsorbates may screen from one another and lead into increasing the adsorbates density [116]. In the current work, our focus is on SiGe nanoribbons (NRs), where it is important not only in complementary metal-oxide semiconductor (CMOS) or heterojunction bipolar transistor (HBT) but also as optical or electrical interconnections in Si micro/nanoelectronics.

Similar to nanotube structure Nanoribbon structure also provides the quasi-one-dimensional transition to charge carriers, and high surface to volume ratio. In addition, the terminated edges trigger the edge effects [16] while its overall size provides quantum confinement effects [14,15]. These are very novel phenomena that govern many properties of nanostructures and extremely useful in many applications. There are several experimental and theoretical works reported on SiGeNRs. Sahin *et. al.* have performed a very extensive study on group IV

homo and heteronuclear NR structures [131], and found that the SiGe NRs of honeycomb lattice structure is stable as a low buckled structure. Eberal and Shimdt [90] reported the successful synthesizing of SiGe nanolayers, and using selective etching process in order to convert those nanolayers into nanotubes. In addition, Zang *et. al.* reported that they have designed Si and Ge layered nanoribbons [91] and after optimization, the NRs were curved due to built-in strain-stress imbalance. Also Zhang *et. al.* reported that they have successfully synthesized wiggled SiGe nanoribbons deposited onto Si substrate which can be used as a stretchable electronic material [132].

Despite some theoretical studies of planar SiGeNRs, it is commonly agreed that SiGeNRs on honeycomb lattice structure is stable only in low buckled nature. Furthermore, all these studies have been based on the idea of having SiGe deposited onto a substrate material. In this work, we moved a step further from that and tried to identify and understand the SiGeNRs ability to survive as a standalone structure. Additionally, the reported work so far for SiGe work have followed the atomic arrangement of SiC " type I " [133] arrangement where Si and Ge atoms have alternative attachment into the honeycomb lattice nodes. However, our previous studies [116,123] have revealed that even though for the SiC " type I " is clearly the most stable, for SiGe, all four types reported have very close energies that it is unable to point out that one particular type is more stable than the other.

Hence, we have studied SiGeNR of types I, II and III in both armchair (AC) and zigzag (ZZ) categories. Here, the AC and ZZ nature is determined with the terminating edge shape similar to graphene nanoribbons. However due to computational cost, width dependence of the NRs to the electronic structure was calculated only for the " type I " AC and ZZ SiGeNRs. In addition, we have designed the Si and Ge atoms to be in perfect sp^3 hybridization and all the dangling bonds were saturated with hydrogen atoms. Therefore, the studied SiGeNR structures were fully hydrogenated. As a consequence, the structures are much stable, and the band gaps reported are the maximum value that can be achieved with respect to their respective width size.

6.2 Results and discussion

Calculations presented here in this work have been carried out using density functional theory (DFT) and periodic boundary conditions implemented in Gaussian 09 [48] suite of programs. We have employed screened-exchange hybrid functional, HSE06 [134] created by Heyd, Secuseria and Ernzerhof, along with all electron basis set 6-311G (d,p) [95] for these calculations.

The reciprocal space integration has been performed with a uniform mesh of 100 and 86 k-points for armchair and zigzag nanoribbons, respectively. Width dependence on the electronic structure properties have been calculated only with

respect to the type I structures for both armchair (AC) and zigzag (ZZ) categories with widths changing from 4.4 Å to 19.9 Å and 7.3 Å to 27.5 Å respectively. Calculations on all the other types, Type II, III and IV have been performed on width sizes of 19.9 Å and 27.5 Å for armchair and zigzag categories, respectively.

All the structures have been fully relaxed without any symmetry constraints until their maximum and root mean square atomic forces are less than 0.02 and 0.015 eV/Å respectively. Additionally, the maximum and root mean square atomic displacements in consecutive cycles were less than 1×10^{-3} and 6×10^{-4} Å, respectively. The cohesive energy per atom of the nanoribbons was calculated using following equation:

$$E_c = \frac{[E_{NR} - n(E_{Ge} + E_{Si} + 2E_H)]}{4n}, \quad (6.1)$$

where E_{NR} is the total ground state energy of the SiGe nanoribbon, while $E_{Ge,}$ E_{Si} and E_H are the total ground energies of Ge atom, Si atom and H atom respectively. In addition, n is the number of atoms in particular atom type. In all our structures the stoichiometry for Si:Ge:H is 1:1:2.

6.2.1 Type I SiGe nanoribbons

Atomic arrangement of all nanoribbon types are followed by the previously reported work and adopted the same naming. Figure 6.1 shows the

images of type I in both AC and ZZ nanoribbon categories. Since Si and Ge atoms in these nanoribbons are in sp^3 hybridization state, two consecutive atoms always belong to two different lattice planes and it is visible in side views of the images in Figure 6.1.

In Table 6.1, we report the results of SiGe AC nanoribbons. The main observation is once optimized, nanoribbons have gained a curvature. There is no curvature gain for the smallest width nanoribbon since it has no adequate width. We have calculated the curvature using the following equation.

$$\mathrm{K} = f''(x) = \frac{\mathrm{d}^2\mathrm{y}}{\mathrm{dx}^2}, \tag{6.2}$$

where K is the curvature gained and is defined as the second derivative of the surface function.

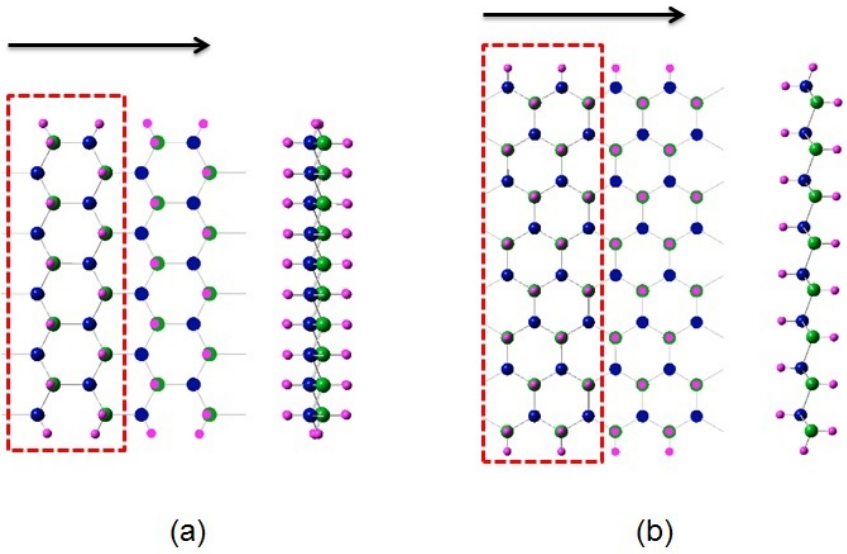

Figure 6.1: (a) Top and side view of type I AC SiGeNR (b) Top and side view of type I ZZ SiGeNR. Black arrow shows the growth direction of the nanoribbons. Red dashed box indicates the unit cell used for the calculations. Si, Ge and H atoms are in blue, green and pink colors.

We have fitted for each line of atoms that perpendicular to growth direction of the nanoribbon a second order function. Then their respective curvatures were calculated and finally the average curvature was calculated. As the nanoribbons get wider, NRs gained more curvature. It can be clearly seen in Figure 6.2. In addition from the Table 6.1, we can identify the curvature of the NRs become saturated around 0.4 A^{-1}. The cohesive energies of the NRs also increases and saturates as the width increases. The band gaps of the NRs have the decreasing and saturating trend as width increase similar to the SiGe NTs results presented in Chapter 1.

Having highest band gap for the smallest width and gradual decrease of the band gap values as width increase implies the action of quantum confinement effects where for the most confined structure has the highest band gap and as the confinement of the NRs become less, the band gaps decrease. Figure 6.2 shows the optimized structures of the type I SiGeNRs. According to Figure 6.2, it is clear that the SiGeNRs are rearranging towards the SiGe nanotubes.

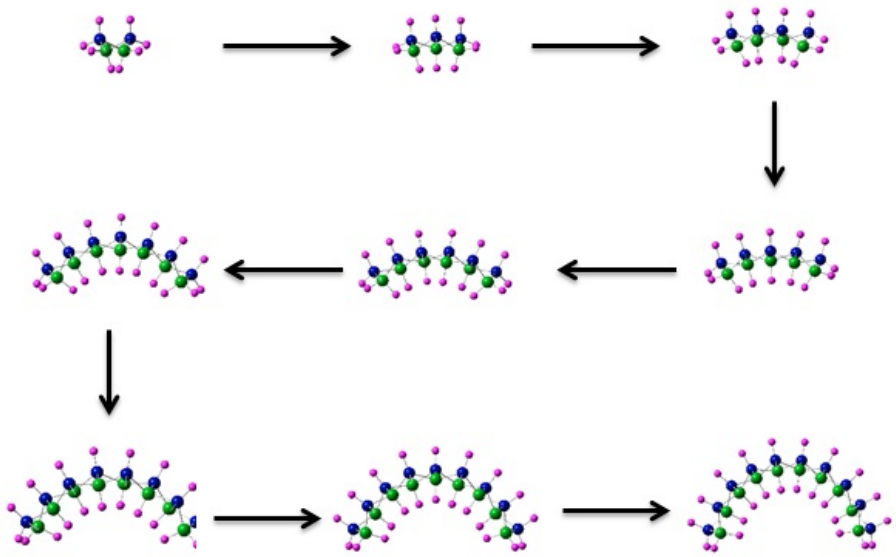

Figure 6.2: Side views of Type I AC SiGeNRs. Images indicate the gain of curvature as the nanoribbon width increases. Atoms have usual colors.

Table 6.1: Optimized properties of Type I armchair SiGeNRs.W is the nanoribbon width before the optimization of the NRs, E_a is the cohesive energy per atom, E_{gap} is the band gap of a nanoribbon of particular width, K is the curvature gained by the nanoribbon when optimized and p orbital % is the percentage of the p orbitals within the nanoribbons.

W (Å)	E_a (eV)	E_{gap} (eV)	K ($Å^{-1}$)	p orbital %
4.4	3.0	5.9	0.0	8.3
6.3	3.1	5.0	0.1	2.8
8.3	3.2	4.3	0.3	4.2
10.3	3.2	4.0	0.3	3.3
12.2	3.3	4.0	0.4	5.6
14.1	3.3	4.0	0.4	6.0
16.1	3.3	3.4	0.4	6.3
18.0	3.4	3.4	0.4	6.5
19.9	3.4	3.4	0.4	6.7

This observation is similar to the results shown by Eberal and Shimdt [90] for experimental realization of SiGe nanotubes where when they etched the attached substrate, the SiGe nanolayers formed into nanotubes. Another observation is the direction of the NRs has bended. It is always towards the Ge lattice. We observed this bending more intensively in zigzag category (refer Figure 6.3).

This type of behavior is also observed in the work performed by Zang *et. al.* [91] where Ge was the inner layer of the developed nanotubes. According to the atomic arrangement of type I, one type of atoms is always surrounded by the other type. Hence, Ge atoms belong to one lattice and the Si atoms belong to another lattice (refer side views of Figures 6.1a and 6.1b). The two lattices (Si lattice and Ge lattice) act as individual lattices even though they are entangled and saturated with hydrogen atoms as one lattice. The intrinsic surface stress in these materials becomes dominant at nanoscale. In this particular case, surface stress by two lattices has an inequality since one lattice is Si and the other lattice is Ge. Similar to Zang *et al.*'s [91] work, Ge stress is compressive while for Si it is tensile. Hence the built-in stress imbalance is the reason for spontaneous bending of type I SiGeNRs. In addition, we have performed another two calculations with all Si atoms and all Ge atoms NRs. Both started with exact sp^3 bonded Si or Ge atoms with dangling bonds saturated with hydrogen atoms. It is found that after

optimization all Si atoms NR did not gain any curvature while all Ge atoms NR gained a curvature similar to type I SiGeNRs (refer Figure 6.4).

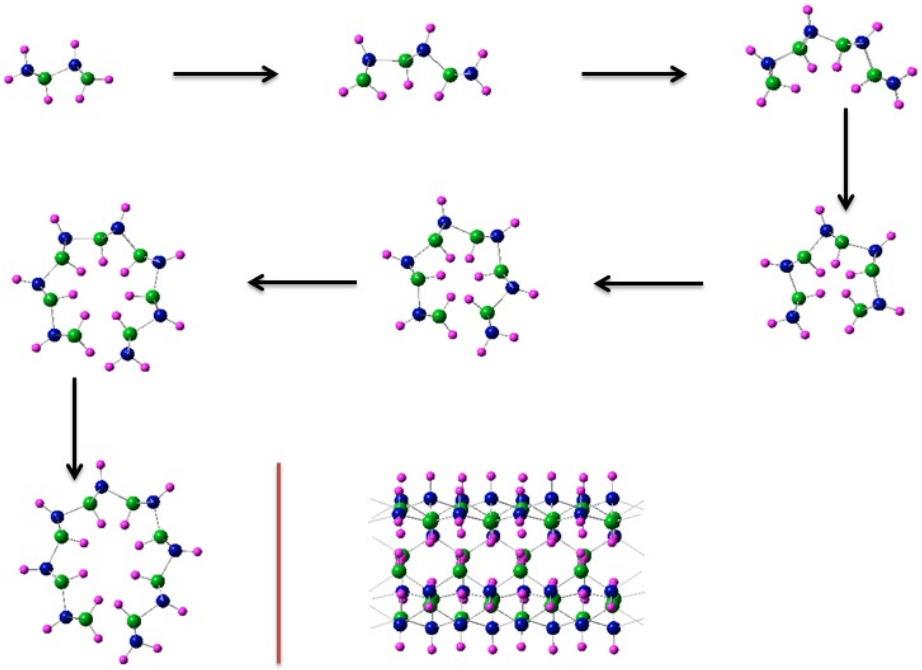

Figure 6.3: Side views of type I ZZ SiGeNRs. Images indicate the gain of curvature and becoming nanotube like structure as the nanoribbon width increases. Image separated by the red line is another side view of the largest studied SiGeNR of the ZZ category.

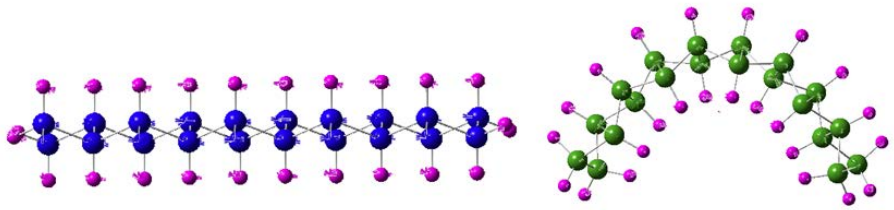

Figure 6.4: Side views of (a) all Si AC nanoribbon and (b) all Ge AC NR. Atoms have usual colors.

Table 6.2: Optimized properties of type I zigzag SiGeNRs.W is the nanoribbon width before the optimization of the NRs, E_a is the cohesive energy per atom, E_{gap} is the band gap of a nanoribbon of particular width, K is the curvature gained by the nanoribbon when optimized and p orbital % is the percentage of the p orbitals within the nanoribbons.

W (Å)	E_a (eV)	E_{gap} (eV)	K ($Å^{-1}$)	p orbital %
7.3	3.2	3.6	0.0	1.5
9.7	3.3	3.3	0.1	3.2
14.1	3.3	3.1	0.3	5.6
16.5	3.4	3.2	0.3	6.1
20.9	3.4	2.9	0.4	6.6
23.3	3.5	2.9	0.4	6.8
27.5	3.5	2.9	0.4	7.1

It is also reported in literature that the heavier group 14 elements prefer to bond through p orbitals without hybridizing with s orbitals [98] for the simple fact that heavier group 14 elements are inefficient in making strong hybridized orbitals. Since the bond lengths are larger in those heavier group 14 elements, making σ bonds with p orbitals is more stable rather than making π bonds. If the p orbital σ bonds are made, the bonds in those atoms should contain 90 degree bond angles since p orbitals are 90 degrees apart. Therefore in the bended SiGe NRs or all Ge atoms NR make p orbitals σ bonds, the 90 degree bond angles should be present instead of 109.5 degree bond angles (sp^3 bonding is around 109.5 degree angle), at least for part of the bond angles. When analyzed, all Ge atoms NR have ~7% of its bond angles made out of 90 degree bond angle. Similarly, in Type I SiGeNRs, p orbital bonding is present, and at the maximum length, it is close to 7% (refer Tables 6.1 and 6.2).

In Figure 6.5, we present the band gap structures of SiGe AC and SiGe ZZ nanoribbons (the largest widths we have studied). In addition, the reported band gaps for SiGe type I AC NR in Table 6.1 are indirect and for SiGe type I ZZ NR in Table 6.2 are direct in nature. Furthermore it is visible in Figure 6.5b where direct minimum band gap is occurring at Γ point.

6.2.1 Type II and III SiGe nanoribbons

Furthermore, we have studied the SiGe type II and type III nanoribbons of AC and ZZ categories. As shown in Figure 6.6, the main difference between the

type I NR and the type II and III NR is the curvature gain. None of the type II or III NRs in any category have gain the curvature. Following the same reasoning, we can claim that it is visible that in Figure 6.6 two lattices are equal. Hence there is no stress in-balance in type II or III in any category which result in keeping the quasi flat nature. Furthermore, in AC category the SiGe type II and III NRs show cohesive energies of 3.4 eV and 3.4 eV respectively. In addition their band gaps are 3.1 eV (indirect) and 3.3 eV (indirect), respectively. In ZZ category the SiGe type II and III NRs show cohesive energies of 3.4 eV and 3.4 eV respectively. In addition their band gaps are 3.0 eV (direct) and 3.1 eV (direct), respectively.

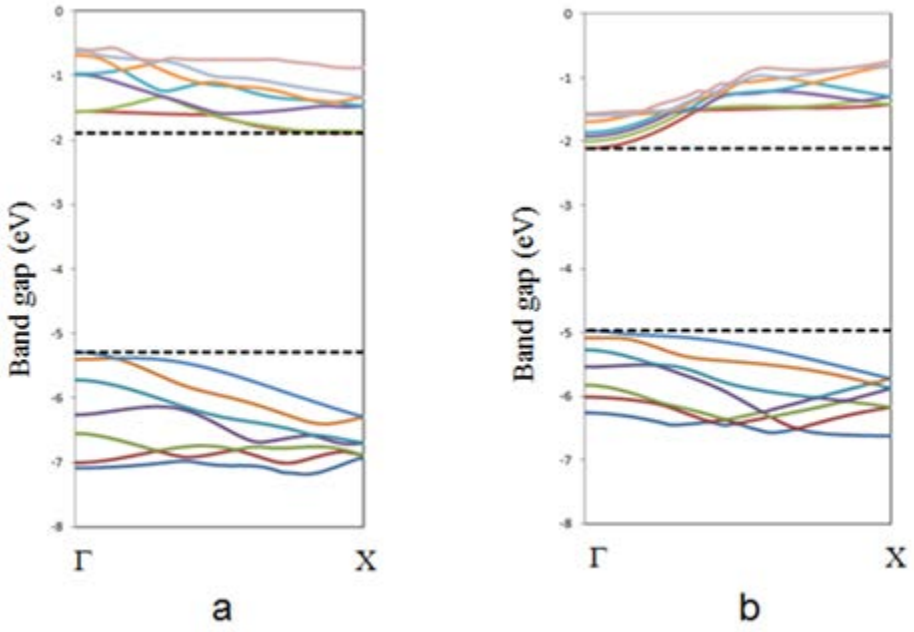

Figure 6.5: Band structures of (a) SiGe type I AC NR (width=19.9 Å) and (b) SiGe type I ZZ NR (width=27.5 Å).

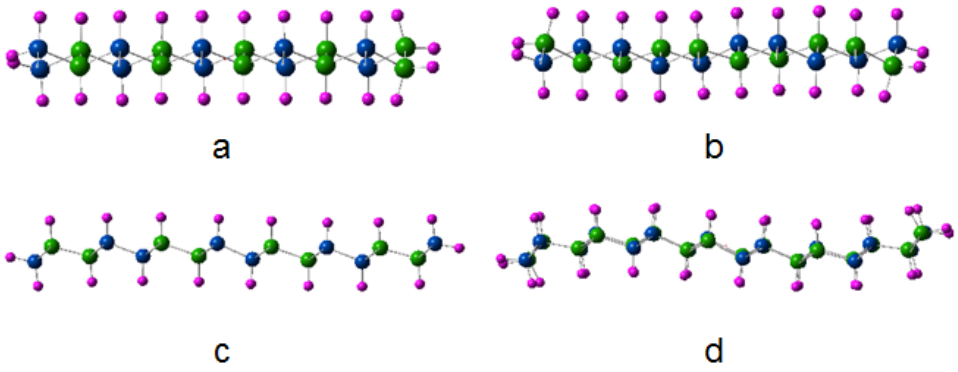

Figure 6.6: Side views of optimized (a) SiGe type II AC NR (width=19.9 Å) (b) SiGe type III AC NR (width=19.9 Å) (c) SiGe type II ZZ NR (width=27.5 Å) and (d) SiGe type III ZZ NR (width=27.5 Å)

Chapter 7

Ultrathin α-Fe_2O_3 Nanoribbons from (110) and (104) Surfaces

7.1 Introduction

In this Chapter, we are shifting our focus towards the second method introduced in introduction Chapter. Here the top down approach based nanostructures are focused and in that regard we have focused on hematite nanoribbons. α-Fe_2O_3, also known as hematite, is the most stable iron oxide form in ambient conditions. It is a semiconductor, with an indirect band gap of ~2.1 eV[135]. Hematite is renowned for its exceptional electronic and catalytic properties, and hence has been studied extensively [135-139]. Due to the fact that the constituent elements of hematite are amongst the most common elements found in the earth crust, hematite is earth-abundant. Furthermore, hematite's low cost and non-toxic nature makes its applications in sensors, catalysts, electrode materials of Li-ion batteries and water splitting quite attractive. Furthermore, a recently theoretical work reported that the band gap of hematite could be reduced further with iso-valent S doping, making it a potential solar energy conversion material [140].

Recent developments observed in nanotechnology have opened the possibility of realizing most commonly known bulk materials into nanometer scale. In fact, these materials can experience nanoscale phenomena like edge effects [141],

quantum size effects [142,143] and high surface to volume ratios[144], which may result in the increase of carrier mobility [145], catalytic nature [146] and even change in band gap nature from indirect to direct [147]. These effects are prevalent in hematite and the bottom-up approach have made it possible to synthesize many hematite nanostructures like nanotubes [148,149], nanorods [149], nanorings [150], and nanosheets [151] (NSs). These nanostructures have shown significant promise in electronic devices applications such as semiconducting devices [152], solar cells [153], and Li-ion battery anodes [154].

Nanoribbons (NRs) are one of the interesting structures among the nanostructures. Due to its quasi one-dimensional nature, NRs integrate the quantum size effects and edge effects quite efficiently in electronic device application. Furthermore, its thin nature enhances the surface to volume ratio, which subsequently increases its reactivity. In practice, NRs are obtained by cutting nanosheets [155] or by unzipping nanotubes [156]. Many studies have been performed on NRs, and in particularly, earth-abundant transition metal oxides, due to their rich chemical and physical properties [157-164]. Interestingly, hematite NRs have not been significantly explored compared to the other transition metal oxide NRs. Synthesis of ultra-thin hematite NRs using thermal oxidations [165] and controlled annealing of oxides and hydroxides [166] have been reported. Thermal oxidation method was used by Xu *et. al.*[165] and created the hematite nanostructures by heating iron foils for 6h at temperatures ranging

from 280 ^{0}C to 500 ^{0}C; they observed that both the width and the thickness of the nanostructures increased with the increasing temperature and the growth rate of the crystal planes follows {110} > {104} $\gg$ {$\bar{2}$10} order. On the other hand, Sarker *et. al.* [166] have used different iron oxides and hydroxides and by means of controlled annealing to create hematite nanoribbons. Calcination at temperature of 500 ^{0}C for 150 minutes decomposes iron hydroxides into the hematite and forms the porous ultrathin nanoribbons. They were also able to discover that these NRs exhibit weak ferromagnetic behavior and their gas sensing ability is increased due to increment of porosity. Furthermore, none of these methods have utilized the NSs or nanotubes in creating the NRs. Since there have been reports of hematite NSs [151] and hematite nanotubes [148], one can create hematite NRs with the conventional methods such as cutting nanosheets [155] or unzipping nanotubes [156]. Although, hematite NRs was realized experimentally, more theoretical insight is still required in order to manipulate their structural, electronic and magnetic properties. With that understanding, hematite NRs could be applied efficiently and effectively into their prospective applications.

In this work we report our study of hematite NRs by Density Functional Theory (DFT). Our study focused on hematite NRs based on (104) and (110) surfaces since they are the dominant peaks in XRD images reported in hematite NR studies [165,166]. The goal of this work is to gain theoretical insights into the structural, electronic and magnetic properties of hematite NRs using ab initio

density functional theory. Our study revealed that all the NRs based on (110) surface are semiconducting in nature, with the edge atoms and NR width strongly influencing the band gap. Out of two NR types yielded from (104) surface, one variant exhibited *pseudo-Jahn-Teller* (pJT) effect [167], while the other had built-in oxygen vacancy which introduces the half-metallic properties. The observed half-metallic character indicates that hematite NRs can be considered as a promising candidate for spintronics-based devices. The remainder of the manuscript is organized as follows. In section II the computational approach is presented. This is followed by the presentation of the results and associated discussions in section III. Finally, a summary of the key findings and conclusions of the work are present in section IV.

7.1.1 Computational Details

All calculations were based on spin-polarized DFT as implemented in Vienna *ab initio* simulation package (VASP) [49,50]. The Perdew–Burke–Enzerhof (PBE) [168] formulation for the generalized gradient approximation to the exchange–correlation functional was employed. Projected augmented wave (PAW) potentials [169] were employed to describe the electron–ion potential, and the kinetic energy cutoff for the plane wave expansion of wave functions was 400 eV. For the nanosheet and nanoribbon calculations, a vacuum of 12 Å applied to remove the interaction with image cells. The valence electron configurations

considered in this study are (3p3d4s) for Fe and (2s2p) for O. To accurately describe the strongly correlated nature of the Fe 3d electrons, the on-site coulomb repulsion of the exchange–correlation energy is treated with the GGA+U approach due to Dudarev *et al.*[170]. We have employed the effective U=4 eV value; this yielded bulk hematite properties that agreed well with the experimental data [140] and other theoretical data [171-174]. The following k-point grids were employed for integrations over the first Brillouin zone : a $5 \times 5 \times 5$ k-point grid used for bulk hematite; a $7 \times 9 \times 1$ k-point grid was used for the nanosheets; a $7 \times 1 \times 1$ (or $1 \times 9 \times 1$) grid, was used for the nanoribbons cleaved in the direction [100] (or [010]) direction. The k-point grids were doubled in the computation of the electronic density of states (DOS). All possible antiferromagnetic (AFM), the ferromagnetic (FM), and the paramagnetic arrangements were considered. The atomic positions were relaxed until the maximum Hellmann–Feynman force on each atom was less than 0.005 eV/Å.

7.2 Results and Discussions

7.2.1 Nanosheets based on (104) or (110) surfaces

Optimized nanosheets of the (104) and (110) surfaces are presented in Figure 7.1. The (104) nanosheet consists of hexagonal rings of Fe and O atoms while the (110) nanosheet consists of octagonal rings of Fe and O

atoms. Those ring arrangements make (104) nanosheet is less porous compared to (110) nanosheet. Depending on the termination edge we can identify different types of nanoribbons. We introduce two types of nanoribbons per nanosheet: Nanoribbons grown in [010] direction are labeled as “n-a Type I”, while the nanoribbons grown in [100] direction are labeled as “n-b Type II”. The notations “n-a” and “n-b” denote *n* repetitions along the *a* axis and *b* axis respectively. - *n* is a measure of the width of the respective NR and the values *n*=1, 2, 3, 4, 5, 6 were considered.

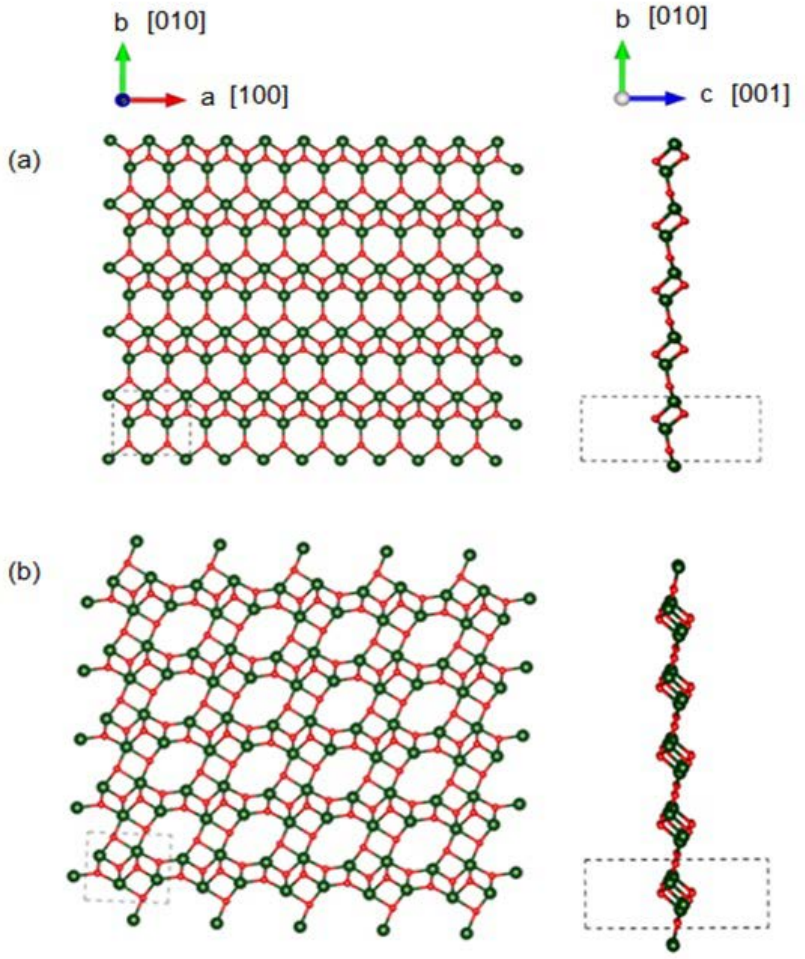

Figure 7.1: (a) Top and side view of the nanosheet in (104) surface. a= 6.003 Å, b= 5.446 Å and c=1.875 Å. (b) Top and side view of the nanosheet in (110) surface. a= 6.356 Å, b= 5.426 Å and c=1.953 Å. The unit cell is marked in dashed line box. Images are super cells of size 5 × 5. O atoms are in red color and Fe atoms are in green color.

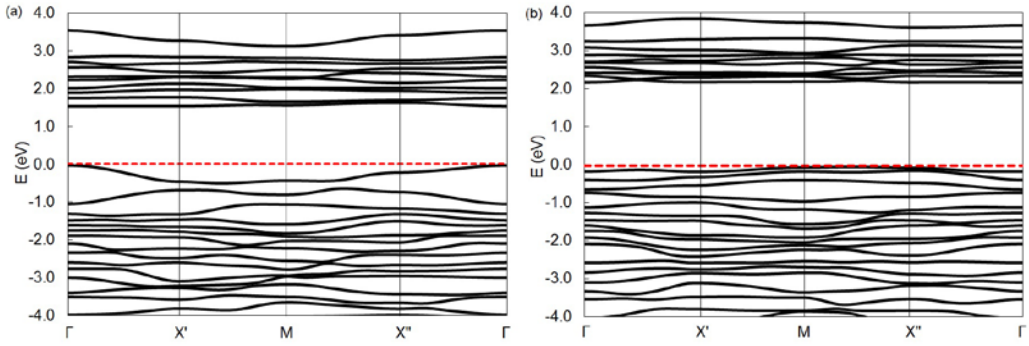

Figure 7.2: (a) Band structure diagram of the (104) nanosheet. (b) Band structure diagram of the (110) nanosheet. Valence band maximum is set to zero in both nanosheets.

The band structures of the nanosheets are presented in Figure 7.2. It can be seen from the figure that the band gap for (104) nanosheet is 1.54 eV and that for the (110) nanosheet is 2.17 eV. The valence band of both nanosheets comprises O 2p orbitals, while the conduction band comprises empty Fe 3d orbitals. The conduction bands are extremely flat in both band structures due to the highly localized nature of the Fe 3d electrons. It is worth mentioning that both these nanosheet structures are in the perfect AFM moment orientation and only the spin-up components are plotted.

The cleaving energy per formula unit (E_c) of these nanosheets with respect to the bulk structure of hematite was also calculated. It is defined as

$$E_C = \frac{E_{NS}}{n} - \frac{E_{Bulk}}{m}, \tag{7.1}$$

where, E_{NS} is the ground state energy of nanosheet and E_{Bulk} is the ground state energy of bulk α–Fe_2O_3 structure. n and m are the number of formula units in the super cells used to calculate the nanosheet and bulk structures respectively. The nanosheet of (104) surface has the cleaving value of 1.41 eV per formula unit and the nanosheet of (110) surface has the cleaving value of 1.51 eV per formula unit. This indicates that the nanosheet on (104) surface is more favorable to synthesize than the nanosheet on (110) surface.

7.2.2 Nanoribbons derived from (110) nanosheet

In Figures 7.3a and 7.33b, we present the optimized structures of the NRs derived from (110) nanosheet. All the NRs remained quasi-flat after the geometry optimization. In Figure 7.3c, we plot the cleavage energies of two NR types versus their respective width. Type I NRs have higher cleavage energy which indicates that Type II NRs are more feasible to realize experimentally than the Type I NRs. NRs derived from (110) nanosheet are always semiconducting in nature, regardless of their width direction (see Figure 7.4). However, Type II NRs have a slightly higher converging band gap of ~1.79 eV compared to Type I NRs converging band gap of ~1.66 eV.

The reported (110) surface based ultrathin hematite nanoribbons in the current work have under-coordinated Fe and O atoms which are similar to surface Fe or O atoms of hematite bulk structure. Bulk Fe and O atoms have coordination numbers of 6 and 4 respectively; surface atoms have less coordination number than those values and in particular capable of generating defect states in the density of states [172]. In the reported (110) based nanoribbons, the under coordinated Fe and O atoms are present throughout the structures and hence there are many defect states present in the density of states. This subsequently reduces the band gap in comparison to the bulk structure. In addition, when we carefully check the two nanoribbons (one from Type I and the other from Type II) with nearly the same width and obtained average Fe coordination numbers for Type I

is 4.40 and 4.42 for Type II. While the difference is small but still support that the Type I, Fe atoms are less coordinated and hence lower in band gap ~0.1 eV. In addition, the coordination number distributions in two types are different; in Type I, there are two Fe atoms per unit cell at the edges, which are always less in coordination number compared to the internal Fe atoms. Since these edge Fe atoms contribute highly in determining band edges (refer to Figure 7.5),

Type I band gaps are always lower in value compared to Type II band gap values. Additionally, the NRs of both categories show higher band gaps in shorter widths due to quantum confinement effect. In addition, as width increases, the band gaps tend to decrease.

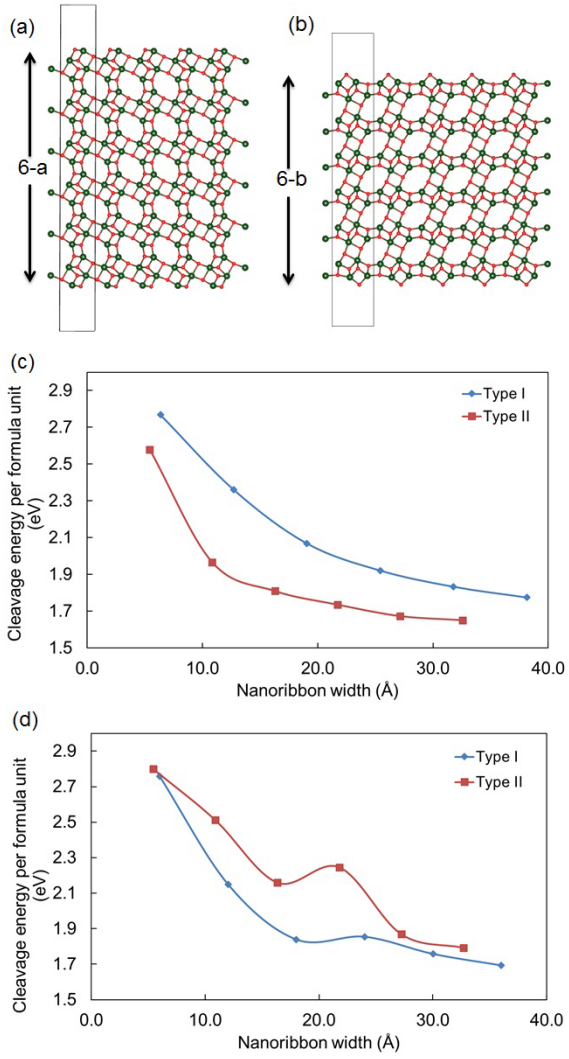

Figure 7.3: (a) Top view of the 6-a Type I NR derived from (110) surface nanosheet. (b) Top view of the 6-b Type II NR derived from (110) surface nanosheet. (c) Cleavage energy for NRs of (110) surface w. r. t. the NR width. (d) Cleavage energy for NRs of (104) surface w. r. t. the NR width. Atoms are in usual color. Images are super cells of size 5. The width of the specific NR is either a= 6.356 Å or b= 5.426 Å times the integer number.

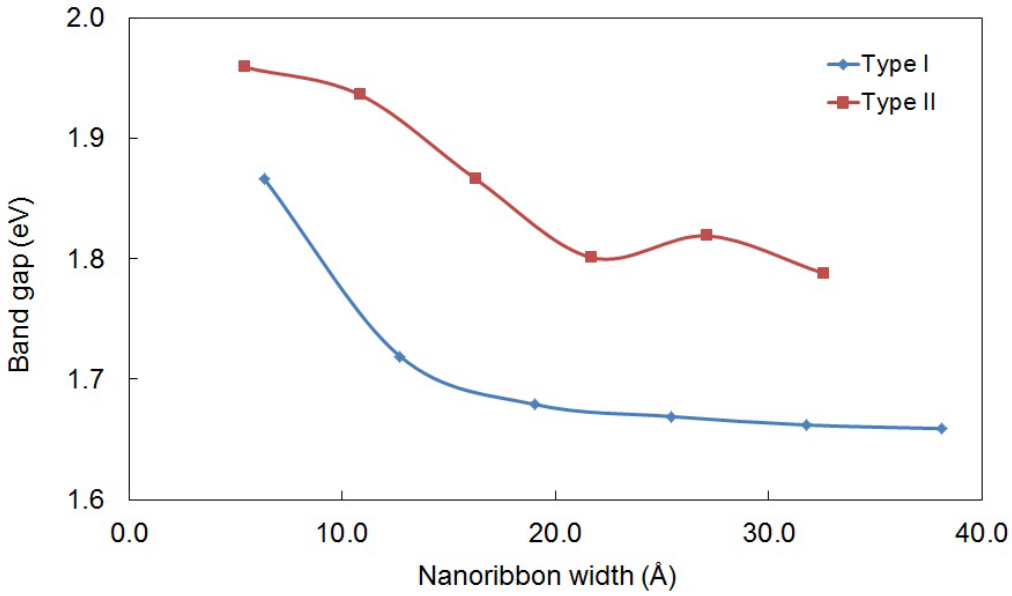

Figure 7.4: Band gap dependence with respect to widths of the NRs derived from (110) surface based NS.

One important observation in the above results is that the band gaps values of the nanoribbons do not tend to converge to the band gap value of the (110) nanosheet. One would expect that, as the widths of these NRs increases, their properties should converge to those of the parent nanosheet since increase in width resemblance more of a nanosheet rather than a nanoribbon. To further understand the origins of these observations, we performed DOS calculations on the NRs. In Figure 7.5, we plot the atom-projected DOS (pDOS) of (110) surface based 5-a Type I NR. The atoms of interest were the middle and edge atoms of the NR structure. We can clearly identify that the pDOS from the edge Fe atoms and edge O atoms dominates the band edges of the NR. This is similar to all other Type I and Type II NR structures of (110) surface. The edge atoms are always present in NRs due termination of one translational direction. At least among the studied width sizes those edge atoms have not rearranged and hence the NR band gap values did not converge towards the nano sheet band gap value. However, the current study of hematite NRs cannot be compared with the experimentally realized NRs due to larger widths and thicknesses of those experimental NRs [166] which are about 30 times larger.

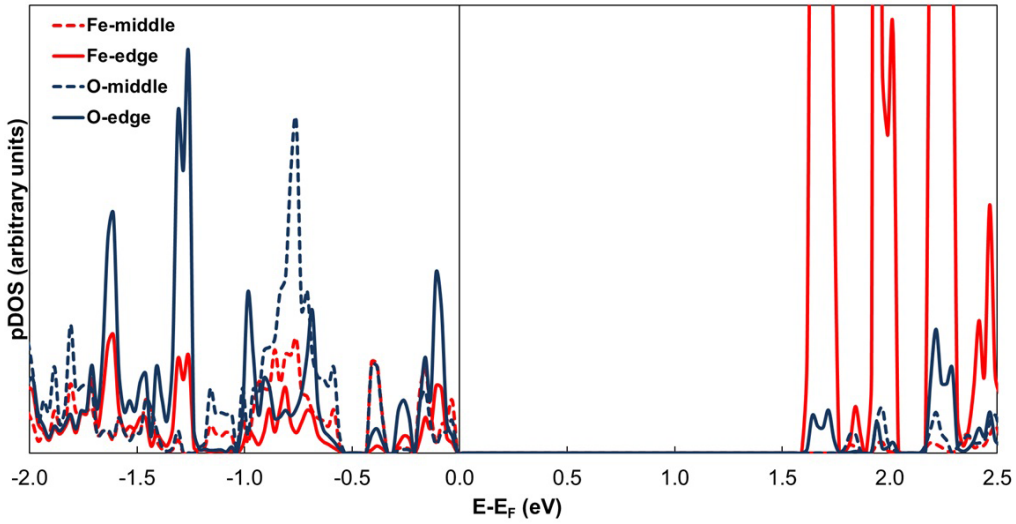

Figure 7.5: Atom-projected DOS of (110) surface based 5-a Type I NR. Fermi energy has been shifted to be at 0.0.

Since those larger widths and thicknesses allow the surface modifications and structural reconstructions to happen, the edge effects may be dissipated. However, the NRs reported in this work have relatively smaller widths which resulted in under coordinated Fe and O atoms at the edges make the dominating contribution to the band gap. Hence, at the current width values, we have much smaller converging band gap values compared to experimental band gap values.

7.2.1 Nanoribbons derived from (104) Nanosheet

The construction of the (104) surface based NRs is similar to the (110) surface based NRs. In Figure 7.6, we present our optimized Type I NRs of (104) surface. Unlike the (110) surface based NRs, there are visible geometrical changes presented in the (104) surface based NRs after optimization. Out of all the NR sizes studied in this category (width sizes “1-a” through “6-a” of Type I), the three smaller widths “1-a”, “2-a” and “3-a” NRs remained flat after the optimization and the three larger widths, “4-a”, “5-a” and “6-a” NRs bended after optimization. One NR structure from each set is presented in Figure 7.6.

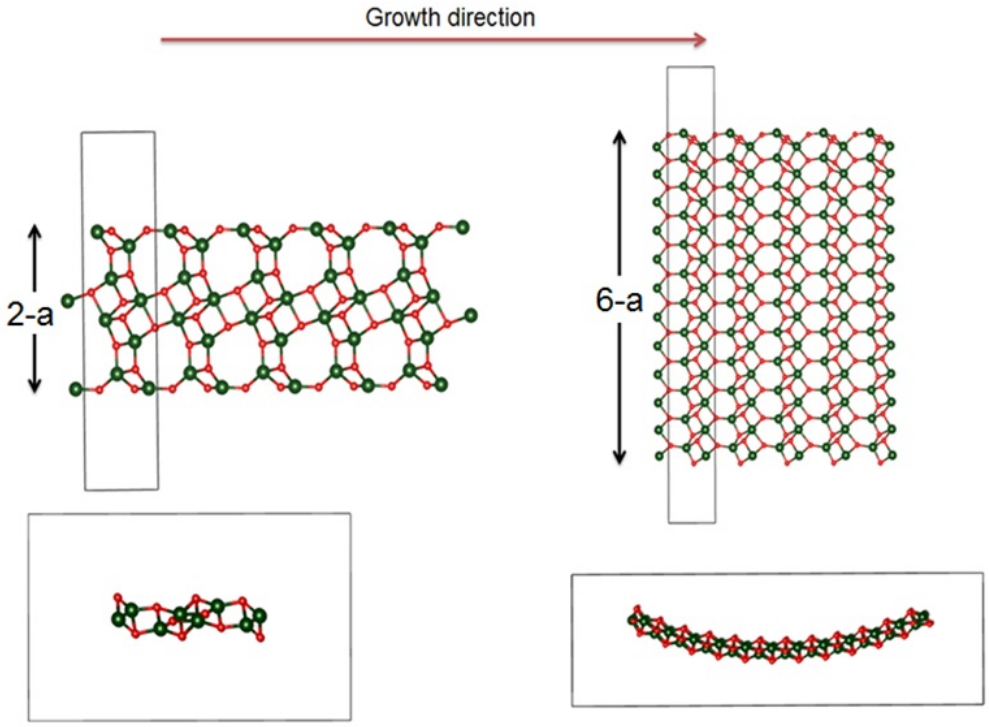

Figure 7.6: Top and side views of NRs 2-a Type I and 6-a Type I NRs derived from (104) surface nanosheet.The unit cell is in the black box. Atoms are in usual color. Images are super cell of size 5. Dimensions are, a= 6.003 Å times the integer number.

It is our understanding that for the first set of NRs (“1-a”-“3-a”), the width is not enough to undergo a structural deformation like bending to stabilize the structure. Instead, those NRs have gone through a surface modification where the structure was rearranged from hexagonal rings to octagonal rings during optimization process to gain the structural stabilization. When the NRs are presented with enough width, as in three larger width NRs, the structural modification happened in the transverse direction which resulted in gaining a curvature for the NR. These modifications indicate the possibility of pJT effect [167].

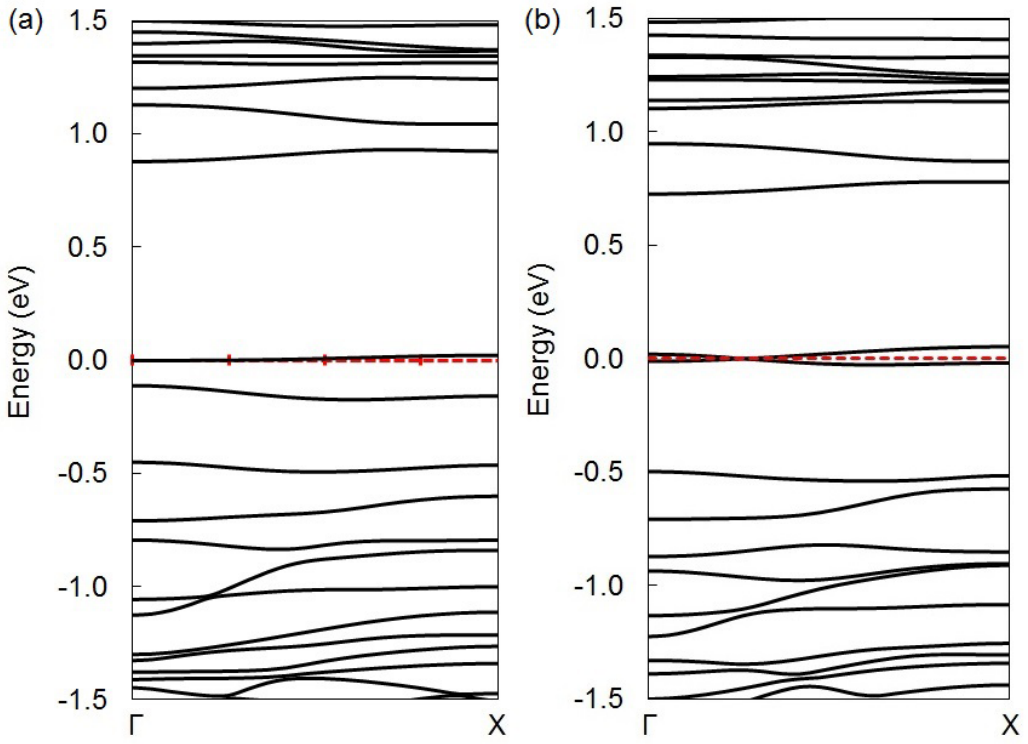

Figure 7.7: (a) Band structure diagram of 4-a Type I NR – no constraint. (b) Band structure diagram of 4-a Type I NR – with constraint. The Fermi energy level is shifted to 0.0 and marked with the red dashed line.

In order to investigate whether these distortions are due to the pJT effect, we have carried out a test optimization with an added constrain, in which we fixed the atomic movement in transverse direction ([001]) where the NRs bend. We have chosen the system 4-a Type I NR for this purpose. Calculation started with the same initial structure as previous "no constrain" calculations. In Figure 7.7, we provide the band structures obtained for optimized 4-a Type I NR system with and without the added constrain. In the "no constrain" situation (refer Figure 7.7a) where the structure deviated from the quasi-flat nature, there are two band lines close to each other around the Fermi level.

These two lines can be considered as originally *pseudo* degenerated bands, and due to the distortion (in order to lower the symmetry), the degeneracy had been lifted (pJT effect). By imposing the constrain of restricting the motion of atoms in [001] direction, we have taken out the system's ability to lower the symmetry. In addition, after the "constrained" optimization, the resulted structure does not show the surface rearrangement observed in smaller width situations. If the distortion of the structure is due to pJT effect, there should be nearly degenerating bands around the Fermi level since there is no any structural deformation after "constrained" optimization. In Figure 7.7b, we could observe such nearly degenerating band lines around the Fermi level. Therefore, it can be concluded that these surface rearrangements and structural deformations happened due to pJT effect.

In addition, we have calculated the cleaving energy of these NRs similar to the (110) surface NRs and plotted the energy values in Figure 7.3d. Unlike the (110) surface NRs, Type I NRs of (104) surface have lower cleaving energies, indicating that Type II NRs are energetically less feasible to synthesize compared to Type I NRs. The band gaps of the first set of Type I NRs ("1-a" to "3-a") are semiconducting and the second set of Type I NRs ("4-a" to"6-a") are metallic. Induced strain due to bending may be the reason for the second set of Type I NRs of (104) surface to be metallic.

In Figure 7.8, we present the optimized atomic and band structures of 6-b Type II NR based on the (104) surface nanosheet. When calculated, the (104) surface based Type II NRs with smaller widths ("1-a"-"3-a") are semiconducting with decreasing band gaps as width increases. The larger width NRs ("4-a"-"6-a") have metallic character (refer to Figure 7.8b and 7.8c) where some bands at the Fermi level are partially occupied. Even though this larger width NRs shows metallic character, we can identify by comparing Figure 7.8b and 7.8c that for the spin up orientation, the band line at Fermi level is localized and for the spin down orientation the band line at Fermi level is delocalized. This kind of a system is known as *transport half metals* [175] rather than metals. Additionally, there are no significant structural modifications similar to Type I NRs of (104) surface. The careful investigation of the structure revealed that the atomic arrangement of this NR type has a built-in O vacancy at one edge (top edge of the NR in Figure 7.8a)

of the structure. The important fact is that we kept the stoichiometry intact. Hence, this is a built-in O vacancy that leads the NRs to have spin-polarized edge effect. Such spin dependent band structure has been reported with TiO_2 NRs [157] where the authors have manually removed the O atoms to create O vacancy. However, our (104) NS based Type II NRs have built-in O vacancy by the flipping of an O atom out of 3 Fe triangle (as shown in the blue color box in Figure 7.8a).

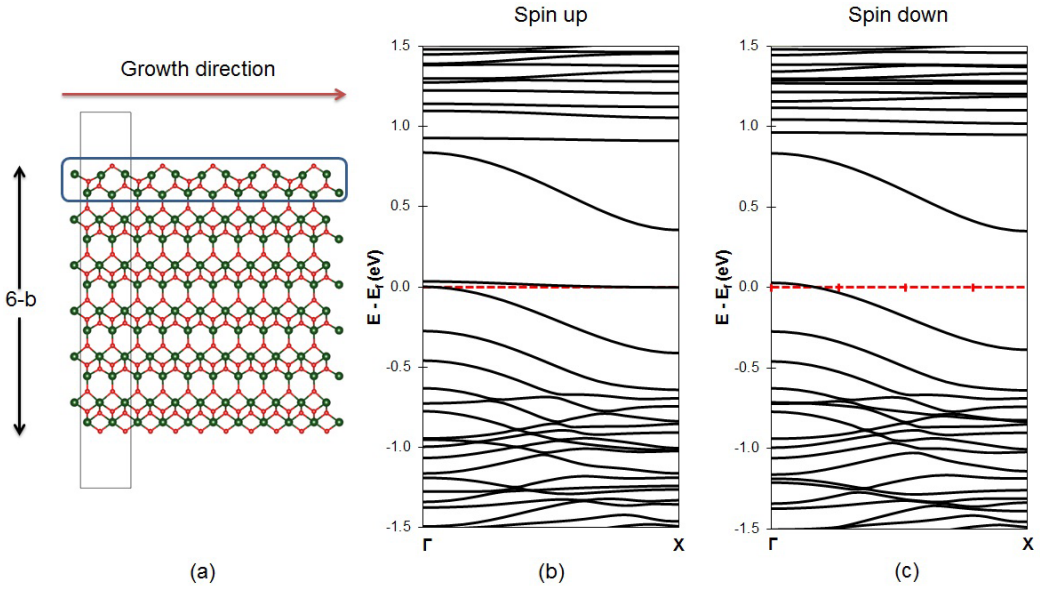

Figure 7.8: (a) Top view of the 6-b Type II NR derived from (104) surface nanosheet. (b) spin up and (c) spin down band structures of 6-b Type II NR derived from (104) surface nanosheet. The Fermi energy level is shifted to 0.0 and marked with a red dashed line. The unit cell is in the black box. Atoms are in usual color. The image is a super cell of size 5. Width is b=5.446 Å times the integer number. NR edge with oxygen vacancy marked with blue color box

This leads to spin dependent band structures. It is our understanding that for smaller widths, this spin-polarized edge effect is screened by the quantum confinement effect which forces the band gap to be open-up. When the NR width is increased, the influence from the quantum confinement effect is weakened and the spin-polarized edge effect starts to dominate. This explains the observation of gradual decrease of the band gap and arising of half-metal character as the increase of widths of the (104) Type II NRs. Most probably, the experimental realization of Type II NRs based on (104) surface may indicate the characteristics of half-metallicity, since the experimentally observed NR[31] widths are much larger in size. Only the narrow width NRs will yield the semiconducting Type II NRs based on (104) surface. The results suggest that these materials are promising in spintronics applications because at low temperatures, electrons of different spins observe different resistance, and definitely the transport of one spin state electrons is higher compared to the other spin state electrons due to changes in the effective masses.

Chapter 8

Conclusions

In summary, we studied four types of SiGe armchair nanotubes. We conclude that tubes are stable and semiconducting in nature with wide spectrum of HOMO-LUMO gaps. Types I, III and IV of SiGe nanotubes show equal stability in terms of binding energy per atom and they express more stability compared to type II. Wide spectrum of HOMO-LUMO gaps in SiGe NTs indicated that they can be used in band gap engineering applications. All the tubes indicate their preferred hybridization is sp^3 and hence once optimized the nanotubes show puckered nature. Out of all nanotube categories type IV nanotubes show the highest tendency towards the p orbital sigma bonding even at larger diameters and have high binding energies. Different bonding, wide spectrum of HOMO-LUMO gaps, and lone pairs of electrons in these NTs indicate the potential wide area of applications.

Our next interest was the Li adsorption on SiGe single walled NTs. Based on 48 possible internal and external adsorption sites, only 18 structures retained the tubular shape. Type III retained the tubular shape for 11 structures out of 12 possible input structures. For the external adsorption, Li could be adsorbed into both “Si Top” and “Ge Top” sites and the concentration can be higher than Si or C based materials. It will be possible to add Li internally in type III category of

SiGeNTs, where Li concentration matches with Si or C based materials. We conclude that there were definite indications of Jahn-Teller distortion effect. The structures that retained the tubular shape after adsorption of one Li atom did not have any Jahn-Teller active orbitals. Hence, it is possible to attach more Li, without distorting the structure. Furthermore, additional studies of SiGe NTs and Li atoms should be done to find the maximum possible concentration of Li atoms and to find the diffusion paths of those Li through the NT. We also conclude that type III SiGeNT has a higher potential to be used as the anode material of a Li ion battery system.

Our study of interaction of SiGe (6,6) NT and H, O, H_2 and O_2 done by adopting the cluster approach. We conclude that Si and Ge atoms of the SiGeNTs can be passivated by H in order to saturate dangling bonds of the NTs. However the passivation in a controlled environment of H can introduce defect states into the frontier orbital region which leads into a reduction of HOMO-LUMO energy gap. Instead, the SiGeNTs introduced into H rich environment will increase the HOMO-LUMO energy gap. Also the increment of the HOMO-LUMO gap is not intense and still preserves the semiconducting nature of the SiGeNTs. In addition SiGeNT interaction with H_2 revealed that the bonding nature is physisorption and have minimal effect on SiGeNT HOMO-LUMO energy gap. Hence we conclude that the passivation of Si and Ge atoms with H atoms could not be achieved via

dissociation of H molecules. Instead it should be achieved with some other means like H treatment of materials[34].

However, O adsorption shows a strong interaction with SiGeNTs and most of the time, atomic O was able to break constitute bonds of SiGeNTs and incorporate into NT wall. The O atom was able to acquire charge from the NT, and HOMO-LUMO energy gap had very minimal decrease due to single O atom interaction. O acted in similar geometrical manner for both O multiple (O rich) and single adsorptions where it always incorporated into tube wall. However HOMO-LUMO energy gap had decreased significantly in O rich situation, in contrast to what we observed in H rich situation.

In O_2 adsorption, the two O atoms, most of the time remained intact beside the bond stretch. However there is a possibility of dissociation of O_2 into two O atoms and incorporate into nanotube wall which modify the electronic structure of SiGeNTs. The acquired charge per O atom was less in O_2 case compared to atomic O adsorption. We note that Si atoms in the SiGeNT were making the stronger bonds with H and O. Our results predicted that locally created SiO_2 (due to single O_2 adsorption, the generated SiO_2 is local in the SiGeNT wall) is stronger than the local GeO_2 occurring in SiGeNTs. Further study of SiGeNT with mixture of H and O, and H_2O will be interesting since it will predict the SiGeNTs interaction with O and H_2O in the presence of H or H treated SiGeNTs.

Our studies revealed that band gap values of armchair (AC) and zigzag (ZZ) SiGeNRs of type I decrease as width increases. Furthermore, the ZZ NRs show direct band gap values at the Γ point for all the widths. In addition, the cohesive energy per atom for the type I show the increasing and saturating trend as width increase. Also the type I SiGe NRs show a tendency to gain a curvature as width increases. In particular, the ZZ type I NRs have fully converted into nanotubes around the NR width of 27.5 Å. However, for type I NRs the curvature increment has decreases and become constant around the highest width considered. Type II and type III for both AC and ZZ categories retained their NR integrity after optimization and kept the sp^3 hybridized nature while type I, have introduced sp^2 and p orbitals in addition to sp^3 hybridized orbitals. Our study further revealed that it is not always possible to make nanotubes from standalone or etched NRs since it has dependence to the atomic arrangement of the structure. In addition, the ZZ SiGeNRs can be used in creating efficient opto electronic devices since the ZZ SiGeNRs exhibit direct band gap properties. Tunable band gap with respect to the nanoribbon width is another advantage in that aspect.

Considering the top-down approach, we have studied hematite nanoribbons based on (110) and (104) surfaces using density functional theory. The results indicate that Type I and Type II of α-Fe_2O_3 NRs from both surfaces are energetically feasible to synthesize. Their feasibility changes in the following ascending order:

$$\text{Type II}_{(104)} < \text{Type I}_{(110)} < \text{Type I}_{(104)} < \text{Type II}_{(110)},$$

which implies, Type II NRs on (110) surface are the most probable on the set to synthesize. (110) surfaced based NRs show the definite semiconducting character with a converging band gap of ~1.66 eV for Type I NRs and ~1.79 eV for Type II NRs. Both types of (110) surface based NRs have the trend of decreasing the band gap with increasing nanoribbon width and eventually converging. In addition, we observed that the under coordinated Fe edge atoms play a major role in determining the band gaps of these ultra-thin narrow NRs. The (104) surface based Type I NRs have gone through either surface re-arranging or bending depending on the nanoribbon width after the optimization, which is due to *pseudo-Jahn-Teller* effect. The Type II NRs of (104) surface have the built-in oxygen vacancy defect in one of its edges while preserving the stoichiometry. This leads to in-equivalent transport property for spin-up and spin-down electrons. This observed oxygen vacancy defect introduces the half-metallicity into the NRs. The feasible energetics, reduced tunable band gaps and half-metallicity of these hematite NRs implies their potential applications in solar energy conversions and spintronics-based devices.

REFERENCES

1. S. Iijima, Nature 354, 56 (1991).

2. R. Saito, G. Dresselhaus, and M. S. Dresselhaus, 1998, Physical properties of Carbon nanotubes, London, UK: Imperial college Press.

3. M P Anantram and F Léonard, Physics of carbon nanotube electronic devices, Reports on Progress in Physics, 69, 507, (2006).

4. Hagmann, M. J. 2005. Isolated carbon nanotubes as high-impedance transmission lines for microwave through terahertz frequencies. IEEE Trans. Nanotechnol. 4(2): 289–296.

5. Kreupl, F., A. P. Graham, G. S. Duesberg, W. Steinhogl, M. Liebau, E. Unger, and W. Honlein. 2002. Carbon nanotubes in interconnect applications. Microelectron. Eng. 64(1–4): 399–408.

6. Li, J., Q. Ye, A. Cassell, H. T. Ng, R. Stevens, J. Han, and M. Meyyappan. 2003. Bottom-up approach for carbon nanotube interconnects. Appl. Phys. Lett. 82(15): 2491–2493.

7. Morris, J. E. 2008. Nanopackaging: Nanotechnologies and electronics packaging. New York: Springer.

8. Postma, H. W. C., T. Teepen, Z. Yao, M. Grifoni, and C. Dekker. 2001. Carbon nanotube single-electron transistors at room temperature. Science 293(5527): 76–79.

9. Li, H., C. Xu, N. Srivastava, and K. Banerjee. 2009. Carbon nanomaterials for nextgeneration interconnects and passives: Physics, status, and prospects. IEEE Trans. Electron Devices 56(9): 1799–1821.

10. Hanson, G. W. 2005. Fundamental transmitting properties of carbon nanotube antennas. IEEE Trans. Antennas Propag. (53): 3426.

11. Maksimenko, S. A., G. Ya. Slepyan, A. M. Nemilentsau, and M. V. Shuba. 2008. Carbon nanotube antenna: Far-field, near-field and thermal-noise properties. Physica E 40: 2360

12. ITRS. 2009. International Technology Roadmap for Semiconductors. http://public.itrs .net, Edition 2009.

13. Avouris, P., Z. Chen, and V. Perebeinos. 2007. Carbon-based electronics. Nat. Nanotechnol. 2(10): 605–613.

14. L. Vayssieres, C. Sathe, S. M. Butorin, D. K. Shuh, J. Nordgren, and J. Guo, Adv. Mater. 17, 2320 (2005).

15. P. Shemella, Y. Zhang, M. Mailman, P. M. Ajayan, and S. K. Nayak, Appl. Phys. Lett. 91, 042101 (2007).

16. O. Hod, J. E. Peralta, and G. E. Scuseria, Phys. Rev. B 76, 233401 (2007).

17. F. Schwierz, Nat. Nanotechnol. 5, 487 (2010).

18. Q. H. Wang, K. Kalantar-Zadeh, A. Kis, J. N. Coleman, and M. S. Strano, Nat. Nanotechnol. 7, 699 (2012).

19. B. C. Faust, M. R. Hoffmann, and D. W. Bahnemanni, J. Phys. Chem. 93, 6371 (1989).

20. M. Chhowalla, H. S. Shin, G. Eda, L.-J. Li, K. P. Loh, and H. Zhang, Nat. Chem. 5, 263 (2013).

21. Hongwei Zhu', Jinquan Wei, Kunlin Wang, Dehai Wu, Volume 93, Issue 9, September 2009, Pages 1461–1470

22. Arora, Narain D., John R. Hauser, and David J. Roulston. "Electron and hole mobilities in silicon as a function of concentration and temperature." Electron Devices, IEEE Transactions on 29.2 (1982): 292-295.

23. R. Martel, T. Schmidt, H. R. Shea, T. Hertel and Ph. Avouris, Appl. Phys. Lett. 73, 2447 (1998)

24. Krupke, R., Hennrich, F., Löhneysen, H.V. and Kappes, M.M., 2003. Separation of metallic from semiconducting single-walled carbon nanotubes. Science, 301(5631), pp.344-347.

25. Chattopadhyay, Debjit, Izabela Galeska, and Fotios Papadimitrakopoulos. "A route for bulk separation of semiconducting from metallic single-wall carbon nanotubes." Journal of the American Chemical Society 125.11 (2003): 3370-3375.

26. Arnold, M. S., Green, A. A., Hulvat, J. F., Stupp, S. I., & Hersam, M. C. (2006). Sorting carbon nanotubes by electronic structure using density differentiation. Nature nanotechnology, 1(1), 60-65.

27. Silicon Heterostructure Handbook: Materials, Fabrication, Devices, Circuits and Applications of SiGe and Si Strained-Layer Epitaxy, John D. Cressler November 1, 2005 by CRC Press

28. SiGe and Si Strained-Layer Epitaxy for Silicon Heterostructure Devices, John D. Cressler CRC Press (December 13, 2007

29. High-k/Ge MOSFETs for future nanoelectronics Y. Kamata materials today Volume 11, Issues 1–2, January–February 2008, Pages 30–38

30. Tarascon, J-M., and Michel Armand. "Issues and challenges facing rechargeable lithium batteries." Nature 414.6861 (2001): 359-367.

31. Taberna, Pierre-Louis, S. Mitra, Philippe Poizot, Patrice Simon, and J-M. Tarascon. "High rate capabilities Fe3O4-based Cu nano-architectured electrodes for lithium-ion battery applications." Nature materials 5, no. 7 (2006): 567-573.

32. Armand, Michel, and J-M. Tarascon. "Building better batteries." Nature451.7179 (2008): 652-657.

33. Nazri, Gholam-Abbas, and Gianfranco Pistoia, eds. Lithium batteries: science and technology. Springer Science & Business Media, 2008.

34. Subrahmanyam Goriparti, Ermanno Miele, Francesco De Angelis, Enzo Di Fabrizio, Remo Proietti Zaccaria, Claudio Capiglia Journal of Power Sources 257 (2014) 421e443

35. H. Wu, Y. Cui, Nano Today 7 (2012) 414e429.

36. J.R. Szczech, S. Jin, Energy Environ. Sci. 4 (2011) 56e72.

37. R. Teki, M.K. Datta, R. Krishnan, T.C. Parker, T.-M. Lu, P.N. Kumta, N. Koratkar, Small 5 (2009) 2236e2242.

38. A. Magasinski, P. Dixon, B. Hertzberg, A. Kvit, J. Ayala, G. Yushin, Nat. Mater. 9 (2010) 353e358.

39. R. Chandrasekaran, A. Magasinki, G. Yushin, T.F. Fuller, J. Electrochem. Soc. 157 (2010) A1139eA1151.

40. C.-M. Park, J.-H. Kim, H. Kim, H.-J. Sohn, Chem. Soc. Rev. 39 (2010) 3115e 3141.

41. A.M. Chockla, K.C. Klavetter, C.B. Mullins, B.A. Korgel, ACS Appl. Mater. Interfaces 4 (2012) 4658e4664.

42. Michael Grätzel Inorg. Chem., 2005, 44 (20), pp 6841–6851

43. Duffie, J. A., & Beckman, W. A. (1974). Solar energy thermal processes. University of Wisconsin-Madison, Solar Energy Laboratory, Madison, WI.

44. Lewis, Nathan S., and Daniel G. Nocera. "Powering the planet: Chemical challenges in solar energy utilization." Proceedings of the National Academy of Sciences 103.43 (2006): 15729-15735.

45. Green, Martin A. "Solar cells: operating principles, technology, and system applications." (1982).

46. Green, MA, Emery, K, Hishikawa, Y, Warta, W, and Dunlop, ED (2015), Solar cell efficiency tables (version 46). Prog. Photovolt: Res. Appl., 23, 805–812.

47. Fuhrer, M. S.; Nygård, J.; Shih, L.; Forero, M.; Yoon, Y.-G.; Mazzoni, M. S. C.; Choi, H. J.; Ihm, J.; Louie, S. G.; Zettl, A.; McEuen, P. L., Crossed Nanotube Junctions. Science 2000, 288 (5465), 494-497

48. Gaussian 09, Revision A.02, M.J. Frisch et. al., Gaussian, Inc., Wallingford CT, 2009.

49. G. Kresse, and J. Furthmuller, Phys. Rev. B 54, 169 (1996).

50. G. Kresse and D. Joubert, Phys. Rev. B 59, 1758 (1999).

51. M. Born and R. Oppenheimer, Annalen der Physik Volume 389, Issue 20, pages 457–484, 1927

52. D. R. Hartree, The Wave Mechanics of an Atom with a Non-Coulomb Central Field. Part I. Theory and Methods, Mathematical Proceedings of the Cambridge Philosophical Society 24, 89-110 (1928).

53. V. Fock, Näherungsmethode zur Lösung des quantenmechanischen Mehrkörperproblems, Zeitschrift für Physik 61, 126-148 (1930).

54. C. Coulson, Present State of Molecular Structure Calculations, Reviews of Modern Physics 32, 170-177 (1960)

55. L. H. Thomas, The calculation of atomic fields, Proceedings of the Cambridge Philosophical Society 23, 542-548 (1927).

56. E. Fermi, Eine statistische Methode zur Bestimmung einiger Eigenschaften des Atoms und ihre Anwendung auf die Theorie des periodischen Systems der Elemente (A statistical method for the determination of some

properties of the atom and its application to the theory of the periodic table of elements), Zeitschrift für Physik 48, 73-79 (1928)

57. P. Hohenberg and W. Kohn, Inhomogeneous Electron Gas, Physical Review 136, B864- B871 (1964)

58. W. Kohn and L. J. Sham, Self-Consistent Equations Including Exchange and Correlation Effects, Physical Review 140, A1133-A1138 (1965).

59. W. J. Carr and A. A. Maradudin, Ground-state energy of a high-density electron gas, Physical Review 133, A371-A374 (1964).

60. M. Gell-Mann and K. A. Brueckner, Correlation energy of an electron gas at high density, Physical Review 106, 364-368 (1957).

61. W. J. Carr, Energy, specific heat, and magnetic properties of the low-density electron gas, Physical Review 122, 1437-1446 (1961).

62. P. Nozieres and D. Pines, The Theory of Quantum Liquids, Cambridge, MA (1999).

63. U. von Barth and L. Hedin, A local exchange-correlation potential for the spin polarized case. I Journal of Physics C: Solid State Physics 5, 1629-1642 (1972).

64. O. Gunnarsson and B. I. Lundqvist, Exchange and correlation in atoms, molecules, and solids by the spin-density-functional formalism, Physical Review B 13, 4274-4298 (1976).

65. S. H. Vosko, L. Wilk and M. Nusair, Accurate spin-dependent electron liquid correlation energies for local spin density calculations: a critical analysis, Canadian Journal of Physics 58, 1200-1211 (1980).

66. O. Gunnarsson, M. Jonson, and B. I. Lundqvist,Exchange and correlation in inhomogeneous electron systems, Solid State Communications 24, 765–768 (1977).

67. T. Ziegler, A. Rauk, and E. J. Baerends, On the calculation of multiplet energies by the hartree-fock-slater method, Theoretical Chemistry Accounts: Theory, Computation, and Modeling (Theoretica Chimica Acta)43, 261-271 (1977).

68. K. Burke, J. P. Perdew, and M. Ernzerhof, Why semilocal functionals work: Accuracy of the on-top pair density and importance of system averaging, Journal of Chemical Physics 109, 3760-3771 (1998).

69. J. P. Perdew, Density-functional approximation for the correlation energy of the inhomogeneous electron gas, Physical Review B 33, 8822–8824 (1986).

70. J. P. Perdew, Electronic Structure of Solids ’91, edited by P. Ziesche and H. Eschig (Akademie Verlag, Berlin (1991).

71. J. P. Perdew and Y. Wang, Accurate and simple analytic representation of the electrongas correlation energy, Physical Review B 45, 13244–13249 (1992).

72. J. P. Perdew, K. Burke and M. Ernzerhof, Generalized Gradient Approximation Made Simple, Physical Review Letters 77, 3865–3868 (1996).

73. A.D. Becke, Density-functional thermochemistry. III. The role of exact exchange, The Journal of Chemical Physics 98, 5648-5652 (1993).

74. A. D. Becke, A new mixing of Hartree-Fock and local density-functional theories, The Journal of Chemical Physics 98, 1372-1377 (1993).

75. C. Lee, W. Yang, R.G. Parr, Development of the Colle-Salvetti correlation-energy formula into a functional of the electron density, Physical Review B 37, 785-789 (1988).

76. Anisimov, Vladimir I. and Zaanen, Jan and Andersen, Ole K. Phys. Rev. B 44, 943-954 1991

77. N. Wang, Y.H. Tang, Y.F. Zhang, C.S. Lee and S.T. Lee, Phys. Rev. B 58, R16024 (1998).

78. J. Hu, M. Ouyang, P. Yang and C.M. Lieber, Nature 399, 48 (1999).

79. M. Menon and E. Richter, Phys. Rev. Lett. 83, 792 (1999).

80. B. Marsen and K. Sattler, Phys. Rev. B 60, 11593 (1999).

81. U. Landman, R.N. Barnett, A.G. Scherbakov and P. Avouris, Phys. Rev. Lett. 85, 1958 (2000).

82. R.Q. Zhang, S.T. Lee, C.-K. Law, W.K. Li and B. K Teo, Chem. Phys. Lett. 364, 251 (2002).

83. P. Pradhan and A.K. Ray, J. Comp. Theo. Nanosci. 3, 128 (2006).

84. S.J. Rathi and A.K. Ray, J. Comp. Theo. Nanosci. 5, 464 (2008).

85. X. Chen, C.-S. Lee, X. Meng and W. Zhang, J. Nanomat. 2011, 830157 (2011).

86. G.G. Guzmán-Verri and L.C.L.Y. Voon, J. Phys.: Cond. Matter 23, 145502 (2011).

87. M.B. Ishai and F. Patolsky, J. Am. Chem. Soc. 131, 3679 (2009).

88. X. Liu, D. Cheng and D. Cao, Nanotech. 20, 315705 (2009).

89. D.B. Migas and V.E. Borisenko, Phys. Rev. B 76, 035440 (2007).

90. O.G. Schmidt and K. Eberl, Nature 410, 168 (2001).

91. J. Zang, M. Huang and F. Liu, Phys. Rev. Lett. 98, 146102 (2007).

92. B. Lalmi, H. Oughaddou, H. Enriquez, A. Kara, S. Vizzini, B. Ealet and B. Aufray, Appl. Phys. Lett. 97, 223109 (2010).

93. J. Muscat, A. Wander and N. Harrison, Chem. Phys. Lett. 342, 397 (2001).

94. J. Heyd and G. Scuseria, J. Chem. Phys. 121, 1187 (2004).

95. W.J. Hehre, L. Radom, P.R. Schleyer and J.A. Pople, Ab Initio Molecular Orbital Theory, Wiley, New York (1986).

96. S.J. Rathi and A.K. Ray, Chem. Phys. Lett. 466, 79 (2008).

97. NBO Version 3.1, E. D. Glendening, A. E. Reed, J. E. Carpenter, and F. Weinhold.

98. S. Nagase, K. Kobayashi and N. Takagi, J. Org. Chem. 611, 264 (2000).

99. P. Pyykkö, Chem. Rev. 88, 563 (1988).

100. M. Wendt and F. Weinhold, NBOVIEW 1.1, Theoretical Chemistry Institute, University of Wisconsin, Madison (2001).

101. N.M. O'Boyle, A.L. Tenderholt, K.M. Langner, J. Comp. Chem. 29, 839 (2008).

102. Li N, Martin CR, Scrosati B (2001) Nanomaterial-based Li-ion battery electrodes. Journal of power sources 97-98:240-243. doi: 10.1016/S0378-7753(01)00760-1.

103. Gao B, Kleinhammes A, Tang XP, Bower C, Fleming L, Wu Y, Zhou O (1999) Electrochemical intercalation of single-walled carbon nanotubes with lithium. Chem Phys Lett 307:153-157. doi: 10.1016/S0009-2614(99)00486-8.

104. Zhao J, Buldum A, Han J, Lu JP (2000) First-principles study of Li-Intercalated carbon nanotube ropes. Phys Rev Lett 2000, 85, 1706-1709. doi: 10.1103/PhysRevLett.85.1706.

105. Lahiri I, Oh S-W, Hwang JY, Cho S, Sun Y-K, Banerjee R, Choi W (2010) High capacity and excellent stability of lithium ion battery anode using interface-controlled binder-free multiwall carbon nanotubes grown on copper. ACS Nano 4:3440-3446. doi: 10.1021/nn100400r

106. Wang W, Kumta PN (2010) Nanostructured hybrid silicon/carbon nanotube heterostructures: reversible high-capacity lithium-Ion anodes. ACS Nano 4:2233-2241. doi: 10.1021/nn901632g

107. Song T, Xia J, Lee J-H, Lee DH, Kwon M-S, Choi J-M, Wu J, Doo SK, Chang H, Park WI, Zang DS, Kim H, Huang Y, Hwang K-C, Rogers JA, Paik U

(2010) Arrays of sealed silicon nanotubes as anodes for lithium ion batteries. Nano Lett 10:1710-1716. doi: 10.1021/nl100086e

108. Linus Pauling J. Am. Chem. Soc., 1932, 54, 3570–3582

109. Zhivotovskii DB, Molev G, Kravchenko V, Botoshansky M, Schmidt A, Apeloig Y (2006) Novel aggregation motif of gem-dilithiosilanes: coaggregation of two R_2SiLi_2 molecules

with two RLi molecules. Organometallics 25:4719-4721. doi: 10.1021/om060469o

110. Adamo C, Barone V (1999) Toward reliable density functional methods without adjustable parameters: The PBE0 model. J Chem Phys 110:6158-6170. doi: 10.1063/1.478522

111. Ortiz YP, Seligman TH (2010) Spontaneous symmetry breaking by double lithium adsorption in polyacenes. AIP Conf Proc 1323:257-264. doi: 10.1063/1.3537854.

112. Jahn H, Teller E (1937) Stability of polyatomic molecules in degenerate electronic states. I. orbital degeneracy. Proc Roy Soc Lond Series A Math Phys Science 161:220-235. doi: 10.1098/rspa.1937.0142.

113. Szakács P, Kocsis D, Surján PR (2010) Jahn–Teller distortion of ionized and excited carbon nanotubes. J Chem Phys 132:034309-1-4. doi: 10.1063/1.3292604

114. Koga N, Morakuma K (1992) Ab initio MO study of the C_{60} anion radical: the Jahn—Teller distortion and electronic structure. Chem Phys Lett 196:191-196. doi: 10.1016/0009-2614(92)85952-7

115. Tanaka K, Okada M, Okahara K, Yamabe T (1992) Structure and electronic state of C^{-}_{60}

Chem Phys Lett 193:101-103. doi: 10.1016/0009-2614(92)85690-C

116. Wanaguru P, Ray AK, Unusual Bonding Characteristics in a New Type of Single Walled Armchair SiGe Nanotubes, J. Comput. Theor. Nanosci., 2013;10:859-866.

117. Kissinger G, Pizzini S, Editors, Silicon, Germanium, and Their Alloys: Growth, Defects, Impurities, and Nanocrystals, CRC Press, Boca Raton, FL (2015)

118. Claeys C, Simoen E, Editors, Germanium-Based Technologies: From Materials to Devices, Elsevier Science, Oxford, UK (2007)

119. Zhao M, Zhu Z, Xia Y, Lu M, Stabilizing Zigzag Single-Walled Silicon Nanotubes and Tailoring the Electronic Structures by Oxygen Atoms: First-Principles Studies, J. Phys. Chem. C, 2007;111:2942–2946.

120. Voon LCLY, Sandberg E, Aga RS, Farajian AA, Hydrogen Compounds of Group-IV Nanosheets, Appl. Phys. Lett., 2010;97:163114-3.

121. Osborn TH, Farajian AA, Pupysheva OV, Aga RS, Voon LCLY, Ab Initio Simulations of Silicone Hydrogenation, Chem. Phys. Lett., 2011;511:101-105.

122. Houssa M, Scalise E, Sankaran K, Pourtois G, Afanasev VV, Stesmans A, Electronic Properties of Hydrogenated Silicene and Germanene, Appl. Phys. Lett., 2011;98:223107-3.

123. Wanaguru P, Ray AK, An Ab Initio Study of the Interaction of a Single Li Atom with Single-walled SiGe (6,6) Nanotubes and Consequences of Jahn–Teller Effect, J. Nanopart. Res., 2014;16:2318-17.

124. Adhikari K, Huda MN, Ray AK, Anomalous Dependence of Band Gaps of Binary Nanotubes on Diameters, J. Comput. Theor. Nanosci., 2011;8:1502-1508.

125. Huda MN, Rev. Nanosci. Nanotechnol., 2014;3:88-106.

126. Chen X, Huo Y, Harris JS, Cho S, Park B-G, Editors. O_2-Enhanced Surface Treatment of Ge Epitaxially Grown on Si for Heterogeneous Ge

Technology, The 18th IEEE International Symposium on Consumer Electronics (ISCE 2014), (2014) June 22-25; JeJu Island

127. Tsybeskov L, Lee E-K, Chang H-Y, Lockwood DJ, Baribeau J-M, Wu X, Kamins TI, Silicon–germanium Nanostructures for On-chip Optical Interconnects, Appl. Phys. A, 2009;95:1015-1027.

128. Cho S, Kang IM, Kim KR, Park B-G, Harris Jr. JS, Silicon-compatible High-hole-mobility Transistor with an Undoped Germanium Channel for Low-power Application, Appl. Phys. Lett., 2013;103:222102-4.

129. Tischler JZ, Budai JD, Jesson DE, Eres G, Zschack P, Baribeau J-M, Houghton DC, Ordered Structures in Si_xGe_{1-x} Alloy Thin Films, Phys. Rev. B, 1995;51:10947–10955.

130. Sluiter MHF, Kawazoe Y, Bondengths and Phase Stability of Silicon-Germanium Alloys Under Pressure, Materials Transaction, 2001;42:2201-2205.

131. H. Şahin, S. Cahangirov, M. Topsakal, E. Bekaroglu, E. Akturk, R. T. Senger, and S. Ciraci Phys. Rev. B 80, 155453 2009

132. Effect of surface bonding on semiconductor nanoribbon wiggling structure

Zhang, Yu and Yu, Minrui and Savage, Donald E. and Lagally, Max G. and Blick, Robert H. and Liu, Feng, Applied Physics Letters, 96, 111904 (2010), DOI:http://dx.doi.org/10.1063/1.3353972

133. Adhikari K, Ray AK, Magnetic Silicon Carbide Nanotubes by 3d Transition Metal Atom Functionalization, Phys. Lett. A, 2013;377:2147-2153.

134. J. Heyd, G. E. Scuseria, and M. Ernzerhof, J. Chem. Phys., 124 (2006) 219906.

135. S. S. Shinde, R. A. Bansode, C. H. Bhosale, and K. Y. Rajpure, J. Semicond. 32, 013001 (2011).

136. Y. Xiong, Z. Li, X. Li, B. Hu, and Y. XieInorg, Chem. 43, 6540 (2004).

137. P. Liao, M. C. Toroker, and E. A. Carter, Nano Lett. 11, 1775 (2011).

138. N. Y. Dzade, A. Roldan, and N. H. de Leeuw, Minerals 4, 89 (2014).

139. Y.-X. Zhou, H.-B. Yao, W.-T. Yao, Z. Zhu, and S. –H. Yu, Chem. Eur. J. 18, 5073 (2012).

140. C. Xia, Y. Jia, M. Tao, and Q. Zhang, Phys. Lett. A 377, 1943 (2013).

141. O. Hod, J. E. Peralta, and G. E. Scuseria, Phys. Rev. B 76, 233401 (2007).

142. L. Vayssieres, C. Sathe, S. M. Butorin, D. K. Shuh, J. Nordgren, and J. Guo, Adv. Mater. 17, 2320 (2005).

143. P. Shemella, Y. Zhang, M. Mailman, P. M. Ajayan, and S. K. Nayak, Appl. Phys. Lett. 91, 042101 (2007).

144. F. Schwierz, Nat. Nanotechnol. 5, 487 (2010).

145. Q. H. Wang, K. Kalantar-Zadeh, A. Kis, J. N. Coleman, and M. S. Strano, Nat. Nanotechnol. 7, 699 (2012).

146. B. C. Faust, M. R. Hoffmann, and D. W. Bahnemanni, J. Phys. Chem. 93, 6371 (1989).

147. M. Chhowalla, H. S. Shin, G. Eda, L.-J. Li, K. P. Loh, and H. Zhang, Nat. Chem. 5, 263 (2013).

148. J. Chen, L. Xu, W. Li, and X. Gou, Adv. Mater. 17, 582 (2005).

150. L. Chen, H. Xu, L. Li, F. Wu, J. Yang, and Y. Qian, J. Power Sources 245, 429 (2014).

151. X. Hu, J. C. Yu, J. Gong, Q. Li, and G. Li, Adv. Mater. 19, 2324 (2007).

152. W. Cheng, J. He, T. Yao, Z. Sun, Y. Jiang, Q. Liu, S. Jiang, F. Hu, Z. Xie, B. He, W. Yan, and S. Wei, J. Am. Chem. Soc. 136, 10393 (2014).

153. X. Lu, Y. Zeng, M. Yu, T. Zhai, C. Liang, S. Xie, M.-S. Balogun, and Y. Tong, Adv. Mater. 26, 3148 (2014).

154. C. Liu, H. Dong, Q. Zhang, Q. Sun, L. Yu, and L. Dong, J. Renewable Sustainable Energy 5, 021416 (2013).

155. J. S. Chen, T. Zhu, X. H. Yang, H. G. Yang, and X. W. Lou, Am. Chem. Soc. 132, 13162 (2010).

156. N. Mohanty, D. Moore, Z. Xu, T.S. Sreeprasad, A. Nagaraja, A. A. Rodriguez, and V. Berry, Nat. Commun. 3, 844 (2012).

157. H. Wang, Y. Wang, Z. Hu, and X. Wang, Appl. Mater. Interfaces 4, 6827 (2012).

158. T. He, F. Pan, Z. Xi, X. Zhang, H. Zhang, Z. Wang, M. Zhao, S. Yan, and Y. Xia, J. Phys. Chem. C 114, 9234 (2010).

159. A. R. Botello-Mendez, F. Lopez-Urıas, M. Terrones, and H. Terrones, Nano Lett. 8,1562 (2008).

160. X. Gou, G. Wang, J. Yang, J. Park, and D. Wexler, J. Mater. Chem. 18, 965 (2008).

161. J. Liu, J. Cai, Y.-C. Son, Q. Gao, S. L. Suib, and M. Aindow, J. Phys. Chem. B 106, 9761 (2002).

162. K. Matsui, B. K. Pradhan, T. Kyotani, and A. Tomita, J. Phys. Chem. B 105, 5682 (2001).

163. Q. Chen, L. Zhu, and J. Wang, Appl. Phys. Lett. 95, 133116 (2009).

164. C. K. Chan, H. Peng, R. D. Twesten, K. Jarausch, X. F. Zhang, and Y. Cui, Nano Lett.7, 490 (2007).

165. R. Xu, H. Yan, W. He, Y. Su, J.-C. Nie, and L. He, J. Phys. Chem. C 116, 6879 (2012).

166. D. Sarkar, M. Mandal, and K. Mandal, ACS Appl. Mater. Interfaces 5, 11995 (2013).

167. I. B. Bersuker, The Jahn-Teller Effect (Cambridge University Press, Cambridge, U.K., 2006).

168. J. P. Perdew, K. Burke, and M. Ernzerhof, Phys. Rev. Lett. 77, 3865 (1996).

169. P. E. Blöchl, Phys. Rev. B 50, 17953 (1994).

170. S. L. Dudarev, G. A. Botton, S. Y. Savrasov, C. J. Humphreys, and A. P. Sutton, Phys. Rev. B 57, 1505 (1998).

171. O. Neufeld, and M. C. Toroker, J. Phys. Chem. C 119, 5836 (2015).

172. M. C. Toroker, J. Phys. Chem. C 118, 23162 (2014).

173. N. Yatom, O. Neufeld, and M. C. Toroker, J. Phys. Chem. C 119, 24789 (2015).

174. N. Yatom, and M. C. Toroker, Molecules 20, 19900 (2015).

175. J. M. D. Coey, and M. Venkatesan, J. Appl. Phys. 91, 8345 (2002).

BIOGRAPHICAL INFORMATION

Prabath Wanaguru received his Bachelor of Science degree in Engineering Physics from University of Colombo, Sri Lanka. He received his Master of Science degree from Central Michigan University, USA in Physics. His research during his master's studies was on the hydrogen storage on Li mediated carbon nanostructures. After receiving his M.Sc., he joined the University of Texas at Arlington in the fall of 2010. His current research focus is on computational studies of novel nanostructure materials.